Discovery of the Fractional Quantum Anomalous Hall Effect in Moiré $MoTe_2$

Eric Anderson

A dissertation
submitted in partial fulfillment of the
requirements for the degree of

Doctor of Philosophy

University of Washington

2024

Reading Committee:

Xiaodong Xu, Chair

David Cobden

Mark S. Rudner

Program Authorized to Offer Degree:
Physics

University of Washington

Abstract

Discovery of the Fractional Quantum Anomalous Hall Effect
in Moiré $MoTe_2$

Eric Anderson

Chair of the Supervisory Committee:
Xiaodong Xu
Physics

The impact of the integer and fractional quantum Hall effects on condensed matter physics can hardly be overstated. Their discovery in the 1980s [1, 2] and the subsequent theoretical interpretation by Thouless et al., Laughlin, Jain, Halperin, and others [3–6] has resulted in a completely new way of thinking about condensed matter. We now understand that there are quantum phases beyond those described via Landau symmetry-breaking theory - that is, phases with topological order [7]. The physics of fractional quantum Hall phases is particularly rich, leading to concepts such as charge fractionalization, composite fermions, and non-Abelian anyon excitations. Beyond their fundamental interest, non-Abelian anyons could lead to topologically-protected quantum computation [8]. However, the massive magnetic fields and millikelvin temperatures necessary for fractional quantum Hall physics make experiments extremely difficult. Lattice systems showing a quantized Hall effect at zero magnetic field without the formation of Landau levels - Chern insulators - were first proposed by Haldane [9]. More recently, systems hosting lattice versions of fractional quantum Hall states, or fractional Chern insulators (FCIs), have been explored theoretically [10–15]. The quantized Hall effect at zero field - the quantum anomalous Hall effect - was observed experimentally in 2012 [16]. The natural question then arises: are there systems which show the fractional quantum anomalous Hall effect?

In this dissertation, we answer in the affirmative. By forming a heterostructure of two monolayers of van der Waals semiconductor $MoTe_2$ with a small twist angle, a moiré superlattice can be

realized. Surprisingly, this superlattice meets all the criteria to host an FCI - topological bands, strong correlations, and spontaneous time reversal symmetry breaking. Using optical probes, we observe ferromagnetism arising from strong correlations between doped holes over a large region of phase space. Optical Landau fan diagrams, compared with the expected Streda formula dispersion for topological states, provide the first signature of a zero-field FCI. Transport measurements at zero magnetic field reveal not only an integer quantized Hall resistance at full filling of the moiré Chern band, but also fractionally quantized Hall resistance at multiple fractional fillings. These results constitute the first experimental observation of the fractional quantum anomalous Hall effect. This groundbreaking discovery sets up the search for more FCI phases, including those hosting zero-field non-Abelian anyons. We take a first step in this direction, using the optical response of the system to find signatures of a zero-field composite Fermi liquid. The composite Fermi liquid is the parent state of fractional phases which host Abelian anyon excitations - and, possibly, phases which host non-Abelian ones as well.

TABLE OF CONTENTS

LIST OF FIGURES

GLOSSARY

2D: Two-dimensional

vdW: van der Waals

TMD: Transition metal dichalcogenide

$MoTe_2$: Molybdenum ditelluride

hBN: Hexagonal boron nitride

Moiré: Large-scale interference pattern occurring from two superposed periodic patterns - in this case, from the crystal lattice of the constituent monolayer 2D materials

BZ: Brillouin zone

mBZ: Mini Brillouin zone

Chern band: Topologically nontrivial Bloch band

Valley: Local extremum of the valence or conduction band

Exciton: A Coulomb-bound electron-hole pair, in our case occurring when an electron is excited to the conduction band, leaving behind a positively charged hole in the valence band

Trion: The charged bound state of an exciton and an electron or hole

PL: Photoluminescence

dRR: Differential reflectance

DOCP: Degree of circular polarization

σ^+: Right circularly polarized

σ^-: Left circularly polarized

RMCD: Reflective magnetic circular dichroism

FM: Ferromagnetic

AFM: Antiferromagnetic

TRS: Time reversal symmetry

LLL: lowest Landau level

IQHE: Integer quantum Hall effect

FQHE: Fractional quantum Hall effect

QAHE: Quantum anomalous Hall effect

FQAHE: Fractional quantum anomalous Hall effect

FCI: Fractional Chern insulator

CFL: Composite Fermi liquid

ACKNOWLEDGMENTS

My acknowledgments begin, naturally, with my PI, Xiaodong Xu. That he is a brilliant physicist goes without saying. Much of what I have learned over my PhD can be attributed to observing his approach to research - his drive, his breadth of knowledge, and his almost frightening ability to intuit the most promising directions to explore. Just as impressive, however, is his astute judgement of character. It is no accident that my time in the Xu lab was spent surrounded by not only the most gifted people I have ever worked with, but also the warmest and most generous. The amount that I was able to learn and accomplish over these short years would not have been possible without the environment Xiaodong has created - creative, intense, stimulating, and enabling of excellence.

One of the most important aspects of being a successful experimentalist is continually interacting with and learning from talented fellow researchers. This is particularly critical during one's formative graduate school years, where the impact of effective mentorship can be profound. I was incredibly fortunate to have been able to work closely with Tiancheng Song over the first years of my PhD, where I learned not only measurement techniques and scientific writing skills, but also how to think critically as an experimental physicist. His advice and support was critical to my success over the course of my graduate school career, and wish him the best of luck as he starts his own research group at UW Madison.

The success of our rapid, hectic, and exhilarating campaign in pursuit of the fractional quantum anomalous Hall effect would not have been possible without my two brilliant colleagues and friends - Jiaqi Cai and Heonjoon Park. Jiaqi's broad and profound grasp of physics serves as an inspiration for everyone in the group, and has motivated my own drive to achieve a deeper understanding. But beyond his adeptness with physics, his personality and range of interests have made working with him over these past years extremely enjoyable - I have lost count of the number of times we have stayed past midnight in the lab talking about philosophy, or category theory, or geopolitics, or the best way to make a pour-over coffee.

One of the most fortunate aspects of the Moiré $MoTe_2$ project was that it gave me the chance to work closely with Joon. He is one of the greatest device makers I have ever met, and has a nearly superhuman work ethic. He once mentioned to a theory collaborator that fabricating one good transport device takes "200 hours - if you're lucky". The success of the transport measurements of the FQAHE rests primarily on his shoulders. The thing I admire most about Joon, though, is his skepticism, analysis, and good judgement when it comes to understanding what we see experimentally. It has become almost a reflex for me - if something unexpected pops up in some measurement results, my immediate response if Joon is around (and he almost always is) tends to be: "Hey Joon - want to see something weird?"

The degree of collaboration at UW - within Xu lab, with other CME groups in the Physics department, and with other departments - means that the success of any given project relies on the contributions of many members of the 2D community. I am indebted to past members of the Xu group - Nathan, Pasqual, Dmitry, Zhong, Zaiyao, Bevin, Xi, Yingqi, Kyle, Minhao, and John - for all they have taught me about physics, research, and life. One of the great luxuries of academia is that I will have the chance to continue to spend time with them regularly at conferences and visits. I'm glad that the other members of the group working on $MoTe_2$ - Will, Weijie, Courtney, Julian, Dhan, and Jack - will continue pursuing exciting new physics in the system, and I'm looking forward to all the new results which will be coming out of Xu lab over the next few years. I'd also like to thank Kai, an undergraduate who worked with me during the crucial months of the Moiré $MoTe_2$ project, for all his hard work - our device assembly line would not have been nearly as efficient without his help. I'm fortunate to have been able to work with and learn from our excellent postdocs - Yuzhou, Chaowei, and Jiang - and (at least attempt to) absorb some of their understanding of instrumentation, measurement, and crystal growth. I'm also glad that our current ultrafast efforts - attributable mostly to the work of Geoff - will be continued by Ren and Mai. I think I can speak for the entire Xu group about the joy we felt when Essance returned to the lab, and I'm excited to see her STEM results in her work with Juan Carlos. The rest of my Xu lab cohort - Jordan, Jiayi, and Yinong - have been a pleasure to spend my time in grad school with, and I'm sure we will remain close friends.

Because of all the cross-collaboration with Dave, Jiun-Haw, and Matt's groups, I have been lucky enough to get to know the grad students and postdocs in their labs. From helping me to bug-fix equipment, to agreeing to give talks at the condensed matter journal club meetings, I've always found everyone to be incredibly generous with their time and effort. I would like to thank all of the members of my committee - Di, Dave, Mark, Boris, and Rahul - for their guidance and feedback in putting together this dissertation. It was a pleasure getting to know them during my time at UW, whether by taking classes with them, discussing experimental results, or simply talking about life in academia.

I have relied deeply on the assistance of our collaborators - within and outside of UW, in theory and experiment - over the course of my PhD. Discussing our results with Dave and getting his perspective has always been great fun and extremely helpful in figuring out puzzling results. Drawing on the expertise of other experimentalists, including Matt, Jiun-Haw, and Cui-Zu, has also been crucial. Discussions with our theory collaborators, Di, Ting, and Wang, as well as their students, have added greatly to my understanding of moiré systems. The rapid feedback loop and exchange of ideas between the theory and experimental sides has been one of my favorite aspects of this project. None of our work would have been possible without high-quality crystal sources, and we are lucky to be able to work with numerous growth experts - Michael McGuire, Jiaqiang Yan, Xavier Roy, Takashi Taniguchi, and Kenji Watanabe, as well as Jiun-Haw, Chaowei, and Zaiyao here at UW. I am also happy to have had a chance to work with Liang Fu and Aidan Reddy, who have done much to help in my understanding (or at least my attempts at understanding) the exotic phases that can arise in moiré $MoTe_2$.

My family - both immediate and extended - has been a great support over my time at UW. The time I spend with them is always and a lot of fun, and I'm glad to have been able to take the time to see them regularly over my PhD. Having them at the wedding in Normandy, in particular - and seeing them interact with Léa's family and friends - was a great experience, and a restorative one to have before jumping back in to research over the next years.

Lastly, and most importantly, I wish to thank my wife, Léa. Her love and support has been essential for my survival over these past five years - as it will continue to be over the next fifty.

DEDICATION

to Léa

"The two patterns create a third: a moiré, a new world of flowing shadows, interferences. . . ."
— Thomas Pynchon, *Gravity's Rainbow*

Chapter 1

INTRODUCTION

Our story begins - like many great stories - *in medias res*. In the two decades since the isolation of monolayer graphene, the menu of 2D van der Waals (vdW) materials has come to contain hundreds of entries, in a staggering range of flavors. These include insulators, metals, semimetals, semiconductors, superconductors, ferroelectrics, ferromagnets, antiferromagnets, and topological insulators. Often, the monolayer version of a vdW material exhibits strikingly different physics than the bulk crystal. In semiconducting transition metal dichalcogenides (TMDs), for instance, exfoliating down to a single layer results in a direct bandgap at the K and K' valleys of the Brillouin zone, extremely strong exciton binding energies of hundreds of meV, and valley-dependent optical selection rules arising from the massive spin-orbit splitting of the valence band.

The real strength of 2D materials, however, lies not only in their behavior in the monolayer limit, but also from their ability to be formed into heterostructures. These consist of "sandwiches" containing stacked vdW layers of different types, enabling a degree of control and flexibility in the design of materials properties not possible with other device architectures. Particularly useful is the combination of metallic graphite and insulating hexagonal boron nitride to form a parallel plate capacitor structure - a gate - which allows for continuous tuning of electron doping in a 2D material. Rather than creating a series of samples with different chemical dopings to determine the behavior of a material as the Fermi level is changed, a single heterostructure device equipped with a gate can be employed to continuously map out an entire phase diagram.

By the late 2010s, the 2D materials field had become vast.[1] The discovery of graphene - which was awarded the Nobel Prize in Physics in 2010 - had kicked off an area of research spanning fundamental physics, materials science, chemistry, engineering, and a range of other disciplines. The variety of vdW materials was large and growing, heterostructure device fabrication was being

[1]Too vast, in fact, to cover here with any degree of detail. A (by no means inclusive!) selection of review articles can be found in Appendix B.

improved, and measurement techniques relevant to 2D materials perfected. Few suspected, however, that a second 2D revolution - the moiré revolution - was around the corner...

1.1 Overview of dissertation

The goal of this work is to present, in a reasonably self-contained manner, the experiments leading to the discovery of the fractional quantum anomalous Hall effect (FQAHE). States hosting the FQAHE, zero-magnetic-field fractional Chern insulators (FCIs), have stringent criteria - the simultaneous existence of flat, topological Bloch bands (Chern bands), strong electron-electron correlations, and spontaneous time reversal symmetry breaking. As we move chronologically through our experimental results within these chapters, it will become apparent that homobilayer $MoTe_2$ moiré heterostructures, surprisingly, fulfill every one of these criteria.

One of the most exciting aspects of this system is that it promises to make some of the deepest and most abstract concepts in condensed matter physics experimentally accessible. These include electron fractionalization, zero field fractional Chern insulators, and anyonic quasiparticle excitations. As these ideas are crucial to understand the import and implications of the experimental results, they are discussed in more depth in the appendices, which are referred to as needed in the following chapters.

Chapter 2 is an introduction to moiré heterostructures of vdW materials and how they can give rise to correlated and topological phases. We discuss a simple, but powerful, approach to describe the physics of the moiré superlattice - the continuum model. With this picture, we can understand the emergence of flat bands in moiré systems, and with them, a plethora of exotic correlated phases of matter. Using the continuum model picture with semiconducting TMD moirés can result in an effective Kane-Mele model with topologically nontrivial moiré bands - that is, moiré Chern bands. Spontaneously breaking time reversal symmetry leads to the Haldane model with strong electron-electron interactions, which allows for the quantum anomalous Hall (QAH) effect.

In Chapter 3, we discuss the experimental results establishing strong correlations and spontaneous time reversal symmetry (TRS) breaking in near-AA stacked homobilayer $MoTe_2$ moiré. The strong optical response of the $MoTe_2$ system - even in the bilayer - allows for a range of optical techniques to be used to probe the correlated phases. One such technique, reflective magnetic circular dichroism (RMCD), enables a continual readout of spin-valley polarization - that is, ferromagnetism

- in the system. We observe ferromagnetism arise over a range of fillings of the superlattice near one hole per moiré unit cell, tunable both by doping and by the application of an out-of-plane electric field. These results demonstrate correlations and spontaneous TRS breaking in moiré $MoTe_2$, setting the stage for QAH - and for zero-field FCIs as well.

Chapter 4 covers the first experimental signature of zero-field FCIs. Improvements to both sample quality and measurement techniques led to the observation of additional features in RMCD - an enhancement of the strength of the ferromagnetic order at fillings ν = -1 and -2/3 of the moiré unit cell. Using photoluminescence as a probe, we find that these enhancements correspond to gapped, incompressible states. To explore the topology of these states, we apply a magnetic field and observe linear shifts in carrier density. The slopes of these linear shifts match the Streda formula predictions for a Hall conductance σ_{xy} of $-e^2/h$ for ν = -1 - the hallmark of QAH - and, surprisingly, $\sigma_{xy} = -2e^2/3h$ for ν = -2/3. This fractional Hall conductance - for a state surviving down to zero magnetic field - serves as the first experimental signature of zero-field FCIs.

In Chapter 5, we present transport results which show the fractional quantum anomalous Hall effect (FQAHE), confirming the existance of zero-field FCIs. The development of a new device geometry enabling these transport measurements was key to observing the "smoking gun" experimental signature of the FQAHE - Hall resistance R_{xy} quantized to fractional values of h/e^2. The fractionally quantized R_{xy} plateaus observed are the analogs of the Jain sequence states in the fractional quantum Hall (FQH) regime, but without the formation of Landau levels. Rather, the FCI states are found at zero magnetic field in a lattice system. These results experimentally confirm the theoretical predictions of the existence of FCIs, made over a decade previously.

Chapter 6 pushes further, exploiting the unique properties of the moiré $MoTe_2$ system in the search for additional phases which cannot be observed directly via the optical or transport techniques discussed in the previous chapters. Measuring polarization-resolved photoluminescence, we find tantalizing evidence for the zero-field analog of the composite Fermi liquid (CFL) - the compressible parent state of the Jain sequence. In the composite fermion picture, the CFL in the 1/2 filled lowest Landau level (LLL) is the parent of not only gapped states hosting Abelian anyons, but also more exotic ones predicted to host non-Abelian anyons. Thus, finding the analog of the CFL at zero field in a lattice system is a major step towards the dream of realizing zero-field non-Abelian anyons.

We conclude, in Chapter 7, with something of a cliffhanger ending. There is no question of the groundbreaking nature of the discovery of zero-field FCIs.[2] As of yet, though, there is no definite experimental evidence of phases hosting non-Abelian anyons in these moiré systems. This result would be a paradigm shift - beyond the fundamental physics, realizing and manipulating non-Abelian anyons is the primary requirement for achieving topologically-protected quantum computation. However, the results so far are extremely promising. These non-Abelian anyons could be achieved either through more complex heterostructure engineering or simply by a more thorough exploration of the heterobilayer $MoTe_2$ phase space. Thus, my great hope is that this dissertation will quickly be out of date - that the most profound discoveries in this system still lie in wait.

[2]Now in a second moiré system: the rhombohedral pentalayer graphene-hBN moiré superlattice [17]!

Chapter 2

MOIRÉ HETEROSTRUCTURES AND TOPOLOGY

Few systems in physics are as evocatively named as magic-angle twisted bilayer graphene (MATBG). Perhaps this is justified. By arranging carbon atoms in exactly the right way, it is possible to achieve a dazzling array of exotic phases of matter, many of which are still not fully understood. The importance of MATBG, however, is not only due the new physics which has been discovered - and continues to be discovered - in the system. The experimental and theoretical work on twisted bilayer graphene has also established the power and flexibility of moiré vdW heterostructures more generally. The narrative of this chapter will mirror the chronology of research in moiré systems. That is, we will begin by discussing magic angle graphene and how its behavior can be understood, before applying this understanding to 2D materials beyond graphene - in particular, TMDs.

Building a twisted moiré heterostructure is conceptually quite simple. Pick up half of a flake of 2D material, rotate the other by a small angle, and then pick that one up as well. Of course, this is not so straightforward in practice - strain, cracks, bubbles, relaxation, and twist angle disorder are among the many factors that need to be considered experimentally. But we can conveniently ignore all of this for now, and focus on the key concept - the moiré superlattice.

2.1 Moiré Superlattices and the Continuum Model

Moiré patterns have been known for hundreds of years. They are an interference effect, and arise when two similar periodic patterns are overlaid with a slight misalignment. As the constituent patterns slowly come in and out of sync, a much longer length scale pattern occurs. Moirés come about in a wide variety of situations - in fact, the etymology of the term *moiré* comes from a processed textile which shows this long-wavelength wavy pattern. A more contemporary example is the irritating banding which shows up when a picture is taken of a computer screen - the CCD array of the camera and the pixel array of the screen are always slightly misaligned.

Conveniently for us, crystalline materials are also (by definition!) periodic. In fact, it is this periodicity that allows us to solve the Schrödinger equation for a many particle system - normally a daunting task - quite simply by using Bloch's theorem. We can then understand the behavior of our crystal lattice by working in momentum space, and considering the band structure and dispersion of our system. In the case of a single graphene layer, this is famously a massless linear Dirac dispersion. That is, the low energy particles in graphene behave similarly to massless particles such as photons, but with a "speed of light" given by the Fermi velocity v_F, which is approximately $c/300$. This Dirac dispersion leads to interesting physics, including half-integer quantum Hall plateaus and Klein tunneling [18, 19]. However, the periodicity of the graphene lattice allows for an additional approach to tune the properties of the system - forming a moiré superlattice.

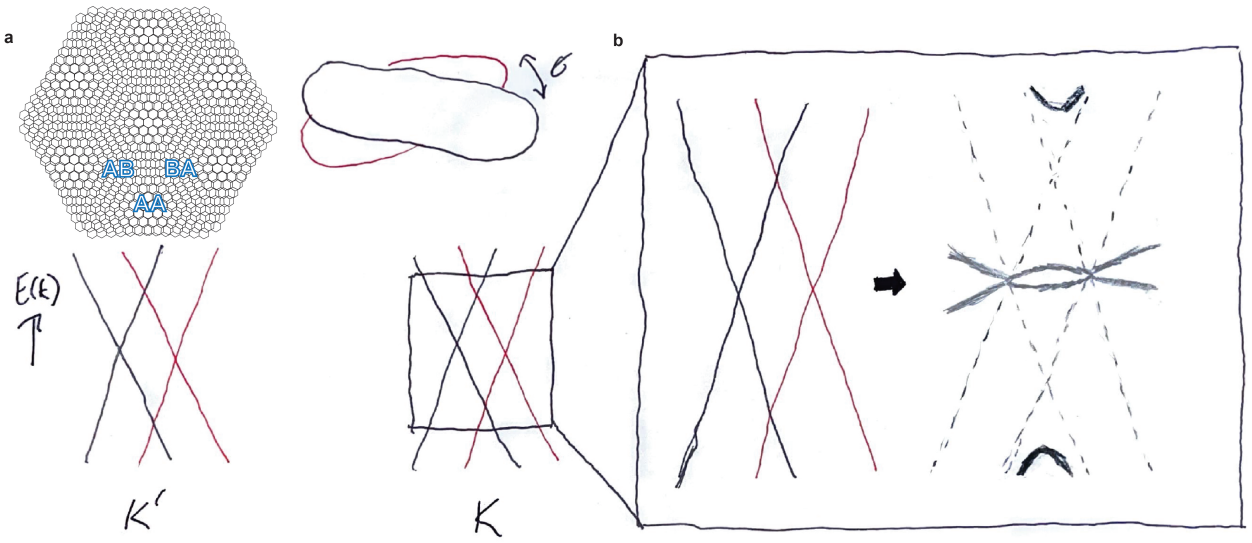

Figure 2.1: Moiré bands. Schematic of the band structure of moiré graphene. **a,** Two stacked graphene flakes are twisted by an angle θ, creating a moiré superlattice. Each moiré unit cell contains three high symmetry stacking points, labelled AA, AB, and BA. The rotation causes a mismatch in momentum space of the top layer (black) and bottom layer (red) graphene Dirac points at the K' and K points. **b,** With finite interlayer tunneling, the Dirac cone crossings from the two layers can mix and split, leading to a flatter moiré band.

The twisted bilayer graphene moiré, and its resulting moiré band structure, is shown schematically in Figure 2.1. The graphene monolayer has a honeycomb lattice structure. By stacking two monolayers with a small twist, a larger-scale moiré pattern arises, with the length scale determined by the twist angle. Considering the behavior in momentum space, the linear Dirac dispersions of

each layer - located at the K and K' valleys in the Brillouin zone - are offset (Figure 2.1a). These two dispersions cross at energies above and below the Dirac points in each valley. Because there is tunneling between the layers, these crossings can gap out, resulting in a new band structure for the twisted bilayer system (Figure 2.1b).

A quite elegant way of formalizing this idea comes in the form of the *continuum model* for moiré systems [21]. This model is quite useful, as a single moiré supercell can contain thousands of individual atoms (depending on the twist angle), and performing calculations on this large of a system can be quite computationally intensive. In addition, it provides a simple, intuitive picture of the physics of these moiré systems. The continuum model approach for TBG considers a bilayer Hamiltonian consisting of two massless Dirac Hamiltonians - one for each layer - and an additional tunneling term which couples the layers. The result is a Hamiltonian which looks like:

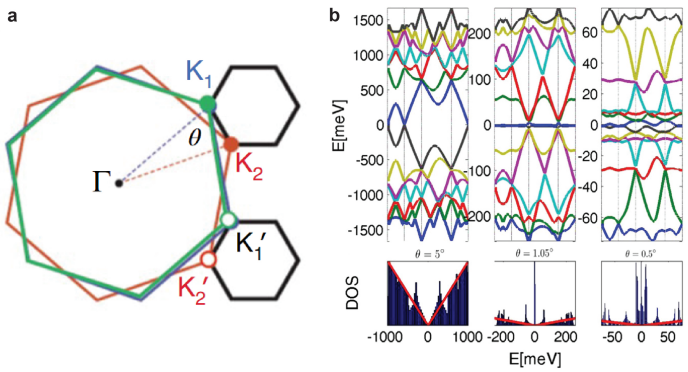

Figure 2.2: The continuum model for graphene. a, Momentum space picture of two graphene flakes twisted by an angle θ. Two mini Brillouin zones (black), corresponding to the K and K' points in the constituent graphene layers, are formed from the angle mismatch. **b,** Moiré band structure for selected angles θ calculated using the continuum model. At large angles, bands are similar to monolayer graphene, showing a Dirac dispersion at the K point. Near the magic angle, at $\theta = 1.05°$, a flat band (blue) forms at the Fermi level. A large DOS is visible near the magic angle. Figure adapted from Refs. [20, 21]. (a) Reproduced with permission from Springer Nature. (b) Copyright 2011 National Academy of Sciences.

$$H_K = \begin{pmatrix} v_F \boldsymbol{\sigma} \cdot \boldsymbol{p}_1 & T_m(\boldsymbol{r}) \\ T_m^\dagger(\boldsymbol{r}) & v_F \boldsymbol{\sigma} \cdot \boldsymbol{p}_2 \end{pmatrix} \tag{2.1}$$

Here, v_F is the Fermi velocity, $\boldsymbol{p}_i = \hbar(\boldsymbol{k} - \boldsymbol{K_i})$ is the momentum relative to the K_i point for $i = 1, 2$ the top and bottom layers, and $T_m(\boldsymbol{r})$ the hopping term between the two layers. This hopping term depends on the lateral offset $\boldsymbol{r}$ between the two layers for a given location in the moiré superlattice. For example, at the AA high-symmetry stacking point, where the carbon atoms from each layer sit directly on top of each other, $\boldsymbol{r} = 0$. H_K is the Hamiltonian for the K mini Brillouin zone (see Figure 2.2a) - the time reversal partner applies to the K' mBZ.

The mBZ consists of two Dirac cones, one from each layer, offset by $k_\theta \approx 2Ksin(\theta/2)$. With the tunneling set to zero, these cross at energies $\pm\frac{1}{2}\hbar v_F k_\theta$. As discussed, turning on the tunneling will cause an avoided crossing, and produce a new set of bands which will change as the twist angle is varied. With some additional analysis of the tunneling term - namely, symmetry constraints and the ability to ignore high-order Fourier components - a band structure can be calculated for an arbitrary angle θ. Because the parameters of the low-energy continuum Hamiltonian are changing over the scale of the moiré - the "high-energy" behavior on the scale of the atomic lattice is thrown out - the calculation is quite efficient, and doesn't require the twist angle to be a discrete, commensurate value of θ.

As can be seen in Figure 2.2b, the tunneling doesn't change the bands very much for large twist angles - the linear Dirac dispersion remains. However, for specific "magic" angles, the band at the Fermi level becomes extremely flat, and the density of states becomes very large. Flat bands are quite exciting - essentially, filling a flat band results in a large number of electrons which are nearly degenerate, and with little dependence on kinetic energy. Therefore, the physics is dominated by electron-electron Coulomb interactions. These sorts of strongly correlated many-body systems tend to result in a range of exotic ground states - and, as we will see, MATBG is no different.

2.2 Correlation and Topology in Moiré Graphene

The first experimental results on correlated phases in moiré systems came out in 2018 - just over five years ago. Transport measurements on moiré graphene heterostructures near the magic angle (Figure 2.3a) showed insulating states not only at charge neutrality and at full electron and hole filling of the moiré band ($\pm n_S$), but also at half filling $\pm n_S/2$ [22]. This is quite unexpected from a band structure picture - a partially filled band should cause a system to act as a metal. However, with strong electron-electron correlations (as in the MATBG flat band), a many-body gap can open, resulting in a correlated insulating phase. Further measurements showed that upon electron or hole doping away from the correlated insulator at $-n_S/2$, resistance drops to zero - the system becomes superconducting (Figure 2.3b) [23]. Superconductivity manifestly relies on correlations between electrons to allow for pairing, and the formation of the flat moiré band is crucial for it to occur.

The interesting physics arising in moiré graphene systems are not only the many-body correlated

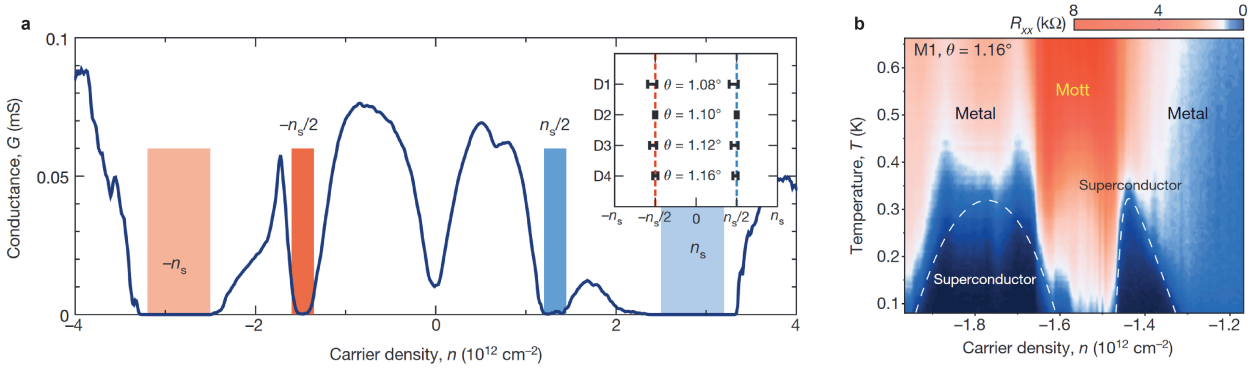

Figure 2.3: Correlated phases in MATBG. a, Correlated insulating states at half-filling of the graphene moiré superlattice, at $\pm n_S/2$. Insulating states arise from strong electron-electron interactions in the half-filled flat band. **b,** Superconductivity in MATBG near $-n_S/2$. Figure adapted from Refs. [22, 23]. Reproduced with permission from Springer Nature.

phases, but topological phases as well. As it turns out, the flat moiré bands in MATBG are topologically nontrivial [24–28].[1] That is, integrating the Berry curvature $\Omega(\boldsymbol{k})$ over a moiré band for a single spin, valley, and sublattice gives a nonzero Chern number:

$$C = \frac{1}{2\pi}\int_{k\in mBZ} d^2k\Omega(\boldsymbol{k}) = \pm 1 \tag{2.2}$$

The existence of a combined rotation and time reversal symmetry C_2T in MATBG constrains the total Chern number to zero for the insulating states, preventing the system from displaying the quantum anomalous Hall effect. However, under certain conditions - such as spontaneous time reversal symmetry breaking by emergent ferromagnetism or rotation symmetry breaking by alignment with hBN - the C_2T symmetry can be broken, allowing for QAH. This symmetry breaking was observed near $3n_S/4$ in TBG. Measurements of the Hall resistance R_{xy} showed hysteresis vs

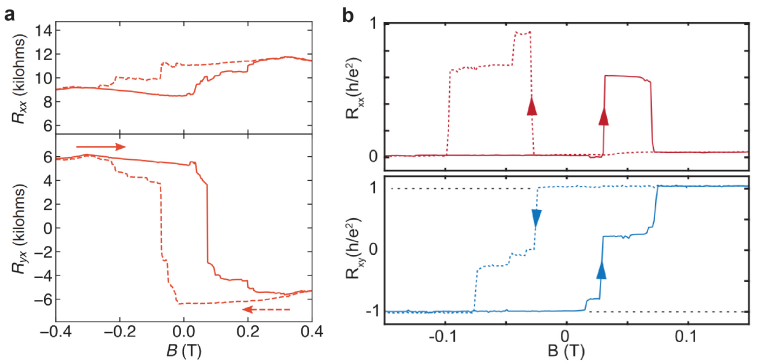

Figure 2.4: Topological phases in MATBG. a, Emergent ferromagnetism in MATBG. **b,** Quantum anomalous Hall effect in MATBG. Figure adapted from Refs. [29, 30]. Reprinted with permission from AAAS.

[1] See Appendices for more resources on topology and a discussion of topologically nontrivial phases.

magnetic field, a hallmark of ferromagnetism (Figure 2.4a) [29]. This is quite surprising, as carbon is not a magnetic element - the ferromagnetism arises from the strong correlations in the flat band. Shortly after, R_{xy} quantized to $\pm h/e^2$ at zero magnetic field was observed in moiré graphene - the hallmark of QAH (Figure 2.4b) [30].

2.3 Gaining (Dirac) Mass: Moiré in Semiconducting TMDs

So far, we have focused on the moiré graphene system near the magic angle of $\sim 1.1°$. This was the first widely studied vdW moiré system, and continues to produce surprising results. However, the idea of moiré superlattices is much more general. Considering the wide range of 2D materials available, and their variety of properties in monolayer form, it is quite natural to consider moiré heterostructures beyond TBG. One of the most fruitful approaches has been in building moiré superlattices of semiconducting TMDs. Not only does this allow for us to take advantage of the optical properties of TMDs, providing a powerful new experimental probe, but can also result in entirely new physics.

There are a number of substantial differences between graphene and TMD moiré systems. One extremely important difference is that semiconducting TMD monolayers are well described by a *massive* Dirac model. Rather than a linear dispersion and Dirac point, TMDs have a conduction and valence band separated by a gap, which is typically in the range of 1-2eV. A similar continuum model approach can be used to describe the coupling of the two massive Dirac Hamiltonians of each layer. However, unlike graphene, the moiré bands of the TMD bilayers don't have a specific magic angle, rather, they remain fairly flat over a range of twist angles.

A second difference is that there are a range of different TMD semiconductors to choose from (WSe_2, WS_2, $MoSe_2$, MoS_2, $MoTe_2$, etc.). One can make a *homobilayer* moiré by playing the same game as with TBG - pick up half of a monolayer, rotate the other half, and pick that one up as well (in fact, we will focus primarily on the TMD homobilayer moiré for the rest of this dissertation). *Heterobilayer* moirés are also possible, though. These can be constructed by choosing two different TMDs (WSe_2 and WS_2, for example) and stacking them with $\sim 0°$ or $\sim 60°$ relative twist. Because the lattice constants of the different materials are slightly mismatched, this system will still form a moiré. In addition, the moiré periodicity will be dominated by the lattice mismatch, so twist angle disorder will be less of a problem in heterobilayers.

A third difference is that, unlike graphene, TMDs have very strong spin-orbit coupling, which leads to a spin splitting of the valence band on the order of 100s of meV. The valence band edges are at the $\pm K$ points in momentum space, and the sign of the splitting is opposite for $+K$ and $-K$. The upshot of this is, for our purposes, the spin and valley degrees of freedom are locked together - the $+K$ valley carriers are spin up, and $-K$ carriers are spin down. Thus, the separate spin and valley degrees of freedom in graphene moirés is lowered to a single spin-valley degree of freedom for the TMDs.

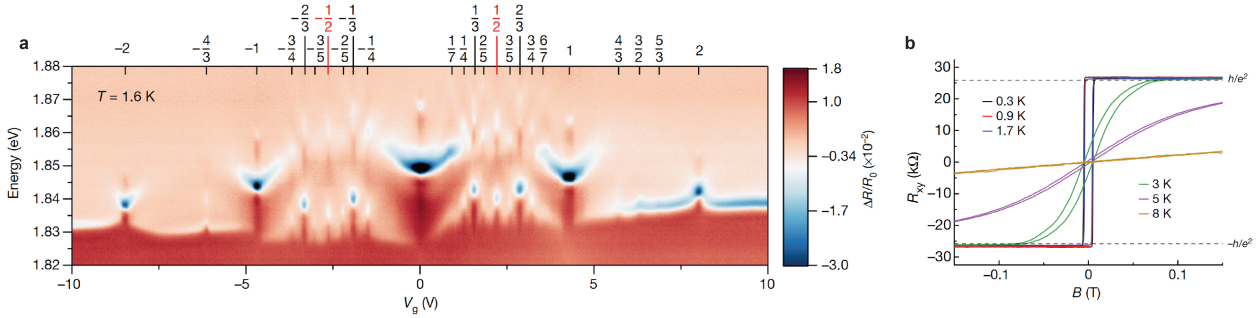

Figure 2.5: Correlation and topology in heterobilayer moiré TMDs. a, Correlated insulating states in a near-0° WSe_2/WS_2 moiré. The 2s exciton resonance of a nearby monolayer WSe_2 sensor layer blueshifts and strengthens upon the formation of a correlated insulating state in the moiré system, due to the change in the local dielectric environment. **b,** Quantum anomalous Hall effect in a near-60° $MoTe_2/WSe_2$ moiré. At filling $\nu = -1$ and large electric field, the system undergoes a band inversion, leading to topologically nontrivial Chern bands and the QAH effect. Figure adapted from Refs. [31, 32]. Reproduced with permission from Springer Nature.

A huge amount of progress has been made on moiré TMD systems over the past few years. The strong optical response of TMDs has proven extremely useful for experimental work [31, 33–38]. However, other techniques, such as microwave impedance microscopy [39], STM [40], compressibility [41], and transport [32, 42, 43] have been employed to study these systems. Although a more complete overview of moiré TMDs is given in the review articles found in Appendix B, some key results are shown in Figure 2.5. Using a monolayer WSe_2 as a sensor, the formation of correlated insulating states in an adjacent TMD moiré can be detected. The idea is that the resonance 2s exciton of the sensor will shift if the local dielectric environment is changed (by, for example, a correlated insulating state forming in the nearby moiré). As shown in Figure 2.5a, this reveals the formation of insulating states at both integer and fractional fillings of the moiré superlattice.

As in moiré graphene, TMD moirés can host topologically nontrivial states. Transport measurements on near-60° $MoTe_2/WSe_2$ heterobilayer revealed a quantized Hall response at filling $\nu = -1$ and large electric field (Figure 2.5b). The quantum anomalous Hall effect in this system can be attributed to a band inversion at large electric field, leading to topologically nontrivial moiré bands.

2.4 Kane-Mele to Haldane

We now turn our attention to the twisted homobilayer TMD moiré superlattice, which is the system we will focus on in the following chapters. The continuum model approach for homobilayer moirés is conceptually quite similar to TBG, with all the caveats discussed in the previous section [44]. Our K-valley valence band Hamiltonian looks like:

$$H_K = \begin{pmatrix} -\frac{\hbar^2(\boldsymbol{k}-\boldsymbol{K_1})^2}{2m^*} + \Delta_t(\boldsymbol{r}) & \Delta_T(\boldsymbol{r}) \\ \Delta_T^\dagger(\boldsymbol{r}) & -\frac{\hbar^2(\boldsymbol{k}-\boldsymbol{K_2})^2}{2m^*} + \Delta_b(\boldsymbol{r}) \end{pmatrix} \tag{2.3}$$

Note that here we have a massive quadratic dispersion for each layer, rather than the massless dispersion for TBG, and there are terms to offset the top and bottom band edges Δ_t and Δ_b, in addition to the interlayer tunneling term Δ_T.

We can collect up all of the Δ terms in our Hamiltonian, and define a layer pseudospin magnetic field - that is, an effective magnetic field acting on the top/bottom layer degree of freedom. The result is:

$$\boldsymbol{\Delta}(\boldsymbol{r}) = (\Delta_x, \Delta_y, \Delta_z) \equiv \left(\mathrm{Re}\, \Delta_T^\dagger, \mathrm{Im}\, \Delta_T^\dagger, \frac{\Delta_b - \Delta_t}{2} \right) \tag{2.4}$$

The Δ_x and Δ_y in-plane components of the pseudospin magnetic field produce interlayer tunneling, and the Δ_z term localizes the wavefunction of the carriers to the top or bottom layer. Each of these components of $\boldsymbol{\Delta}(\boldsymbol{r})$ vary over the moiré unit cell, as they depend on the local offset between the layers, $\boldsymbol{r}$. Symmetry arguments constrain these terms - for example, at the MM site, where the atoms from each layer are directly on top of each other, Δ_z must be 0. In addition, a $C_{2y}T$ symmetry causes the wavefunctions at the MX and XM sites to sit on opposite layers. The layer pseudospin magnetic field variation over the moiré superlattice is shown in Figure 2.6a. One important characteristic to note here is that $\boldsymbol{\Delta}(\boldsymbol{r})$ forms a skyrmion lattice. That is, as we travel across the moiré unit cell, the winding number of $\boldsymbol{\Delta}(\boldsymbol{r})$ is nonzero. The nontrivial winding produces

a real-space Berry phase, and effective real-space magnetic fields which vary on the scale of the moiré unit cell [45].

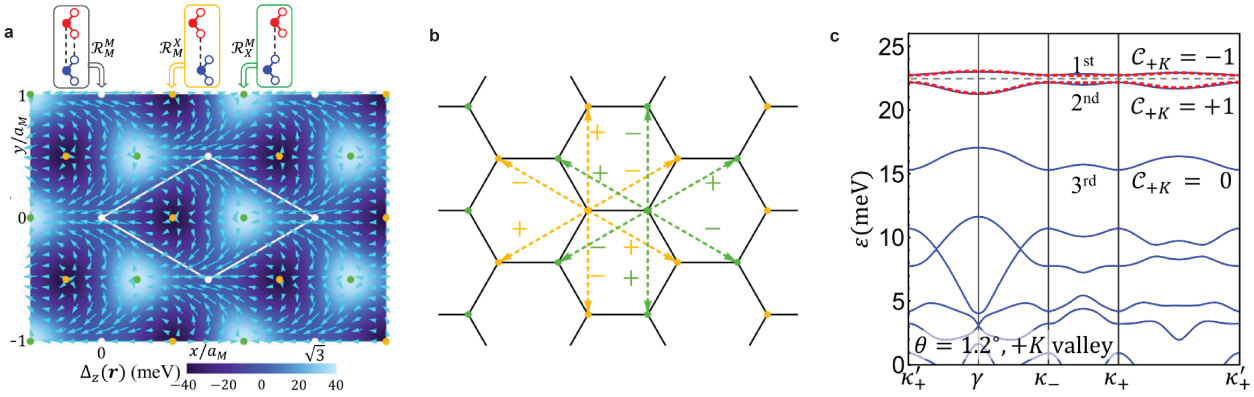

Figure 2.6: The Kane-Mele model in homobilayer moiré TMDs. a, Layer pseudospin over the moiré unit cell. Layer potential Δ_Z favors carriers occupying opposite layers at the MX and XM high symmetry sites. Variation of the layer pseudospin over the moiré forms a skyrmion texture. **b,** Layer pseudospin skyrmion texture leads to $\exp(\pm 2\pi/3)$ phase factors for next-nearest-neighbor hopping between MX (green) and XM (yellow) sites, resulting in an effective Kane-Mele model. **c,** Complex hopping produces topologically nontrivial (Chern) moiré bands in each valley for a range of twist angles. Spontaneous breaking of spin/valley degeneracy leads to QAH. Figure adapted from Ref. [44]. Copyright 2019 by the American Physical Society.

The carriers in the first moiré valence band will preferentially sit on the MX and XM high symmetry sites of the moiré, giving us a honeycomb superlattice. As a result of the layer pseudospin skyrmion texture, the next-nearest neighbor hopping terms (i.e., those between two adjacent MX sites or two adjacent XM sites) will pick up a phase factor of $\exp(\pm 2\pi/3)$ (Figure 2.6b). As a result, our small angle twisted homobilayer moiré TMD realizes an effective Kane-Mele model - that is, two time-reversed copies of the Haldane model, one in each valley [9, 46, 47]. This produces topologically nontrivial moiré bands for each spin/valley (Figure 2.6c). It is worth noting is that not only do these moiré valence bands have a nonzero Chern number, but they are also quite flat. This will turn out to be very important for the observation of the fractional quantum anomalous Hall effect, discussed in the coming chapters. The bandwidth and band gaps of these moiré bands can vary with twist angle θ.

Having established flat topological bands in each valley, there is one more missing ingredient necessary to realize the quantum anomalous Hall effect - and, as we will see, the fractional quantum anomalous Hall effect. The spin/valley degeneracy must be spontaneously broken, allowing for the

filling of a single topologically nontrivial moiré band. In the following chapter, we show that this is accomplished via the spontaneous time reversal symmetry breaking which occurs upon hole doping of the homobilayer moiré $MoTe_2$ system.

Chapter 3

SPONTANEOUS TIME REVERSAL SYMMETRY BREAKING IN MOIRÉ $MOTE_2$

The key to the integer and fractional Chern insulating states observed in the moiré $MoTe_2$ system is spontaneous time reversal symmetry breaking - ie, ferromagnetism. In fact, the first observation of the quantum anomalous Hall effect in 2013 [16] was due to figuring out how to take a topological insulator and spontaneously break time reversal symmetry. This was accomplished by doping with chromium, which provided the ferromagnetic order and created a Chern insulator. More recently, QAH was observed in $MnBi_2Te_4$, a stoichiometric topological insulator with intrinsic ferromagnetism [48]. One of the extremely surprising things about moiré graphene, discussed in the previous chapter, is that it shows ferromagnetism and the QAH effect while being made up entirely of nonmagnetic materials. Rather, twisting the layers to form a moiré superlattice creates flat bands and strong electron-electron correlations, which leads to ferromagnetic order.

In some sense, the ferromagnetic region of moiré $MoTe_2$ is our "playing field". That is, if our ferromagnetism is gone (by increasing temperature, changing doping, etc) we won't be able to observe any of our CI or FCI states. So, one of the advantages of the ferromagnetism in moiré $MoTe_2$ is that it is quite robust. As we will discuss, ferromagnetism is stable over a large region of phase space (doping and electric field) and survives up to $\sim$14K. This may seem like a fairly low temperature! But recall that this is magnetism coming from a moiré superlattice, rather than a crystal structure. The longer length scale, and correspondingly smaller energy scale, of moiré systems means that 14K is actually surprisingly high. It is quite helpful that we have such a large range of phase space to play around with, and a major goal is to figure out how to make the moiré ferromagnetism even more robust.

In this chapter, we will discuss the observation of correlated states in moiré $MoTe_2$ - an indication of strong electron-electron interactions - and the emergence of ferromagnetism upon hole filling of the first moiré valence band. Using the heterostructure gates, we can apply an out of plane

electric field to our system, destroying the ferromagnetism. This behavior can be understood as tuning between an effective honeycomb and triangular superlattices, which changes the exchange interactions from FM to AFM. From the AFM phase, doping even more holes into the system leads to a reemergence of ferromagnetism. These observations set the groundwork for the topological physics that we will see in the coming chapters.

3.1 Correlated States

The lattice structure of a crystalline solid fundamentally determines its physical properties. Therefore, the ability to adjust these lattice parameters - or even continually tune them - would enable us to access a complex electronic phase diagram. This is, in large part, the promise of 2D van der Waals moiré superlattice heterostructures. These systems can serve as synthetic quantum materials, where lattice constants, layer stacking, and Coulomb interaction strengths can be controlled, achieving designer Hamiltonians [23]. While a range of correlated and topological states have been observed in triangular superlattices [29–34, 39, 40, 49, 50], the honeycomb lattice remains largely unexplored. In addition, the ability to *dynamically tune* between superlattice geometries has not been realized, which would provide a method to continuously drive a phase transition between states with distinct symmetries.

Stacking two monolayers of the same transition metal dichalcogenide (TMD) material can offer such an opportunity [44, 45, 52–55]. For a small twist angle away from the AA-stacked configuration, the moiré will have two degenerate energy minima within a single supercell (Figure 3.1a). These minima are on the MX (B sublattice) and XM (C sublattice) high symmetry points. Here, MX refers to transition metal atoms (M) of the top layer sitting on top of the chalcogen atoms (X) of the bottom layer. Crucially, holes doped into the superlattice will preferentially sit on opposite layers for the two different minima, which are linked by a C_2 symmetry (Figure 3.1b). This gives a layer pseudospin, which is locked to the high symmetry points in the moire unit cell. Applying an out-of-plane electric field, D, allows us to layer polarize the system. This pushes the doped holes into a single layer and high-symmetry site, driving a transition between a two-orbital, quarter-filled honeycomb lattice and a one-orbital, half-filled triangular lattice, when considering spin degeneracy (Figure 3.1c).

This near-AA stacked homobilayer moiré had been predicted to host a range of exotic phe-

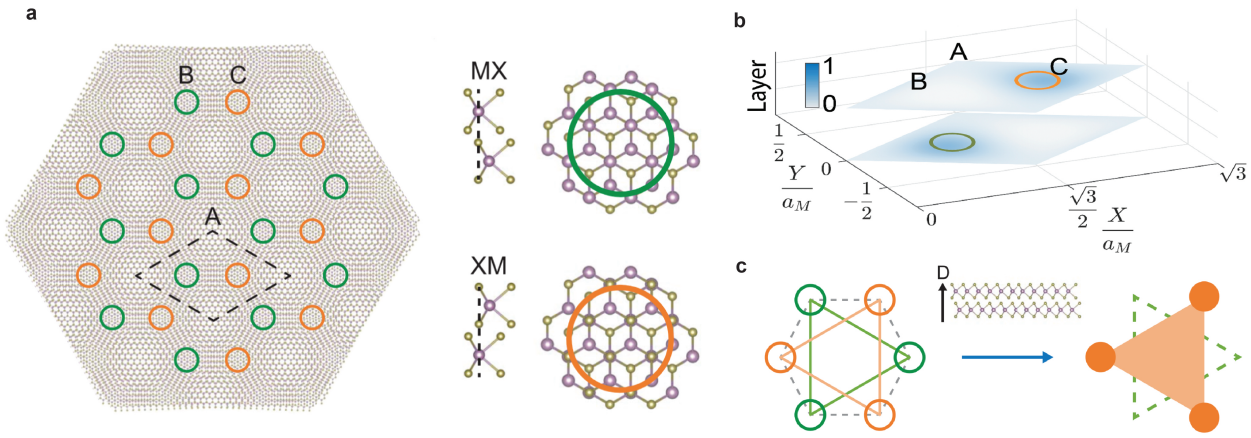

Figure 3.1: Tunable superlattice geometry in the homobilayer moiré. **a,** Schematic of near-AA stacked moiré $MoTe_2$ superlattice. Green circles correspond to MX (B) sites, and orange circles correspond to XM (C) sites. **b,** Spatial density distribution over the real-space moiré unit cell calculating for a doping of one hole per unit cell ($\nu = -1$). Holes preferentially sit on the bottom layer for the MX site, and top layer for XM site. **c,** Out-of-plane electric field D applied by gates lifts layer degeneracy and switches superlattice geometry from honeycomb to triangular. Figure adapted from Ref. [51]. Reprinted with permission from AAAS.

nomena, including the quantum spin hall effect, ferroelectric Mott insultors, integer and fractional quantum anomalous hall states[1], and electric field driven electronic phase transitions [44, 45, 56–63]. In addition, a range of experimental work had been carried out on near-AA stacked homobilayer systems, including studies of moiré ferroelectricity [64], interlayer exciton-electric polarization coupling [65], correlated electronic phases [42, 66], and quantum criticality near one hole per moiré unit cell ($\nu = -1$) [43]. In the following sections, near-AA stacked twisted bilayer $MoTe_2$ will be established as a model system to explore interaction-induced magnetism with electrically tunable moiré geometry.

We study near 4° twisted $MoTe_2$ bilayers, using the dual gated heterostructure geometry discussed in the previous chapter to independently control carrier density n and the out-of-plane electric field, or displacement field, D. Temperature for optical measurements is 1.6K unless otherwise noted. We begin characterizing these devices by measuring photoluminescence as a function of gate-controlled doping. In this measurement, we excite carriers from the valence band to the conduction band using a 633nm HeNe laser with linear polarization, an excitation energy well above

[1] see Appendix D

the band gap. For the $MoTe_2$ monolayer, we see strong photoluminescence, the energy and intensity of which is tuned as the system is doped (Figure 3.2a). This strong emission is due to the formation of excitons - bound electron-hole pairs - when carriers are excited from the valence to conduction bands. These excitons have extremely strong binding energies of 100s of meV, as the 2D nature of the system reduces screening between the charges. The direct band gap of TMD monolayers at the K and K' valleys leads to bright exciton emission. Upon doping of either electrons or holes, the neutral exciton (X^0) disappears, and new features appear at lower energy. These are the positively and negatively charged trions (X^+ and X^-), which are formed when the doped free carriers dress the neutral exciton [67].

While this behavior is common in monolayer semiconductor TMDs, the bilayer displays behavior which is quite unusual. Generally, going from the monolayer to the bilayer produces a change in the TMD band structure from a direct to indirect band gap. This quenches the PL emission, preventing it from being a good probe of bilayer systems. As we see in Figure 3.2b, however, the $MoTe_2$ bilayer PL signal is just as strong as that of the monolayer. This indicates that the moiré bilayer retains the direct bandgap and K-valley physics of the monolayer - behavior which has been observed in untwisted 2H-stacked bilayer $MoTe_2$ as well [68, 69]. Thus, the bilayer system retains the appealing optical properties of monolayer TMDs - strong emission, K-valley valence band physics, and spin/valley/helicity locked optical selection rules - while also enabling twist angle engineering of the moiré superlattice. This, as well as the extremely sharp ($\sim$5meV) emission peak, establishes PL as a sensitive and powerful probe of correlated physics.

Unlike the monolayer, though, there are clear features appearing in the trion PL as doping is changed in the moiré bilayer. These resemble the behavior of interlayer exciton PL in WSe_2/WS_2 heterobilayer moirés, which have been used to probe correlated electronic states at integer and fractional filling of the superlattice [34, 38, 70, 71]. In our system, these features can be understood as the formation of correlated insulating states at particular fillings of the moiré unit cell. When these insulating states form and a Hubbard gap opens, the free doped carriers are consumed, and are no longer available to dress the exitons and form a trion. Thus, we observe a decrease in intensity and a blueshift of the trion PL peak (Figure 3.2c-e). From the strongest features in the PL, we can assign doping values for integer filling of the moiré unit cell. From this, we infer a twist angle of about 3.9°, consistent with the targeted twist angle of 4°. Note that, while the correlated

insulating states are clearest at integer filling, there are features at fractional fillings on both the electron and hole doping sides.

3.2 Optically Detected Ferromagnetism

Taking advantage of the optical properties of the moiré bilayer system, we have established that strong correlations - as indicated by the formation of correlated insulating states - are present in twisted $MoTe_2$. Now, our goal is to explore the magnetic interactions. Conveniently, it is also possible to accomplish this using optical probes. In addition to a strong PL signal which shows correlated states, differential reflectance (dRR) can also serve as a useful technique. To obtain a dRR spectrum, we send in broadband white light from a tungsten-halogen lamp and spectrally resolve the reflected signal. Normalizing the sample signal with another spectrum taken off the sample, we can observe the resonances corresponding to the exciton and trion features as a function of doping.

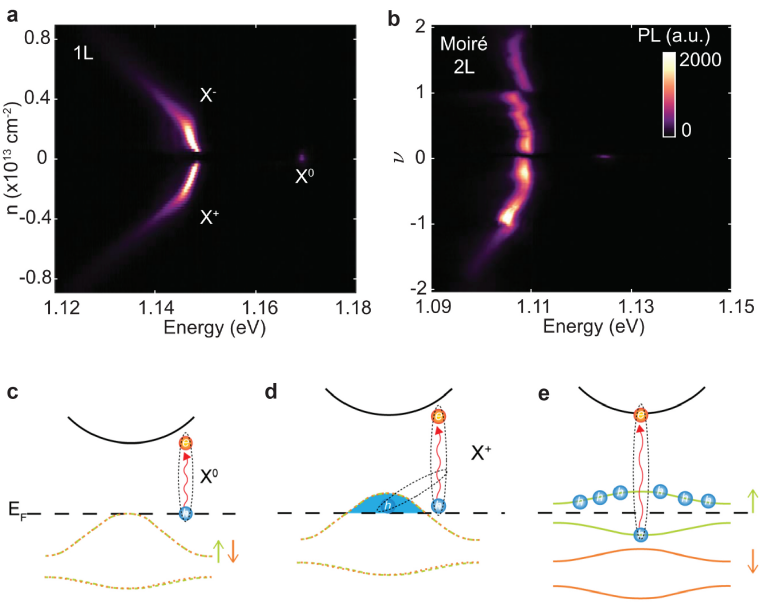

Figure 3.2: Photoluminescence measurements of monolayer and twisted bilayer $MoTe_2$. a, Energy-resolved monolayer $MoTe_2$ PL vs doping. Neutral exciton (X^0) and positively/negatively charged trion (X^+/X^-) features are labelled. **b,** As in (a), but for twisted bilayer $MoTe_2$. Doping has been converted to filling factor ν. Integer and fractional features are visible on both the electron and hole doping sides. **c,** Schematic of neutral exciton recombination and emission. **d,** As in (c), but for the positively charged exciton (trion) when holes are doped into the first moiré valence band. **e,** As (d), but at $\nu = -1$. The gapped state consumed the doped holes, leading to a decrease in trion PL intensity, and a blueshift in the peak energy. Figure adapted from Ref. [51]. Reprinted with permission from AAAS.

As mentioned previously, the bilayer system retains the spin/valley/helicity locking of the mono-

layer TMDs.[2] Thus, circular polarization resolved dRR can indicate valley, and therefore spin, polarization. In Figure 3.3a&b, we see features at the insulating states, as in the PL measurement, but also a clear difference in absorption features between collecting right (σ^+) or left (σ^-) circularly polarized light. Taking the difference between σ^+ and σ^-, it is apparent that there is spin/valley polarization in the system for a range of doping around $\nu = -1$ (Figure 3.3c). This difference between σ^+ and σ^- reflectance from the spin polarization is referred to as reflective magnetic circular dichroism (RMCD). As measuring the entire accessible phase space of ν and D with polarization-resolved dRR would be quite time consuming, we employ a lock-in technique to continually read out RMCD.

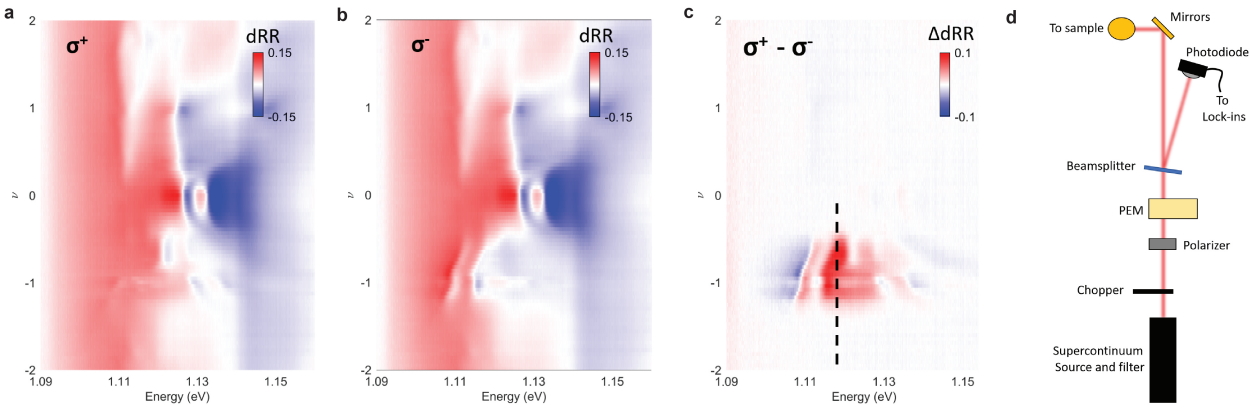

Figure 3.3: Differential reflectance and RMCD. a, Right circular polarization resolved dRR vs ν. **b,** Left circular polarization resolved dRR vs ν. **c,** Difference between (a) and (b), showing helicity-dependent absorption, and thus spin/valley polarization, near $\nu = -1$. **d,** Schematic of RMCD setup.

The schematic of our RMCD setup is shown in Figure 3.3d. Using a filtered supercontinuum source, we select an excitation energy band near the dRR resonances, giving us an RMCD signal, as denoted by the dotted line in 3.3c. This excitation is chopped at ∼1kHz, and modulated between σ^+ and σ^- by a photoelastic modulator (PEM) at ∼50kHz. The reflected RMCD signal can then be read out from the photodiode using a lock-in, with the chopper signal used to normalize any intensity fluctuations. As this approach allows for a continuous readout of the RMCD signal - and thus spin/valley polarization - we are now able to explore our parameter space much more effectively.

[2]For review articles discussing the optical properties of monolayer semiconductor TMDs, see Appendix B

We read out RMCD as a function of ν and D, initialized with positive out-of-plane magnetic field $\mu_0 H$, and measured at $\mu_0 H = 0T$ (Figure 3.4a). There is a clear RMCD signal over a broad range of phase space surrounding $\nu = -1$. This finite RMCD at $\mu_0 H = 0T$ indicates spontaneous spin/valley polarization - or ferromagnetism. Parking our gates at $\nu = -1$ and $D = 0$, we measure RMCD signal vs $\mu_0 H$, swept down and up (Figure 3.4b). There is clear hysteresis as a function of magnetic field sweep direction, a hallmark of ferromagnetic order. In (Figure 3.4c&d), we explore the strength of the ferromagnetism, observing hysteresis as a function of temperature. At $\nu = -1$, we see the hysteresis loop disappear at ∼14K, giving us the Curie temperature T_C. Measuring T_C as a function of ν, we observe that the ferromagnetism is strongest near $\nu = -1$, but survives over a broad range of fillings. This is confirmed in measurements of the RMCD hysteresis, ΔRMCD as a function of ν, shown in Figure 3.4e. Ferromagnetism thus exists in the system not only at the $\nu = -1$ correlated insulating state (as can be observed in PL), but also at partial filling of the first moiré valence band. This implies a tuning between a ferromagnetic insulator and a ferromagnetic metal as a function of ν.

The observed ferromagnetic state near $\nu = -1$ can be understood through the real-space picture of hole filling the moiré orbitals in a honeycomb lattice. As discussed, and shown in Figure 3.1b, doped hole wavefunctions at $D = 0$ will have the highest density on the MX and XM high symmetry sites of the moiré unit cell. The hole wavefunctions are layer polarized at these sites, but have significant spatial overlap at other regions of the unit cell - such as at the MM (A) site, which is layer-hybridized. This overlap produces a significant Coulomb exchange, resulting in next-nearest-neighbor ferromagnetic interactions. This drives a spin/valley polarization of the moiré bands. As we will see, the spin-valley polarized moiré valence band is also a topological (Chern) band with Chern number -1, consistent with theoretical predictions [72–74].

3.3 Electric Field Tunable Exchange Interactions

We have now established ferromagnetism near $\nu = -1$, and for $D = 0$. However, it is clear from the RMCD phase diagram (Figure 3.4a) that ferromagnetism disappears as we increase $|D|$. We will now discuss this D-driven phase transition, as well as providing an intuitive picture of why the transition occurs. Similar to the measurement in Figure 3.4e, we measure RMCD vs $\mu_0 H$ swept down, up, and ΔRMCD vs applied displacement field D, at $\nu = -1$. As D increases, the

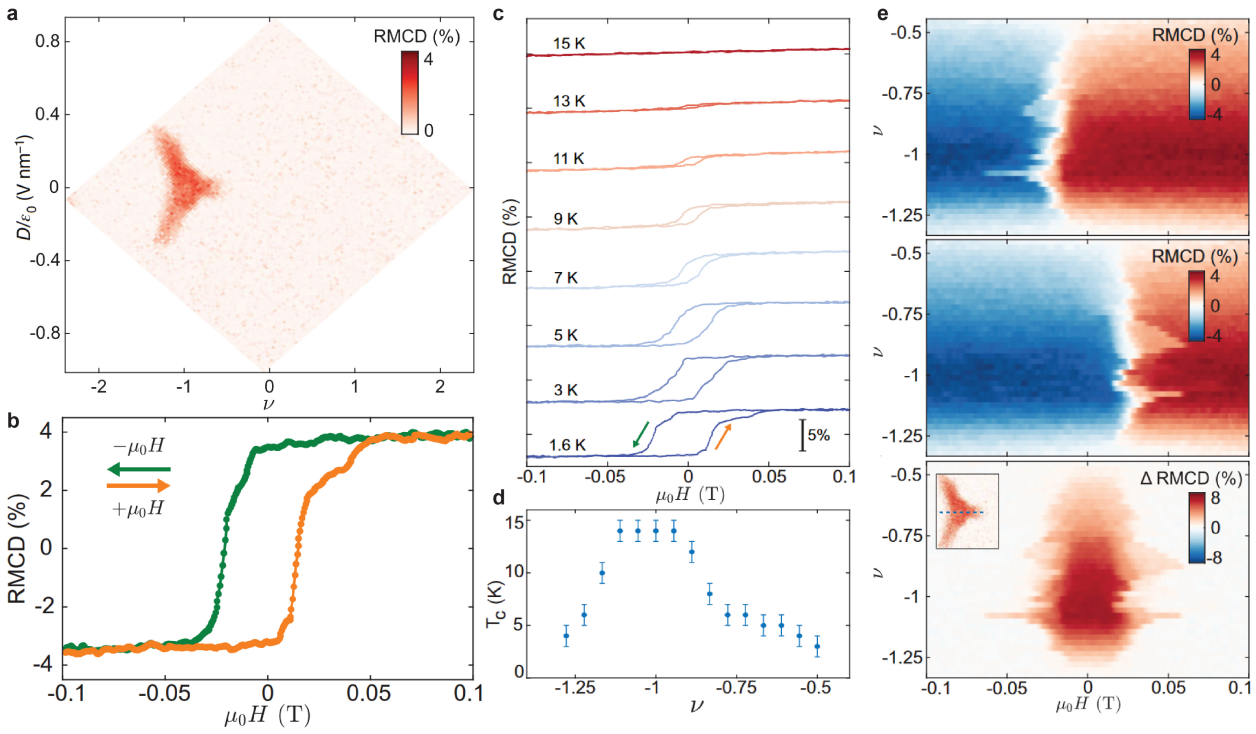

Figure 3.4: Ferromagnetism in moiré $MoTe_2$. **a,** RMCD as a function of ν and D, measured at $\mu_0 H = 0T$. **b,** RMCD hysteresis loop vs $\mu_0 H$, swept down and up, at $\nu = -1$ and $D = 0$. **c,** Temperature dependent RMCD hysteresis. **d,** Curie temperature T_C vs ν at $D = 0$. Error bars correspond to temperature sampling resolution. **e,** RMCD vs $\mu_0 H$ swept down (top) and up (middle), as a function of ν and at $D = 0$. Finite hysteresis ΔRMCD=RMCD$_{down}$-RMCD$_{up}$ is present over a wide range of ν (bottom). Inset: dotted line denotes range of ν shown in (e). Figure adapted from Ref. [51]. Reprinted with permission from AAAS.

hysteresis, indicating ferromagnetism, weakens, and eventually disappears above a critical field of $D_C \approx 0.15 V/nm$ (Figure 3.5a). This behavior is consistent with the disappearing RMCD signal at finite D seen in the dual gate map. The disappearing hysteresis with increasing D also corresponds to a drop in the ferromagnetic Curie temperature T_C, as is shown in Figure 3.5b. These observations are consistent with a weakening of the FM order with increasing D.

To understand the behavior of this system at large $D > D_C$, after the ferromagnetism disappears, we measure RMCD vs $\mu_0 H$ as a function of temperature at $D/\epsilon_0 = 320 mV/nm$ (Figure 3.5c). While there is no hysteresis, we observe a paramagnetic-type response with a saturation at large magnetic field at base temperature of 1.6K. As the temperature increases, the slope of the RMCD vs $\mu_0 H$ near zero magnetic field (which we write as $\left(\frac{\partial R}{\partial H}\right)_{H=0}$) decreases. Using this value

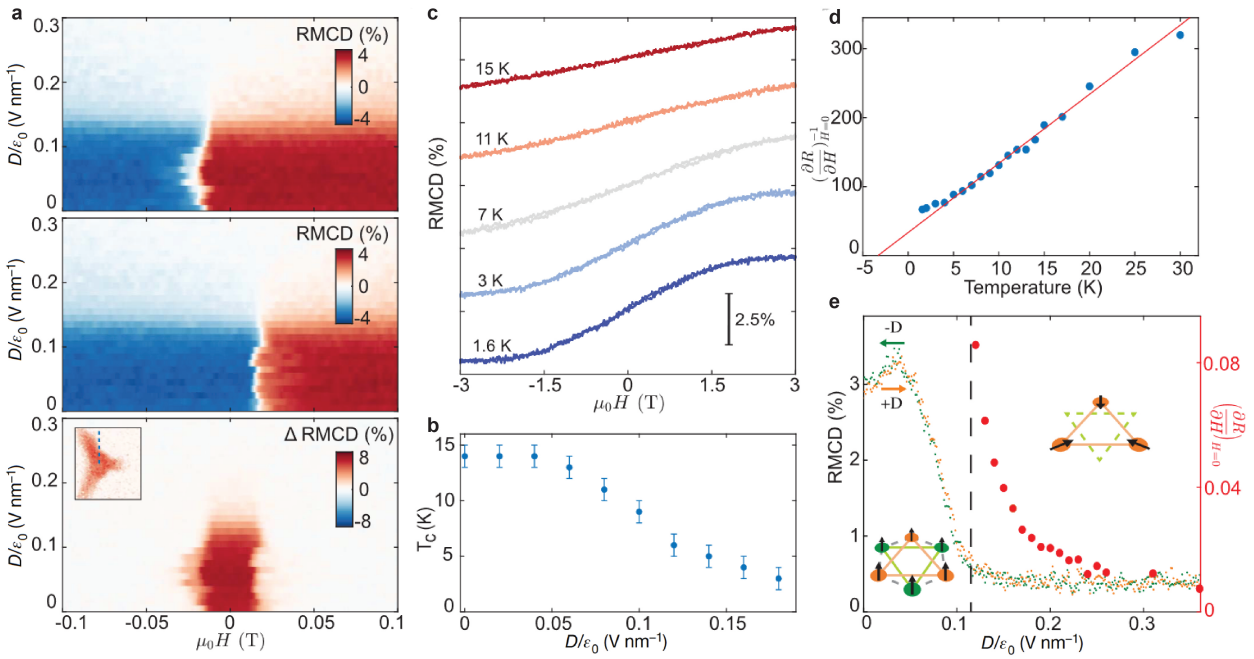

Figure 3.5: D-controlled FM to AFM transition. **a,** RMCD vs $\mu_0 H$ swept down (top) and up (middle), as a function of D. Finite hysteresis ΔRMCD=RMCD$_{down}$-RMCD$_{up}$ is present for small D, up to a critical displacement field of $D_C \approx 0.15 V/nm$ (bottom). Inset: dotted line denotes range of D shown in (a). **b,** Curie temperature T_C vs D. Error bars correspond to temperature sampling resolution. **c,** Temperature-dependent RMCD vs $\mu_0 H$ at large displacement field $D/\epsilon_0 = 320 mV/nm$. The RMCD slope near zero magnetic field, $\left(\frac{\partial R}{\partial H}\right)_{H=0}$, is used as a proxy for susceptibility. **d,** Curie-Weiss fit to $\left(\frac{\partial R}{\partial H}\right)^{-1}_{H=0}$ at selected temperatures at $D/\epsilon_0 = 320 mV/nm$, showing linear dependence and a negative x-intercept, implying AFM interactions. **e,** RMCD ($\mu_0 H = 0$) versus D swept down (green) and up (orange). Red dots are the extracted $\left(\frac{\partial R}{\partial H}\right)_{H=0}$ as D approaches the ferromagnetic phase from the antiferromagnetic interaction side, showing singular behavior. (Insets) The spin arrangements with the antiferromagnetic and ferromagnetic interactions in the (top) triangular and (bottom) honeycomb lattices, respectively. The in-plane spin denotes the superposition of spin up in the K valley and spin down in the K' valley, relative phase corresponding to the in-plane angle. All data were taken at $\nu = -1$, except for data in (e), which was taken at $\nu = -0.9$. Figure adapted from Ref. [51]. Reprinted with permission from AAAS.

as a proxy for the magnetic susceptibility, χ, we can fit the data to the Curie-Weiss law, $\chi = \frac{C}{T-\theta_C}$ [75]. Here, C is a constant, and θ_C is the Curie-Weiss temperature. The extracted $\left(\frac{\partial R}{\partial H}\right)^{-1}_{H=0}$ vs temperature, and the Curie-Weiss fitting, is shown in 3.5d. The extracted data is quite linear down to ~4K, and has a negative intercept, giving $\theta_C = -3.5K$. The negative value of θ_C implies that, at large D, there are antiferromagnetic interactions between the local moments - in contrast to the ferromagnetic interactions at low D.

We can explore the D-driven magnetic phase transition by measuring RMCD at $\mu_0 H = 0$ as a function of D, swept up and down (Figure 3.5e). The data were taken in the slightly underdoped regime ($\nu = -0.9$) to avoid complications from domain effects near $\nu = -1$. The lack of hysteresis as a function of D sweep direction implies a second order magnetic phase transition. Also plotted is the extracted values of $\left(\frac{\partial R}{\partial H}\right)_{H=0}$ (a proxy for susceptibility χ) in the AFM interaction regime. We observe an increasing value of $\left(\frac{\partial R}{\partial H}\right)_{H=0}$ as D_C is approached, with the susceptibility diverging at the same value of D where the $\mu_0 H = 0$ RMCD signal disappears. This singular behavior is also consistent with the interpretation of a second order phase transition.

Our picture of a D-driven honeycomb to triangular superlattice transition can explain this behavior quite nicely. As discussed, at $D = 0$, the doped holes sit on the MX and XM sites with opposite layer polarizations, on a honeycomb lattice with strong Coulomb exchange. This layer-hybridized configuration explains the spontaneous spin-valley polarization - ferromagnetism - observed near $\nu = -1$. However, as we apply an out-of-plane electric field D, we push the doped holes onto a single high symmetry site, as we layer-polarize the system. In the limit of large D, our doped holes sit on only a single moiré orbital, giving us a triangular lattice. This configuration keeps the doped holes well separated, with very little wavefunction overlap. Thus, rather than FM Coulomb exchange, our system is now dominated by superexchange, which produces the observed AFM interactions.

3.4 Proximity Control of Magnetic Exchange

We have established a D-controlled phase transition between the FM phase near $v = -1$ and $D = 0$ and a phase with AFM interactions at large D. However, there is another feature visible in the ferromagnetic phase diagram of Figure 3.4a. As the fully layer polarized system, which is not ferromagnetic, is hole doped further beyond $v = -1$, we see finite RMCD signal, indicating a reemergence of ferromagnetism. RMCD vs $\mu_0 H$ hysteresis sweeps at selected ν and $D/\epsilon_0 = 260 mV/nm$ are shown in Figure 3.6a. Clear hysteresis loops are visible, confirming the reemergence of FM order. Figure 3.6b shows ΔRMCD vs ν, indicating ferromagnetism for for a range of fillings $\nu = -(1 + x)$, centered around $x \approx 0.25$.

This behavior is quite surprising, as at large values of D, the doped holes should be in a triangular lattice with AFM interactions. This reemergence of ferromagnetism, however, indicates

that the hole doping beyond $\nu = -1$ serves as a method for proximity control of the correlated insulating state on a triangular lattice. Figures 3.6c&d illustrate the idea. At $\nu = -1$ and large D, the doped holes sit on a triangular lattice in the top layer. This produces a correlated insulating state with AFM interactions, as discussed previously. The triangular lattice on the bottom layer is empty. This can be understood in the band structure picture as the Fermi level sitting in the Hubbard gap for the top layer, with Coulomb repulsion preventing double filling of the sites. The moiré bands of the empty bottom layer are above the Fermi level.

If we consider hole doping this system beyond $\nu = -1$, the additional holes could either double fill the top layer triangular lattice - costing a large amount of Coulomb energy - or start to fill the moiré bands of the bottom layer. For values of D large enough to layer polarize the $\nu = -1$ system, but not large enough to overcome the Hubbard gap, this will lead to a partial filling of the triangular lattice on the bottom layer. These doped holes contribute a direct Coulomb exchange interaction, providing a competing FM coupling. At finite doping, this FM interaction overcomes the AFM interaction, causing the observed reemergence of ferromagnetism. Thus, for this range of phase space, we can achieve a Mott insulating state in proximity to a doped moiré layer.

Our system contrasts with the proposed gate-tunable exchange interactions of moiré Kondo lattices in TMD heterobilayers [76, 77]. In these cases, the carriers in the conducting layer are not trapped by a moiré potential. However, in our system, the conducting layer is another triangular lattice, which should have a similar trapping potential to the Mott insulating layer. Calculated charge distributions at finite D and $\nu = -1$ and $\nu = -1.3$ are shown in Figure 3.6e. The calculations support this picture of proximity-controlled FM interactions. We see that as holes are doped into a layer-polarized system at $\nu = -1$, they fill the opposite layer and moiré sublattice. This is consistent of our picture of a partially-filled moiré band of the bottom layer upon hole doping, which can mediate the FM interactions.

The discussion so far has been fairly qualitative, as there is not a rigorous microscopic picture of the magnetic phase transitions as a function of D and ν. One possibility in this direction, however, is to build effective spin Hamiltonians using extracted experimental values for the coupling, and then use these model Hamiltonians to explore the evolution of the magnetic ground state [78]. This would augment the experimental results in this system, as our RMCD measurements are only sensitive to out-of-plane spin configuration, as well as AFM interaction strength through Curie-

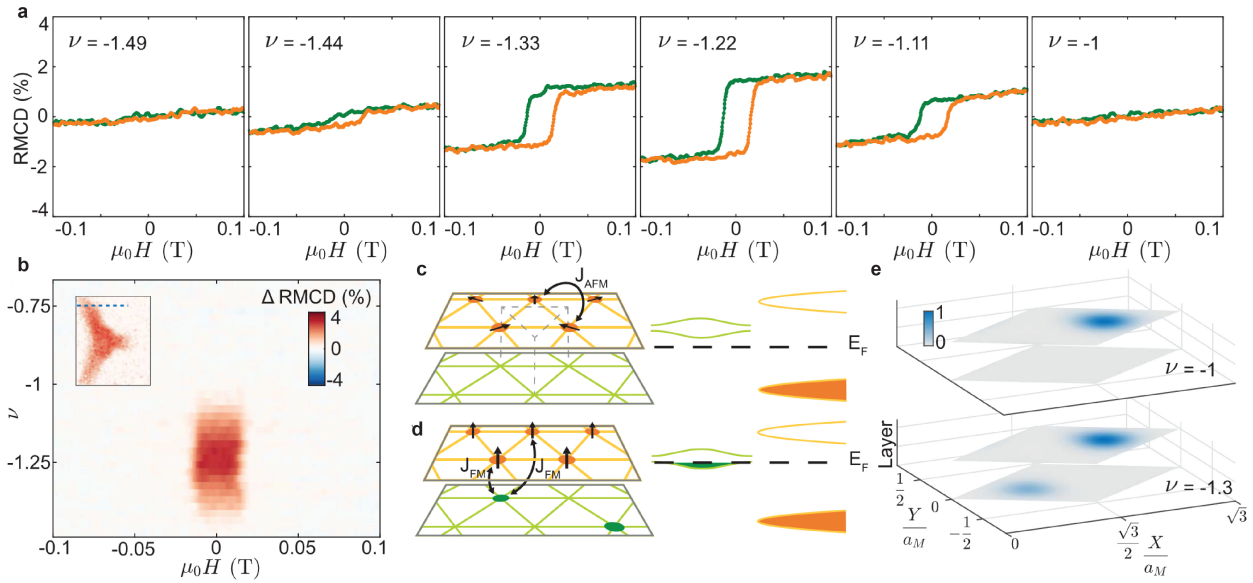

Figure 3.6: Proximity control of magnetic exchange. a, RMCD hysteresis vs $\mu_0 H$ at selected fillings. Inset: dotted line denotes range of ν shown in (a). **b,** ΔRMCD vs ν, showing reemergent ferromagnetism at hole doping beyond $\nu = -1$ at finite D. **c,** (Left) Schematic of twisted bilayer $MoTe_2$ at $\nu = -1$ with full layer polarization. The top layer is a half-filled triangular lattice with antiferromagnetic interactions between the local moments, whereas the bottom layer is unfilled. (Right) Schematic of band alignment. The chemical potential is in the charge gap of the top layer, and the moiré minibands of the bottom layer are empty. **d,** As in (c), but at $\nu = -(1 + x)$. Given that the chemical potential is still in the charge gap of the top layer and the miniband of the bottom layer is partially filled (right), the top layer remains in a half-filled Mott state, whereas the bottom layer becomes a doped triangular lattice. The direct Coulomb exchange of the partially filled B orbitals in this doped layer with the fully filled C orbitals in the top layer gives rise to ferromagnetism. **e,** Calculated charge distribution in the biased condition for $\nu = -1$ (top) and $\nu = -1.3$ (bottom). All data taken at $D/\epsilon_0 = 260mV/nm$. Figure adapted from Ref. [51]. Reprinted with permission from AAAS.

Weiss analysis. Thus, confirming the existence of, for example, 120° Néel order is beyond the capabilities of these techniques.

To sum up, the results presented in this chapter lay the groundwork for the observation of the integer and fractional quantum anomalous Hall effects in moiré $MoTe_2$. As discussed in more detail in Appendix D, observing the FQAH effect requires strong correlations, spontaneous time reversal symmetry breaking, and topologically nontrivial bands. We have experimentally confirmed the first two requirements, and the third was strongly theoretically supported by the time we were taking these measurements. In retrospect, then, perhaps the results presented in the next chapter should not have been too surprising. Nevertheless, seeing the first experimental evidence of the fractional quantum anomalous Hall effect was a shock to us - and, I think, to the rest of the condensed matter community.

Chapter 4

FRACTIONAL QUANTUM ANOMALOUS HALL: OPTICAL PROBES

The experimental results we cover in this chapter are very much a continuation of those in the previous one. We use the same optical probes, RMCD and PL, and study the same system - near 4° twisted AA-stacked bilayer $MoTe_2$. That we are able to observe topological phases - both integer and fractional Chern insulating states - at zero magnetic field is a testament to the importance of sample quality and measurement technique. This fact is known to the fractional quantum Hall community - the cleaner you can make your 2DEG, the more states you tend to see.[1] In any case, measurements on this new, pristine sample, using optimized optical techniques, enabled the first experimental signatures of the zero field FCI - a state which displays the fractional quantum anomalous Hall effect.

Finding the zero field FCI came as a surprise. Our goal initially was to observe a zero field Chern insulating state - that is, a state which displays the quantum anomalous Hall effect. As QAH relies on combining spontaneous time reversal symmetry breaking and topology [9, 16, 79], moiré $MoTe_2$ is a good candidate system. This approach proved successful in both magnetically doped [16, 79] and intrinsic [48] topological insulators. Moiré engineering promised another approach to fulfill these requirements. Indeed, QAH had already been observed in moiré graphene [29, 30, 80] and heterobilayer TMD moirés [32]. However, it was predicted that adding in strong electron-electron interactions would also allow zero field FCI states[2] to emerge [10, 12–14, 28]. These states show the fractional quantum Hall effect, and could host fractional excitations,[3] including non-Abelian anyons - crucial to achieve topological quantum computation [81].

While both FQH and FQAH appear in strongly correlated topological phases [2, 4, 7, 10, 12–14, 82], FQAH requires spontaneous time reversal symmetry breaking, and does not rely on the

[1] as we discuss in Appendix C

[2] Appendix D

[3] Appendix E

formation of Landau levels by a large applied magnetic field. Avoiding this requirement of a large field is, of course, a major advantage, but despite extensive theoretical work, no physical system had been found which could host the FQAH effect. There had been tantalizing hints that moiré superlattices were the right place to look for zero field FCIs, however. FCIs had been observed in bilayer graphene/hBN superlattices under a 30T magnetic field [83], as well as in magic angle twisted bilayer graphene down to only 5T [84].

One reason why moiré systems, and moiré TMDs in particular, are such a promising place to search for zero field FCIs is that realizing the Haldane model on a honeycomb lattice with strong correlations can lead to flat topological bands which share key characteristics of Landau levels, but at zero applied magnetic field [15, 85]. Recent theory work [44, 45, 56–59] had predicted near-AA stacked twisted TMD homobilayer systems to host flat topological bands, with opposite Chern numbers for the two different spin/valley sectors. Considering the results shown in the previous chapter, moiré $MoTe_2$ was a promising system to look for not only zero field CIs, but zero field FCIs as well.

In this chapter, we show that near 3.7° moiré $MoTe_2$ hosts topological bands and spontaneously breaks time reversal symmetry, realizing a Haldane model on a honeycomb lattice, with complex next nearest neighbor hopping and strong Coulomb interactions (Figure 4.1a). We observe robust ferromagnetism corresponding to insulating states at both integer and fractional fillings of the first spin/valley polarized moiré valence band. Using photoluminescence as a probe of the insulating states, we measure the topological invariants of the states at integer filling, $\nu = -1$, and fractional fillings, $\nu = -2/3$ and $\nu = -3/5$. Evidence of the zero field FCIs is obtained by comparing with the predictions of the Streda formula. With further analysis, an additional state at $\nu = -4/7$ is also visible. Last, we show that the states can be driven into the trivial regime by application of an out-of-plane electric field, D.

4.1 Ferromagnetic Insulating States at Fractional Fillings

As in the previous chapter, we can use trion PL as a probe of correlated insulating states in our moiré $MoTe_2$ system. In this higher-quality sample, we observe a much cleaner and sharper PL signal on the hole doping side (Figure 4.1b). Here, there is a substantial blueshift and clear suppression of the trion PL at $v = -1$, but also a smaller feature at $v = -2/3$. Another PL measurement,

taken with finer resolution around the fractional feature, reveals not only a decrease in PL intensity at $v = -2/3$, but another, smaller decrease at $v = -3/5$ - both of which occur at zero applied magnetic field (Figure 4.1c). Because the opening of a gap when the insulating state is formed causes the decrease in the trion PL, because the free carriers are consumed, the strength of the PL suppression should give some indication of the strength of the correlated insulating states. With this interpretation, the integer state at $\nu = -1$ is quite robust, the fractional state at $v = -2/3$ less so, and the state at $v = -3/5$ weaker than the one at $v = -2/3$.

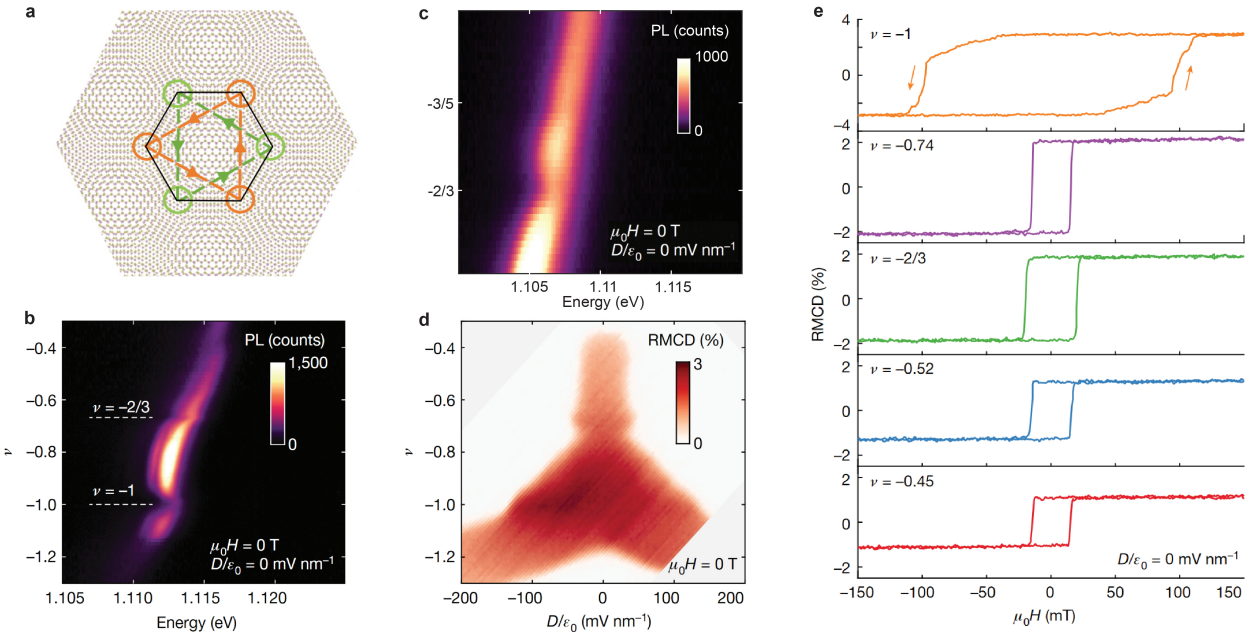

Figure 4.1: Ferromagnetic insulating states at fractional filling. a, Honeycomb moiré superlattice. Next nearest neighbor hopping (dotted lines) is complex, realizing the Haldane model. **b,** Spectrally-resolved PL intensity vs filling, with integer and fractional correlated insulating states indicated. **c,** As in (b), but zoomed in on fractional features. State at $\nu = -3/5$ is visible. **d,** RMCD vs ν and D. Enhancement of ferromagnetic D_C is visible around $\nu = -2/3$. **e,** RMCD hysteresis sweeps at selected ν. Enhancement of ferromagnetic H_C is visible at $\nu = -2/3$. Figure adapted from Ref. [86]. Reproduced with permission from Springer Nature.

We now turn to RMCD which, as discussed in the previous chapter, serves as an optical probe of ferromagnetic order. Figure 4.1d shows a measurement of RMCD at zero applied magnetic field as a function of ν and D - similar to that shown in Figure 3.4a, but on the new sample. While the basic shape of the FM phase space is similar to the previous measurement, we observe a clear

enhancement of the critical electric field D_C of the ferromagnetism around $\nu = -2/3$, the same filling that we see the correlated insulating state in the PL measurement. As we know that applying D suppresses the ferromagnetism in this system, it appears that ferromagnetism is enhanced at this fractional insulating state.

Taking RMCD hysteresis sweeps vs magnetic field can give us another indication of the strength of the ferromagnetism as a function of ν. In Figure 3.4e, we see a large hysteresis loop at $\nu = -1$, with a critical magnetic field H_C of approximately 100mT. This is noticeably larger than the H_C of the previous measurement, suggesting that a cleaner sample produces more robust ferromagnetism. Tuning to different fillings, we see that H_C becomes smaller as we move away from $\nu = -1$ - ie, when we partially fill the moiré band. However, H_C is enhanced at $\nu = -2/3$, another sign of stronger ferromagnetism at this filling.

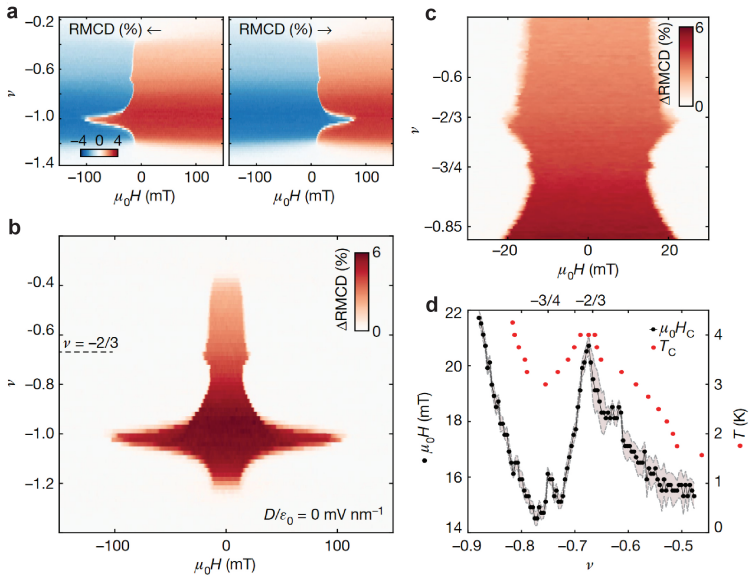

Figure 4.2: Enhancement of ferromagnetism at fractional filling. **a,** RMCD vs $\mu_0 H$ swept down (left) and up (right) as a function of filling ν. **b,** Difference between down and up sweeps, ΔRMCD. Enhancement of $\mu_0 H_C$ is visible at $\nu = -1$ and $\nu = -2/3$. **c,** As in (b), but with finer resolution around fractional features. Clear enhancement around $\nu = -2/3$ is visible, as well as a small enhancement around $\nu = -3/4$. **d,** $\mu_0 H_C$ and T_C vs ν. $\mu_0 H_C$ extracted from data in (c) by change point detection, with the shaded area denoting the extracted transition width. T_C extracted from temperature dependent RMCD hysteresis sweeps, as in Figure 3.4. Extracted T_C values have an uncertainty of 0.25K, from the temperature step size of the measurement. Figure adapted from Ref. [86]. Reproduced with permission from Springer Nature.

A measurement of the RMCD hysteresis as ν is tuned continuously is shown in Figure 4.2a-c. We see that not only is there a large enhancement of $\mu_0 H_C$ around the insulating state at $\nu = -1$, but also an increase in the critical field near $\nu = -2/3$, consistent with Figure 4.1e. A finer measurement of ΔRMCD around the fractional filling is shown in Figure 4.2c. In addition to the clear enhancement around $\nu = -2/3$, we also see a small increase of the critical field at $\nu = -3/4$. This is quite a weak feature, and whether it

appears at all changes from spot to spot on the sample. In contrast, the $\nu = -2/3$ feature is very robust and repeatable.

We can extract the critical field, $\mu_0 H_C$, from these hysteresis sweeps as a function of ν, plotted in Figure 4.2d. A clear enhancement is apparent at $\nu = -2/3$, and the small feature at $\nu = -3/4$ is also visible. Also plotted is the Curie temperature, T_C, extracted from temperature dependent RMCD hysteresis measurements in a similar manner to Figure 3.4. These data also show a maximum at $\nu = -2/3$. Thus, we see an enhancement of D_C, $\mu_0 H_C$, and T_C at the correlated insulating state appearing at $\nu = -2/3$, indicating that not only is this state ferromagnetic, but its ferromagnetism is actually enhanced compared to the surrounding metallic regions.

4.2 The Streda Formula and Optical Landau Fans

Having established that the integer and fractional correlated insulating states are ferromagnetic, the question now arises - are they topological? The most straightforward experimental signature of the topology would be to measure a quantized Hall conductivity (as we will discuss in the next chapter). However, semiconducting TMD systems are notoriously difficult to probe using transport, as forming good electrical contact to them is nontrivial. Luckily, there is another method for determining topological invariants - the so-called Landau fan diagram.

A Landau fan diagram is a measurement of the carrier density at which an insulating state appears as a function of applied magnetic field. A gapped state with nontrivial topology will disperse linearly with applied field, with a slope corresponding to the topological index. To understand why this is the case, we will make a brief digression, and discuss the Streda formula [87]:

$$\sigma_H = \frac{\partial \rho}{\partial B} \tag{4.1}$$

Here, σ_H is the Hall conductivity, ρ is the density, and B is the magnetic field. One way of seeing why this relation follows straightforwardly from a gapped state with Hall conductivity σ_H is as follows.[4] If we have a gapped topological phase, contribution to the current will come only from the Hall conductivity term:

$$j_i = \sigma_H \epsilon_{ij} E_j \tag{4.2}$$

[4] argument adapted from Ref. [88]

We can plug this in to the continuity equation, and apply Maxwell's equations, to get

$$\frac{\partial \rho}{\partial t} = -\nabla \cdot j = -\sigma_H(\partial_x E_y - \partial_y E_x) = \sigma_H \frac{\partial B}{\partial t} \tag{4.3}$$

Eliminating the time derivatives from both sides gives equation 4.1. We can see that, making very few assumptions, a finite quantized Hall conductivity (the hallmark of a topological state) will correspond to a linear density dispersion as a function of B, with the slope corresponding to the topological index.

We rewrite the Streda formula as

$$C = \phi_0 \frac{\partial n}{\partial B} \tag{4.4}$$

where C is the Chern number in units of Hall conductance e^2/h, ϕ_0 the magnetic flux quantum, and n the carrier density of our gapped state. Using this, it becomes possible to extract the Chern number (integer or fractional) from the measured slope in a Landau fan diagram. This approach has been used extensively in moiré systems, and can be used with various probes sensitive to gapped states [84, 89]. For our measurement, we take advantage of the sensitivity of the trion PL emission intensity to the formation of gapped states. As discussed in the previous chapter, excitons in TMDs are sensitive to any changes in the local dielectric environment (by the formation of a correlated insulating state, for instance) [90]. They have been used as a probe of charge gaps of generalized Wigner crystals in TMD moirés [31, 33] as well as fractional quantum Hall states in graphene [91]. A similar approach has also been used to measure fractional quantum Hall liquids in GaAs quantum wells [92].

A corollary of equation 4.4 is that a topologically trivial state with Chern number of 0 should not disperse with applied magnetic field. Luckily, we have a way to measure the density of the insulating states in our system using the features in trion PL. So, an obvious first check for nontrivial topology would be simply to measure PL at different applied fields, and see if there is any shift in the insulating states. This measurement is shown in Figure 4.3. By eye, it is clear that the features at $\nu = -1$ and $\nu = -2/3$ are both shifting with magnetic field. In addition, these shifts appear to be roughly linear with applied field.

However, it is difficult to extract any quantitative value for the slope, and thus an estimate for the Chern number, from these single PL sweeps. To address this, we can integrate the PL intensity over the trion peak, for each value of ν, for a given magnetic field. Because the formation of an

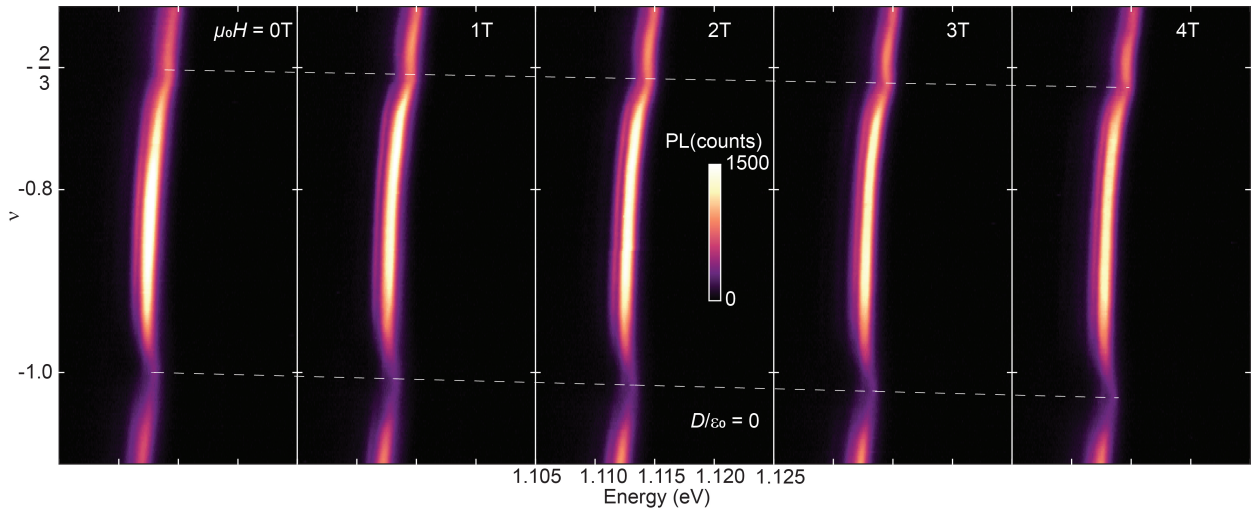

Figure 4.3: PL shift with magnetic field. Spectrally resolved trion PL vs ν at selected magnetic fields. A clear shift is visible for both the integer and fractional correlated insulating states. Dashed lines are guides to the eye. Figure adapted from Ref. [86]. Reproduced with permission from Springer Nature.

insulating state decreases the total trion emission, the position of the states will appear as a dip in this integrated PL vs ν. This condenses the information of the PL vs ν for a given magnetic field $\mu_0 H$ into a single line, and we are now able to plot a color map of integrated PL vs ν and $\mu_0 H$. That is, using trion PL as a probe, we can extract an *optical* Landau fan diagram.

This Landau fan is shown in Figure 4.4a. The insulating states are clearly dispersing, and the dispersion with field is linear, as would be expected from the Streda formula prediction. In addition, the feature corresponding to the $\nu = -2/3$ state appears to be dispersing with a shallower slope than the state at $\nu = -1$. Looking again at equation 4.4, we see that a larger dispersion corresponds to a larger Chern number. If the state at $\nu = -1$ has a Chern number $C = -1$, as we expect for a fully filled topological band, the fact that the fractional state disperses with a shallower slope implies that it has a *finite Chern number between 0 and -1*!

We are more quantitative in Figure 4.4b. Here, we show a Wannier diagram - the linear dispersions predicted by the Streda formula for states with Chern number C and emanating from filling ν, labelled as (C,ν). Overlaid on these predicted dispersions are the extracted carrier densities for the features at $\nu = -1$, $\nu = -2/3$, and $\nu = -3/5$. Details of the process for extracting the density values are discussed in Appendix A. As can be seen by comparing the extracted density values with the Streda slopes, the $\nu = -1$, $-2/3$, and $-3/5$ state dispersions match well with Chern numbers

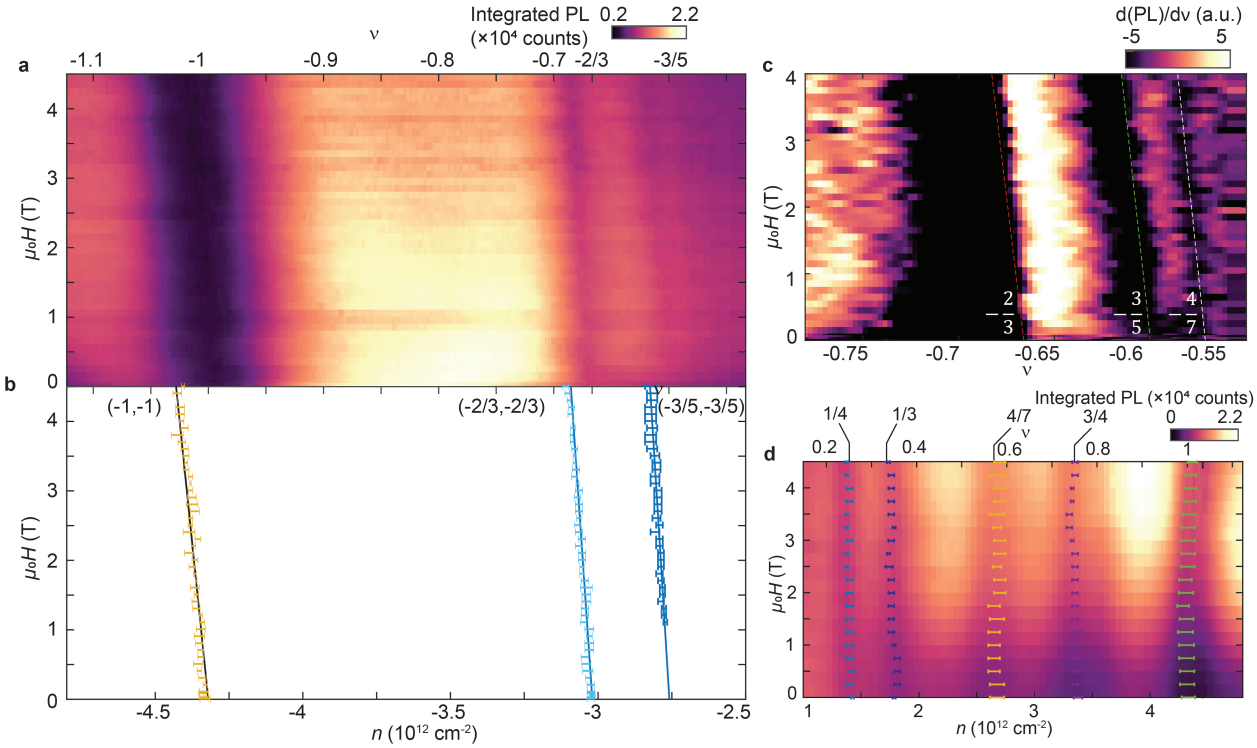

Figure 4.4: Optical Landau fan diagram. a, The optical Landau fan diagram of integrated trion PL vs density and magnetic field. Clear, linear dispersion is visible for both the integer and fractional features. Both the $\nu = -2/3$ and $\nu = -3/5$ states are visible in this diagram. **b,** Wannier diagram, with lines derived from the Streda formula dispersion corresponding to (C,ν) of (-1,-1) for the integer state (black) and (-2/3,-2/3) and (-3/5,-3/5) for the fractional states (blue). Overlaid data are carrier densities for the three insulating states extracted from (a) (see Appendix A). **c,** As in (a), but with a numerical derivative of the integrated PL taken vs filling. With this additional processing, the fractional features become more clear, and an additional state at $\nu = -4/7$ becomes visible. **d,** As in (a), but on the hole doping side, where there is no ferromagnetic order. While correlated insulating states are visible at both integer and fractional fillings, none disperse with field - the states are topologically trivial. Extracted carrier densities are overlaid. Figure adapted from Ref. [86]. Reproduced with permission from Springer Nature.

$C = -1$, $-2/3$, and $-3/5$, respectively. More precisely, a linear fit to the extracted densities yields $C = -0.95(7)$, $C = -0.63(4)$, and $C = -0.59(4)$.

Observing a $C = -1$ dispersion, while interesting, is not a massive surprise. This dispersion is strong evidence for the ferromagnetic insulating state at $\nu = -1$ being a quantum anomalous Hall state (or a topological Mott insulating state [85]). As discussed previously, this system, which combines topological bands with spontaneous time reversal symmetry breaking, should realize the Haldane-Hubbard model [9, 44, 56, 59, 85, 93], where a state with $C = -1$ is expected.

However, states dispersing with a slope corresponding to a *fractional* Chern number were quite unexpected. From our discussion of the Streda formula, this dispersion corresponds to a fractional Hall conductance. As these states survive down to zero magnetic field, this is a signature of states displaying the fractional quantum anomalous Hall effect.

These states can be identified as zero field fractional Chern insulators. Unlike the fractional quantum Hall states observed in partially filled Landau levels, FCIs can display fractionally quantized Hall conductance and host fractionalized quasiparticle excitations at zero magnetic field, in a partially filled topological Bloch band. In Figure 4.4c, we show the same data as in 4.4b, but with a numerical derivative of the integrated PL taken vs ν. This additional processing makes the fractional states clearer, and reveals an additional dispersing feature at $\nu = -4/7$. Thus, not only do these states disperse with slopes corresponding to fractional values of the Hall conductance, but their filling factors match with the first three values of the Jain sequence for the fractional quantum Hall states [5]. Subsequent exact diagonalization calculations yielded results consistent with the assignment of these states as zero field FCIs [73, 94].

To serve as a control, we show the optical Landau fan diagram of the electron doping side in Figure 4.4d. Recall from RMCD measurements that there is no ferromagnetism on the electron side - no topological states are expected. While we do see correlated insulating states for a number of fractions, none show any clear dispersion with magnetic field, and the extracted carrier densities (overlaid) have no obvious field dependence. Thus, as we expect, these electron side states are topologically trivial.

4.3 Electric Field Driven Topological Phase Transitions

In the previous chapter, we discussed the tuning of moiré superlattice geometry with the application of an out-of-plane electric field, D. In tuning from the honeycomb to the triangular lattice of doped holes, ferromagnetism is destroyed, and the magnetic interaction changes sign. The topological states observed rely on both spontaneous time reversal symmetry breaking and nontrivial band topology (arising from the complex second nearest neighbor hopping on the honeycomb lattice). Therefore, we should expect that applying a large value of D would affect the states.

PL vs ν for $D/\epsilon_0 = -250mV/nm$, at selected magnetic fields, is shown in Figure 4.5a. This is the large D limit where we have fully layer polarized the system and tuned to a triangular lattice,

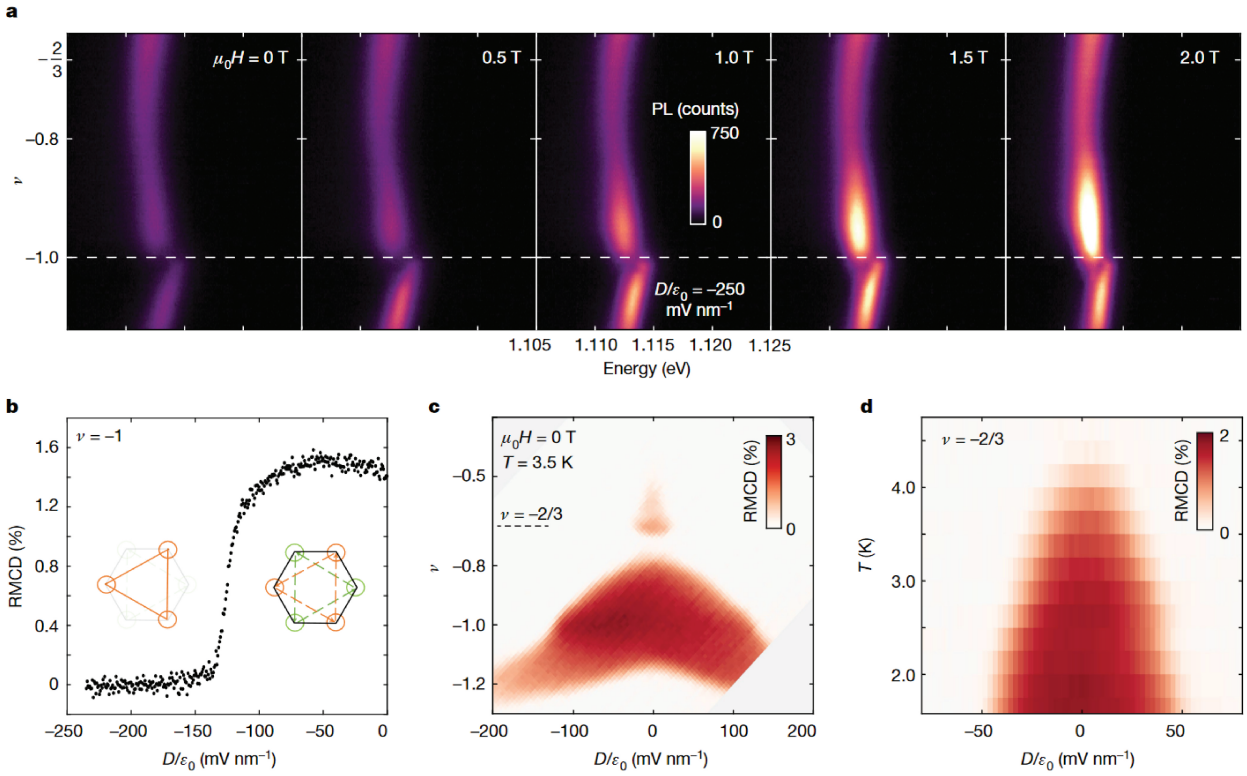

Figure 4.5: Electric field tuning of topology. a, As in Figure 4.3, but with a large applied displacement field, $D/\epsilon_0 = -250mV/nm$. No signature of a state at $\nu = -2/3$ is visible, and the insulating state at $\nu = -1$ does not disperse with field - the state becomes topologically trivial. **b,** RMCD at $\mu_0 H = 0$ at $\nu = -1$ vs D. A drop in RMCD signal is visible as the magnitude of D/ϵ_0 increases through a critical electric field of $-125mV/nm$, concurrent with a change in lattice geometry (insets). **c,** RMCD vs ν and D at $T = 3.5K$. Here, we see that ferromagnetism survives for an island near $\nu = -2/3$, due to the enhanced strength of the ferromagnetism around the zero field FCI state. **d,** RMCD vs D and T at $\nu = -2/3$. Figure adapted from Ref. [86]. Reproduced with permission from Springer Nature.

as we can see from the disappearance of magnetism in Figure 4.5b, as well as from the full FM phase space shown in Figure 4.1d. In this limit, while we can observe an insulating state at $\nu = -1$, the fractional state has disappeared. The PL intensity is enhanced as magnetic field is applied, possibly due to spin polarization enhancing trion recombination and emission. However, the key observation is that the $\nu = -1$ state shows no clear shift with magnetic field. Thus, the state is topologically trivial, as is to be expected for a Mott insulating state on a triangular lattice. Thus, we not only have both integer and fractional Chern insulating states at zero magnetic field in our $MoTe_2$ moiré, but these states can be driven into the topologically trivial regime by the application

of an electric field.

Figures 4.5c&d show the phase space over which ferromagnetism exists for the $\nu = -2/3$ state. We see that the Curie temperature is enhanced for a region of phase space around $\nu = -2/3$, as evidenced by the island of ferromagnetism at $T = 3.5K$. RMCD as a function of D and T shows the ferromagnetism survive even beyond 4K for $D = 0$ at $\nu = -2/3$. These data suggest that the fractional insulating state thermodynamically stabilizes ferromagnetism. As the formation of the zero-field FCI relies upon the spontaneous time reversal symmetry breaking supplied by the ferromagnetism, this large Curie temperature is very encouraging. As the fractional quantum Hall states observed in the partially filled Landau levels of 2DEGs are generally observed at mK temperatures, seeing a zero field FCI survive to multiple Kelvin is quite good.

The fractional states in the moiré $MoTe_2$ system have proven robust in other ways, as well. Beyond the high critical temperatures observed in this device, the fractional states are extremely repeatable, appearing in dozens of devices fabricated in our group. They also survive over a range of twist angles. This device is $\sim 3.7°$, but we have observed the $\nu = -2/3$ FCI state even down to $\sim 2.7°$. Changing the twist angle could certainly change the physics - as many theoretical works have explored since this experimental discovery [58, 73, 94–119] - but there doesn't seem to be a "magic angle" in this system, away from which no interesting physics appears. The fact that these states appear in many optical devices made in our lab (and, as we discuss in the next chapter, transport devices as well), in addition to the fact that our observations have since been replicated by other groups [120], serves as a testament to the robustness and repeatability of the zero field FCIs in this system.

The results discussed over the course of this chapter serve as the first experimental signature of the fractional quantum anomalous Hall effect. The observation of states hosting the FQAHE - zero field FCIs - created tremendous excitement in the condensed matter community. This excitement has mainly been due to the fact that these states should host anyonic quasiparticle excitations, in a lattice system at zero magnetic field. While the states observed thus far are predicted to host Abelian anyons, the moiré $MoTe_2$ holds great promise in the search for additional zero field FCIs hosting non-Abelian anyons. These exotic quasiparticles are the key to topologically protected quantum computation. In addition, the flexibility of vdW heterostructure devices means that hybridizing these FCIs with other systems, such as superconductors, could provide another route

to non-Abelian states.

As exciting as this is, and as compelling as the fractional Streda dispersion data are, we are still missing the "smoking gun" - fractionally quantized Hall conductance. For this, we need electrical transport measurements - a notoriously tricky problem for semiconducting TMDs. As we will see in the next chapter, a clever new device architecture allowed us to overcome this obstacle. The resulting transport measurements provide incontrovertible proof that moiré $MoTe_2$ displays the fractional quantum anomalous Hall effect.

Chapter 5

FRACTIONAL QUANTUM ANOMALOUS HALL: TRANSPORT PROBES

One of the most striking features of quantum Hall measurements is the degree of accuracy to which the Hall resistance can quantize.[1] In fact, the first measurement of the integer quantum Hall effect in 1980 was proposed as a method for precision measurement of the fine structure constant [1]. The exact quantization of R_{xy} is quite surprising, given that experimental systems are never perfect, measurements take place at finite temperature, perfectly isolating the sample from the environment is impossible, etc. Indeed, solving the puzzle of this perfect quantization was what led to the current understanding of these phases in terms of their topology.

The Streda formula for gapped topological states - as discussed in the previous chapter - can be derived directly from the fact that the Hall resistance is quantized, with very few additional assumptions. This allows for Landau fan diagrams to serve as a useful probes of topological states and their topological invariants. However, the gold standard for experimental confirmation of topological states remains a direct measurement of Hall resistance. If there is a quantized plateau in R_{xy} vs ν, with R_{xx} dropping to zero, this is a clear confirmation of quantum Hall. Retaining this quantization at zero applied magnetic field (ie, seeing a quantized hysteresis loop in R_{xy}) implies the quantum anomalous Hall effect. If R_{xy} is quantized to a *fractional* value of h/e^2, and shows a hysteresis loop, this is the fractional quantum anomalous Hall effect.

Unfortunately, performing transport measurements on semiconducting TMDs has always been difficult. The major challenge lies in forming transparent electrical contacts to these systems. Generally, the interface between a metal contact and the TMD will have a large Schottkey barrier, producing a huge contact resistance and making transport measurements impossible. One solution to this has been using a dual gated heterostructure with the top gate covering the metal contact region [42, 43]. Setting the top gate to heavily hole dope the system aligns the Fermi level of the

[1] Recent precision measurements of the quantum Hall effect using graphene have reached accuracies better than one part per billion [121]!

TMD with the metal contact, allowing for a reasonable contact resistance in the range of 10s of kΩ. There is a major drawback of this architecture, however. The large voltage that must be applied to the top gate so the contacts will turn on restricts the accessible range of phase space to large ν and D. Early transport measurements using this device architecture are shown in Figure 5.1. We know from the optical measurements shown in the last two chapters that the topological states occur near $D = 0$, and are suppressed at large D. A completely new device architecture was needed.

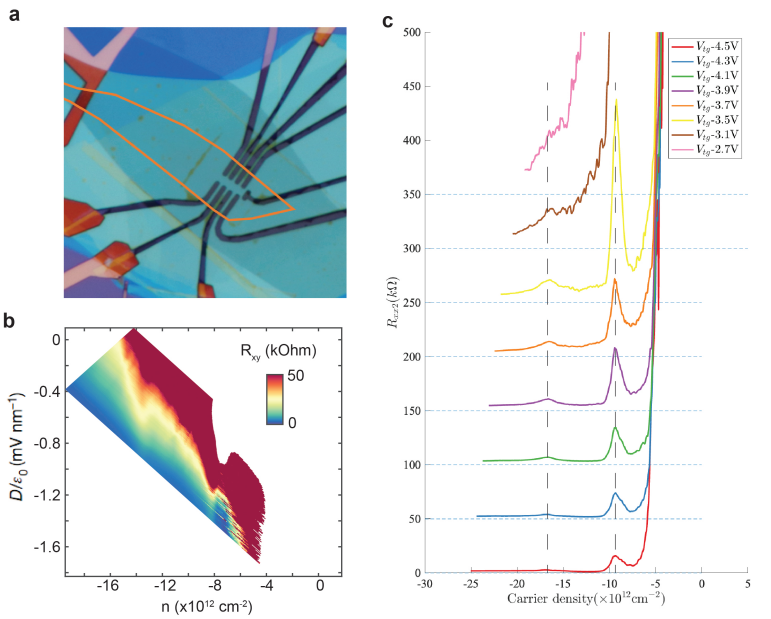

Figure 5.1: Transport device architecture 1.0. **a,** Early transport device image. Top gate outlined in orange. **b,** Hall resistance R_{xx} vs D and carrier density. While correlated insulating states are visible at $n = -8 \times 10^{-12}$ and $n = -14 \times 10^{-12} cm^{-2}$, $D = 0$ cannot be reached for low carrier density as contacts become very resistive (red region). **c,** Sweeps of R_{xx} vs carrier density, at selected gate voltages, showing resistance peaks from correlated insulating states. Data taken at 2K. Sweeps offset for clarity.

In this chapter, we will discuss the solution to this problem, allowing for transport measurements over the entire relevant phase space on the hole doping side, where the integer and fractional Chern insulating states occur. These measurements show precisely what is expected for fractional Chern insulators - plateaus quantized at fractional values of R_{xy} at the appropriate fillings ν, R_{xx} dropping to nearly 0, and quantized hysteresis of R_{xy} vs applied magnetic field. This was the first experimental observation of the fractional quantum anomalous Hall effect. In addition to the zero field FCI states, we observed a linear increase in R_{xy}, with the value passing through $2h/e^2$ at $\nu = -1/2$. This behavior resembles that of the composite Fermi liquid in the half filled lowest Landau level [5, 6, 122–126]. The CFL in the half filled LLL can be understood as the parent state of not only the Abelian Jain sequence states, but those believed to be non-Abelian as well. Thus, not only do these measurements provide the first experimental confirmation of FCIs expected to host zero-field anyons, but also give tantalizing hints towards the "anomalous CFL" - which could possibly serve

as the parent of zero-field non-Abelian anyons.

5.1 Device Architecture and TMD Transport

The key to transport measurements of the FQAHE was the new device architecture developed after the observation of the zero field FCIs with optics. The device, shown schematically in Figure 5.2, incorporates three separately controllable gates. The twisted $MoTe_2$ bilayer is picked up with a thin layer of BN, using the tear-and-stack method, and placed on top of a prepatterned bottom gate with Pt contacts. An additional round of lithography and metal deposition creates the Pt contact gate, which is aligned to sit on top of the contact area. A final transfer adds the top gate. This design enables a large hole doping directly around the contacts, which aligns the Fermi levels of the $MoTe_2$ and the Pt. However, the contact gate does not reach into the main channel of the device where the current is flowing. This channel is controlled only by the top and bottom gate voltages, V_{tg} and V_{bg}. Therefore, it is possible to tune the device over the entire region of the hole doping phase space - including to $D = 0$ - without the contacts turning off.

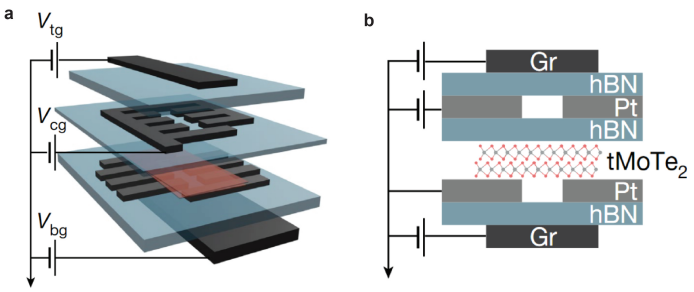

Figure 5.2: Transport device architecture 2.0. a, Schematic of $MoTe_2$ transport device, with additional set of contact gates used to control contact doping. **b,** Side view. Figure adapted from Ref. [127]. Reproduced with permission from Springer Nature.

Dual gate maps of the longitudinal resistance R_{xx} and Hall resistance R_{xy} are shown in Figure 5.3. All transport measurements are taken at 100mK unless otherwise specified. R_{xx} and R_{xy} are symmetrized and anti-symmetrized, respectively, at $\mu_0 H = \pm 200mT$. These phase diagrams are clearly much nicer than the one shown in Figure 5.1, and the behavior at $D = 0$ is accessible. Comparing to the RMCD map in Figure 4.1d, we can see that the general triangular outline and the symmetry around $D = 0$ is the same, but clearly there are many more features visible. The most important of these are the large values of $|R_{xy}|$ and small R_{xx} in the regions near $\nu = -1$ and for filling below $\nu = -2/3$, at small D. Though we will explore these regions more quantitatively in the next sections, it can be seen even in these dual gate maps that $|R_{xy}|$ is near 1 (in units of

h/e^2) over a broad plateau around $\nu = -1$. In addition, $|R_{xy}|$ exceeds 1 in the region around and below $\nu = -2/3$. A dip in $|R_{xy}|$ is also visible slightly below $\nu = -2/3$. These large values of $|R_{xy}|$ indicate the emergence of topological states.

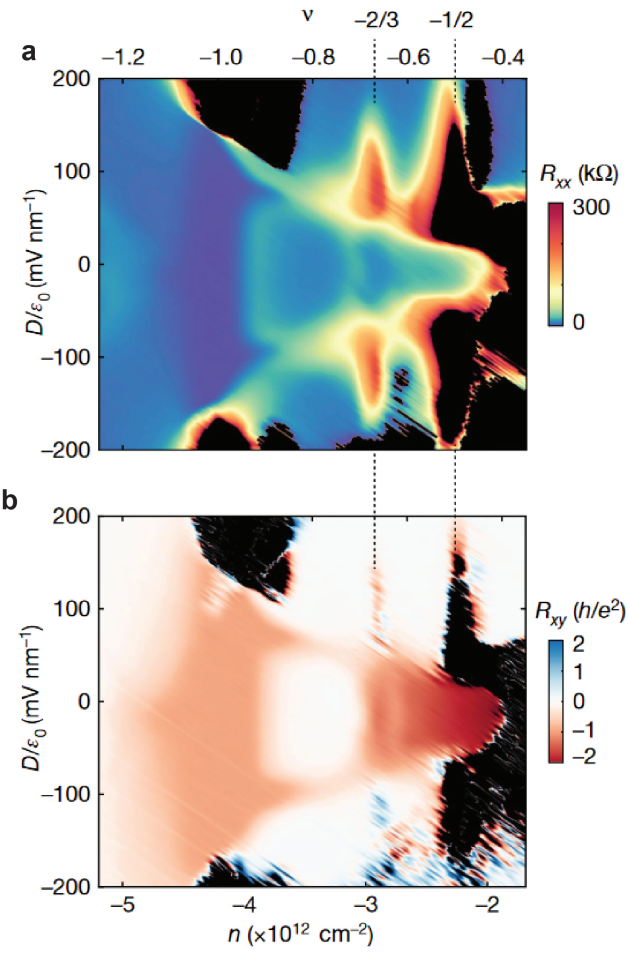

Figure 5.3: Transport phase diagram. a, Longitudinal resistance R_{xx} vs electric field D and carrier density n. Filling factor ν is shown on top axis. Black regions are too insulating to be reliably measured **b,** As in (a), but for Hall resistance R_{xy}. R_{xx} and R_{xy} are symmetrized and anti-symmetrized, respectively, at $\mu_0 H = \pm 200mT$. Figure adapted from Ref. [127]. Reproduced with permission from Springer Nature.

We can check for consistency with our earlier optical measurements of the topological states discussed in Chapter 4. In Figure 5.4, we show a Landau fan diagram of $|R_{xy}|$. It is clear that both the integer and fractional features disperse with $\mu_0 H$. The overlaid black and blue dashed lines are the dispersions predicted by the Streda formula for Chern numbers $|C| = 1$, $2/3$, and $3/5$ for $\nu = -1$, $-2/3$, and $-3/5$, respectively. Thus, our transport measurements are consistent with the dispersions observed using optics. With transport, though, there are additional methods to determine the topology of the states - namely, measurement of quantized R_{xy}.

5.2 Integer Quantum Anomalous Hall Effect in $MoTe_2$

Figure 5.5a shows the measurement of the quantum anomalous Hall effect at $\nu = -1$, and its tunability as a function of applied electric field D. At $D/\epsilon_0 = 0$, in the fully layer hybridized regime, a clear hysteresis loop in the Hall resistance R_{xy} is visible as a function of $\mu_0 H$. R_{xy} is quantized to h/e^2, and remains quantized down to zero field. In addition, the longitudinal resistance R_{xx} is vanishing, with small increases at the critical magnetic field where R_{xy} flips. These are clear signatures of QAH, for an insulating state with a Chern number $C = -1$, as we expect. The

quantized R_{xy} is stable for moderate applied electric field, with decreasing critical magnetic field H_C. Above $D/\epsilon_0 \approx 150mV/nm$, however, R_{xy} decreases and R_{xx} substantially increases, indicating a tuning out of the Chern insulating state.

We explore this transition in the behavior of R_{xy} and R_{xx} as D is continuously tuned in Figure 5.5b. Symmetrized R_{xx} and anti-symmetrized $|R_{xy}|$ are shown as a function of applied electric field D/ϵ_0. We see essentially no change in the quantized $|R_{xy}|$ and vanishing R_{xx} up to a critical electric field $D_C/\epsilon_0 \approx 150mV/nm$. Above this field, $|R_{xy}|$ drops and R_{xx} rapidly increases. A check of the R_{xx} behavior as D/ϵ_0 is swept up and down reveals no hysteresis, implying a continuous phase transition between a QAH and trivial insulating state.

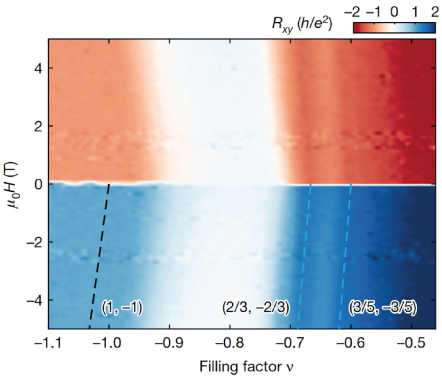

Figure 5.4: Transport Landau fan. R_{xy} Landau fan at $D = 0$. Dispersion of integer and fractional features are consistent with Figure 4.4 (see text). Figure adapted from Ref. [127]. Reproduced with permission from Springer Nature.

Temperature dependence measurements can give us information on the stability of the QAH regime and the electric field driven phase transition. As we can observe in Figure 5.5c, the hysteretic component of R_{xy}, ΔR_{xy}, remains finite up to approximately 10K at $D/\epsilon_0 = 0$, with quantization surviving to 8K. This is quite robust, and near to our Curie temperature for ferromagnetism at $\nu = -1$. The temperature dependence of R_{xx} as a function of temperature and electric field at 100mT is shown in Figure 5.5d. R_{xx} increases with T below $D_C/\epsilon_0 \approx 150mV/nm$, and increases with T above $D_C/\epsilon_0 \approx 150mV/nm$. Arrhenius fitting to the temperature dependence at each value of D/ϵ_0 allows for an estimate of the energy gap as D is increased [16, 30, 48, 128].

The extracted values of the energy gap, Δ, from this analysis are shown in Figure 5.5e. In the QAH region below D_C/ϵ_0, the resistance should be thermally activated. This allows for a fitting of R_{xx} to $R_0 e^{-\Delta/2k_BT}$, with k_B the Boltzmann constant. Above D_C/ϵ_0, the system is in a trivial insulating state, the conductivity is thermally activated, so the fitting is to $R_0 e^{\Delta/2k_BT}$. Between these regimes, R_{xx} is essentially independent of temperature, with a value near h/e^2. This behavior resembles that observed for quantum Hall liquid to Hall insulator[129] and QAH to Anderson insulator[130] phase transitions. From these fittings, we can observe a gradual decrease

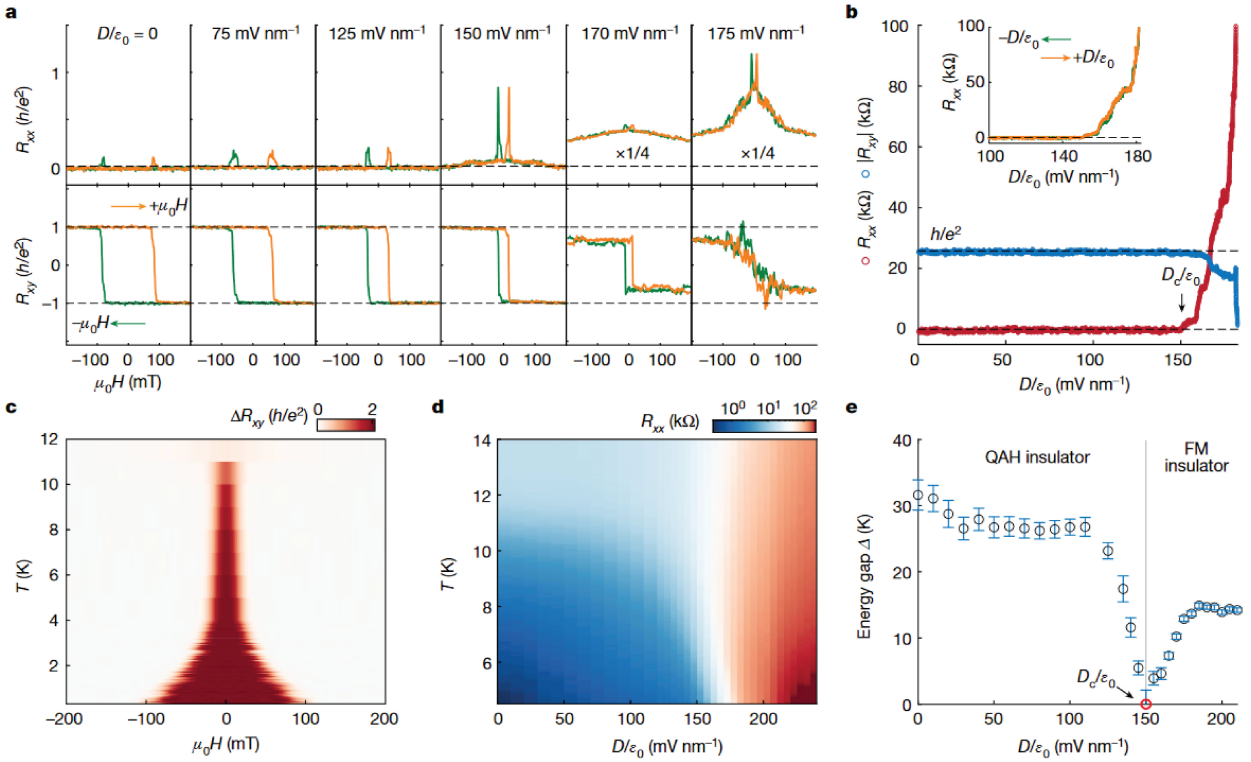

Figure 5.5: Integer quantum anomalous Hall. a, R_{xx} and R_{xy} at $\nu = -1$ as magnetic field is swept down and up for selected values of D/ϵ_0. Data taken at 100mK. Quantized R_{xy} and vanishing R_{xx} at zero magnetic field, as can be observed for $D/\epsilon_0 = 0$, demonstrate the QAH effect. **b,** $|R_{xy}|$ (blue) and R_{xx} (red) as a function of D/ϵ_0. R_{xx} and R_{xy} are symmetrized and anti-symmetrized, respectively, at $\mu_0 H = \pm 200mT$. Inset, R_{xx} versus D/ϵ_0 swept up and down near the phase transition. **c,** ΔR_{xy}, the hysteretic component of R_{xy}, as a function of temperature and magnetic field. ΔR_{xy} remains nearly quantized at $2h/e^2$ up to 8K, demonstrating the robustness of the QAH state. **d,** Intensity plot of R_{xx} versus temperature and electric field. A small magnetic field (100mT) is applied to suppress the magnetic domain fluctuations. The system transitions from a QAH to a trivial insulating phase as D/ϵ_0 is increased above approximately $150mV/nm$. **e,** Energy gap as a function of the electric field extracted from the data in (d). Error bars are obtained from fitting variance. The closing and reopening of the gap versus D/ϵ_0 are evidence for a continuous topological quantum phase transition between the QAH state and the topologically trivial correlated insulating state. Figure adapted from Ref. [127]. Reproduced with permission from Springer Nature.

of Δ as D/ϵ_0 is increased from $0mV/nm$, before a rapid drop near D_C/ϵ_0. As R_{xx} has little temperature dependence in the vicinity of D_C/ϵ_0, the value of Δ cannot be determined precisely in this region. Above D_C/ϵ_0, Δ rises again as the system enters the trivial insulating phase. This behavior strongly supports the picture of a gap closing and reopening as D/ϵ_0, as would be expected for a continuous topological quantum phase transition.

5.3 Fractional Quantum Anomalous Hall Effect in $MoTe_2$

We focus now on the fractional states. Figure 5.6a shows R_{xx} and R_{xy} as $\nu_0 H$ is swept up and down, at $\nu = -2/3$ and $/\epsilon_0 = 0$. As in Figure 5.5a, R_{xy} is quantized at 0T and R_{xx} is vanishing except for small bumps at the flipping field. However, in this case, the quantization of R_{xy} is no longer to $\pm h/e^2$, but rather to $\pm 3h/2e^2$. This confirms the earlier optical measurements - the state at $\nu = -2/3$ is a zero field FCI, with $C = -2/3$. Similarly, the sweeps in Figure 5.6b confirm $\nu = -3/5$ to be zero field FCI with $C = -3/5$.

The zero field FCI states are also electrically tunable, though with a smaller D_C/ϵ_0 than the QAH state. We observe a drop away from the quantized value of R_{xy} and an increase in R_{xx} at a critical field $D_C/\epsilon_0 \approx \pm 50 mV/nm$. R_{xx} increases to approximately $100k\Omega$ near $D_C/\epsilon_0 \approx \pm 100 mV/nm$, before dropping again at large D/ϵ_0. This indicates a phase transition from zero field FCI to to a topologically trivial resistive state, before finally transitioning to a metallic state. The moderate D insulating states can be observed in Figure 5.3a, appearing as triangular features near $\nu = -2/3$. However, the nature of these insulating states are still not clear, and no signatures of these features are observed in optical measurements.

From the temperature dependence of the R_{xx} and R_{xy} vs $\mu_0 H$ sweeps, we can get an idea of the energy scale of the zero field FCI. As we see in Figure 5.6d, R_{xy} remains quantized at zero magnetic field up to 2K - quite robust for a zero field FCI. Finite R_{xy} hysteresis survives up to 3K, as can be seen in Figure 5.6e.

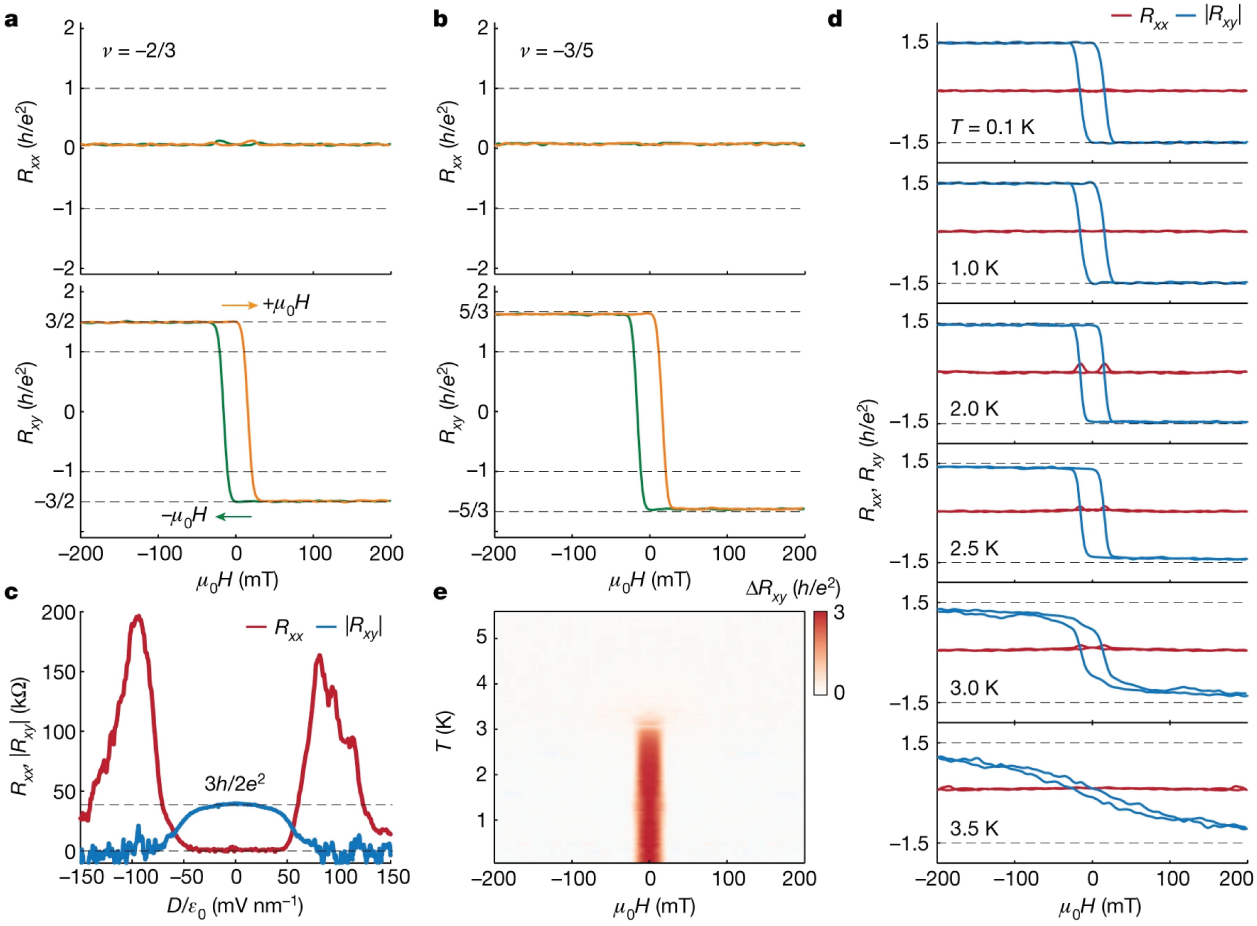

Figure 5.6: Fractional quantum anomalous Hall. a,b, R_{xx} and R_{xy} vs $\mu_0 H$ swept down and up at $D/\epsilon_0 = 0$ for $\nu = -2/3$ and $-3/5$, respectively. **c,** R_{xx} and $|R_{xy}|$ vs D/ϵ_0. Data are taken at $\mu_0 H = \pm 50mT$ and symmetrized and antisymmetrized, respectively. **d,** R_{xx} and R_{xy} sweeps as a function of temperature for $\nu = -2/3$, showing zero field quantization up to 2K. **e,** Hysteretic component of R_{xy} vs temperature, showing a critical temperature for hysteresis of ∼3K. Data in (c-e) are taken at $\nu = -2/3$. Figure adapted from Ref. [127]. Reproduced with permission from Springer Nature.

5.4 *Signs of the Zero Field Composite Fermi Liquid*

Finally, we consider the behavior of the system near half filling of the moiré Chern band. Figures 5.7a&b show R_{xx} and R_{xy} as $\mu_0 H$ is swept up and down, at $\nu = -1/2$ and $D/\epsilon_0 = 0$. R_{xy} shows hysteresis, and has a value of approximately $\pm 2h/e^2$. R_{xx} is small. However, as we can see in Figure 5.7c, there is no plateau in R_{xy} at $\nu = -1/2$. In contrast, there are clear plateaus at the fillings corresponding to the zero field FCI states at $\nu = -2/3$ and $\nu = -3/5$, similar to the behavior of the Jain states in 2DEGS in the FQH regime. We note also a drop in R_{xy} between $\nu = -2/3$ and $\nu = -3/5$, unlike in FQH measurements. This suggests that there may be a competing phase, possibly a ferromagnetic metal, which is favored between these fillings. R_{xy} near $\nu = -1/2$ increases linearly with decreasing ν. This suggests that there is no incompressible state which forms at $\nu = -1/2$. The lack of an incompressible state is consistent with our previous PL measurements, where no gapped feature is seen near $\nu = -1/2$.

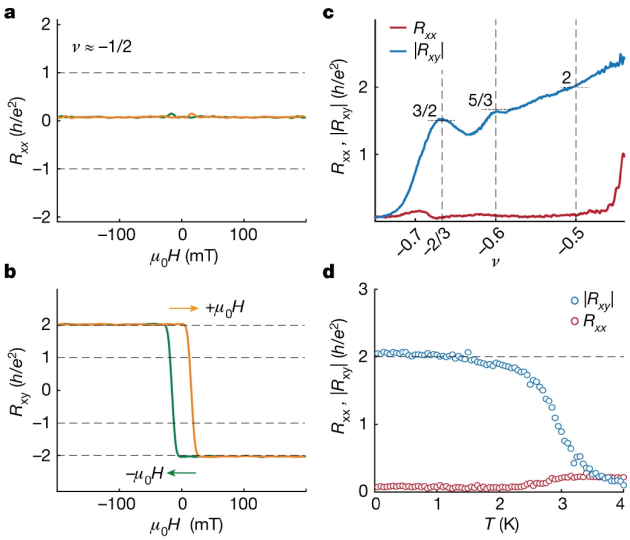

Figure 5.7: Anomalous Hall near $\nu = -1/2$. a, b, R_{xx} and R_{xy} vs $\mu_0 H$ swept down and up at $\nu = -1/2$. **c,** R_{xx} and R_{xy} vs ν. **d,** Temperature dependence of R_{xx} and R_{xy}, near $\nu = -1/2$. R_{xx} and R_{xy} in (c,d) are symmetrized and antisymmetrized at ± 50mT, respectively. All data taken at $D/\epsilon_0 = 0$. Figure adapted from Ref. [127]. Reproduced with permission from Springer Nature.

This behavior, however, bears a clear resemblance to that of the half-filled lowest Landau level, which also shows no plateaus and a continuous change in the Hall resistance. This behavior in the Half filled LLL has been shown to correspond to a compressible composite Fermi liquid (CFL) state [5, 6, 122–126]. Numerical work has predicted that the zero-field lattice analog of the CFL - the anomalous CFL - should appear as the ground state at $\nu = -1/2$ in $tMoTe_2$ [95, 96].

We show the temperature dependence of R_{xx} and R_{xy} at $\nu = -1/2$. As temperature is increased, the value of $|R_{xy}|$ decreases from $2h/e^2$, eventially dropping to zero at 4K. This could indicate a topologically trivial state at higher temperature.

To conclude this chapter, our transport measurements have directly confirmed both QAH and FQAH in moiré $MoTe_2$. These results have since been replicated by a different group [131]. In addition, the behavior of this system around $\nu = -1/2$ suggests that it could host a zero field CFL. Probing the zero field CFL would be quite tricky - measurements of the CFL in the half filled LLL have relied on a variety of complex device architectures.[2] However, some possibilities exist to observe additional experimental signatures. It has been proposed that the moiré potential could result in commensurability oscillations in the resistance near $\nu = -1/2$ [95]. This is similar to the observations of oscillations in a LLL CFL with an externally imposed periodic potential [124, 132]. The question of whether $tMoTe_2$ hosts an anomalous CFL is a major one. The LLL CFL can be understood as the parent state not only of the Jain sequence states, but also more exotic states such as the one observed at $\nu = 5/2$, which is expected to be non-Abelian. Thus, finding evidence of a zero field CFL would be another step towards the ultimate goal of zero field non-Abelian anyons.

[2] See Appendix C

Chapter 6

TRION SENSING OF A ZERO FIELD COMPOSITE FERMI LIQUID

In the last chapters, we used optics and transport to establish the existence of zero-field fractional Chern insulators in moiré $MoTe_2$. The filling factors at which these FCIs are observed - $\nu = -2/3$, $\nu = -3/5$, and $\nu = -4/7$ - correspond to the lowest three Jain sequence states. In addition, the measured Hall resistance R_{xy} shows no plateau as ν is tuned through -1/2. Rather, $|R_{xy}|$ increases linearly, passing through $2h/e^2$ at $\nu = -1/2$. As is discussed in Appendix C, an elegant way to understand the Jain sequence FQH states in partially filled Landau levels is via the composite fermion picture. Here, electrons can be thought of as forming a bound state with two flux quanta of the applied magnetic field, producing a new quasiparticle - the "composite fermion" [5]. At exactly half filling, the electrons will "eat up" all of the applied magnetic field to form the composite fermions. The composite fermions at $\nu = 1/2$ feel an *effective* magnetic field $B^* = 0T$, and form a Fermi liquid [6]. The fractional quantum Hall states can then be thought of as the *integer* quantum Hall states of this composite Fermi liquid. The question then becomes: "how real are composite fermions"? This required some experimental ingenuity to answer. A variety of measurements, using surface acoustic waves [123], magnetic focusing effects [125, 133], and antidot lattice geometric resonances [124] showed that composite fermions at $\nu = 1/2$ really do act like fermions in a vanishing magnetic field. These results established the existence of a CFL in the half-filled lowest Landau level.

Does this understanding translate to the zero field FCIs in our flat moiré Chern band? Do we have an *anomalous* composite Fermi liquid at $\nu = -1/2$? Two recent theory works have predicted this to be the case [95, 96]. Beyond clarifying the behavior of our system, stronger experimental evidence of a zero-field CFL could help to point the way towards additional FCI states hosting non-Abelian anyon excitations. As in the LLL measurements of the CFL, however, the gapless nature of the CFL means alternate experimental routes must be explored. In this chapter, we take advantage of the unique optical properties of the $MoTe_2$ bilayer - not only its strong optical response but also

its selection rules for trion emission - to gather additional evidence for the anomalous composite Fermi liquid.

6.1 Trion Photoluminescence: Spontaneous Circular Polarization

So far, we have taken advantage of the optical properties of $MoTe_2$ bilayer to observe both ferromagnetic order and topologically nontrivial insulating states in our moiré system. The K-valley physics and optical selection rules enable RMCD to serve as a probe of spin/valley polarization, and trion emission intensity is sensitive to the formation of insulating states. However, we haven't looked at the polarization dependence of the photoluminescence emission. While reflectance is sensitive to absorption - and has polarization dependence, which is what allows us to measure RMCD - photoluminescence is dependent on the recombination process of the exciton. As this recombination process depends on the available free charges which can form trion bound states, PL could give us information about what is going on with our doped charges in the moiré band at different fillings.

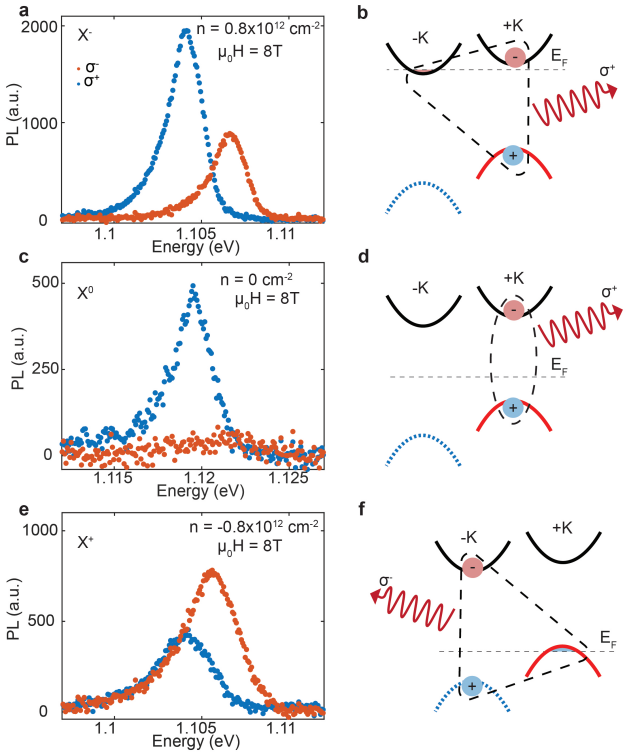

Figure 6.1: Zeeman splitting and selection rules. a, Polarization resolved X^- PL at 8T. Doped electrons preferentially sit in the -K valley and bind to the +K valley exciton, emitting in the σ^+ channel - shown schematically in **b**. **c&d,** As in (a&b), but for zero doping - emission is from X^0. Emission is dominated by the redshifted +K valley exciton emitting in the σ^+ channel. **e&f,** As in (a-d), but for small hole doping, with emission from X^+. Doped holes preferentially sit in the +K valley, binding with the blueshifted -K valley exciton and emitting in the σ^- channel. Electron and hole doping values are small, and the system is not in the ferromagnetic region.

We first discuss the selection rules of the PL emission. Recall that the bilayer system retains the K-valley direct band gap of the monolayer, and displays the strong PL emission and selection rules that this entails. The main difference between the bilayer PL for small doping (Figure 6.1) and the monolayer is a redshift of approximately 30meV. We start with the relatively straight-

forward case of small electron or hole doping, leading to negative and positive trions X^- and X^+, as well as the neutral exciton X^0 at zero doping. The doping is small enough that the system is far from the ferromagnetic region on the hole side, which appears at roughly $-2 \times 10^{12} cm^{-2}$ in this device. In Figure 6.1a, the σ^+ and σ^- emission of the negatively charged trion X^- have different emission intensities and energies under a large applied magnetic field of 8T. This can be understood by a Zeeman shift of both the valence and conduction band edges for the different valleys, as shown schematically in Figure 6.1b. When the system is slightly electron doped, the electrons will preferentially sit in the -K conduction band. The available carriers will make the trion the lowest-energy emission channel, but because of Pauli exclusion the trion must be a singlet - i.e., the two holes must have opposite spin, and therefore opposite valley. Since more -K electrons are available, there is more emission from the exciton in the +K valley. Because of the valley selection rules, the +K valley exciton emits in the σ^+ channel. The energy difference between the peaks is due to the different Zeeman shifts of the two valleys.

For the neutral exciton, the picture is a bit simpler. The Fermi level is in the gap, so there is no trion formation, but there is still a Zeeman shift of the valleys. As we can see from Figure 6.1c&d, X^0 emission is almost entirely from the σ^+ channel at lower energy. This is because, after Zeeman shifting, the exciton in the +K valley is the most energetically favorable state, and therefore dominates the PL emission. The positive trion X^+ acts quite similarly to X^-, but now there is more emission in the σ^- channel (Figure 6.1e&f). This is because more doped holes sit in the +K valley valence band and bind to the -K valley exciton, meaning that the σ^- emission is stronger.

Having established the valley dependent optical selection rules for trion emission, we now consider the behavior of the system in the ferromagnetic regime. In the FM metal phase, the doped carriers are spin-valley polarized. For the FM state initialized with positive magnetic field, the spins point up, and are in the +K valley. As the trion PL emission helicity depends on the valley of the doped carriers, it is reasonable to expect that the degree of circular polarization (DOCP) of the trion PL is sensitive to the doped holes in our system, and can serve as a probe of their behavior - shown schematically in Figure 6.2a. Experimentally, we observe that when the system is tuned to the FM metal regime at $\nu = -0.78$, initialized with $\mu_0 H > 0T$, and measured at $\mu_0 H = 0T$, the emission is essentially completely circularly polarized, emitting in the σ^- channel (Figure 6.2b). The same

measurement, but with initialization $\mu_0 H < 0T$ and measured at $\mu_0 H = 0T$, also shows nearly complete circular polarization, but emits in the σ^+ channel (Figure 6.2c). Worth noting is that this spontaneous near-unity circularly polarized emission is unprecedented not only in TMDs, but in magnetic semiconductor systems generally. The coupling between the spin, valley, and optical degrees of freedom in this system could be extremely valuable for technological applications.

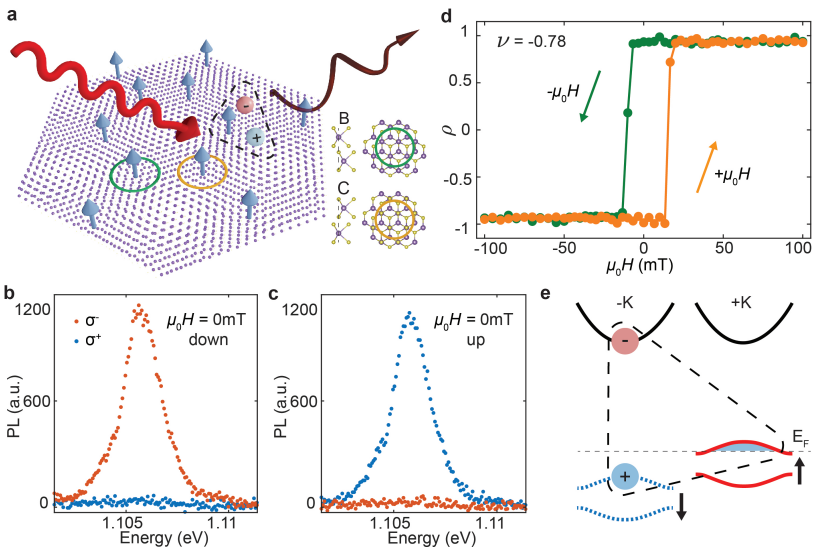

Figure 6.2: Spontaneous circular polarization of trion PL. a, Schematic of moiré superlattice in the ferromagnetic metal phase and trion PL measurement. B (MX) and C (XM) local high symmetry sites are denoted in the inset. **b,** Circular polarization resolved trion PL at $\nu = -0.78$, in the FM metal phase. Magnetization is initialized to point up by sweeping $\mu_0 H$ from a positive value to zero. **b,** As in (b), but with magnetization initialized to point down.**d,** Degree of circular polarization ρ as $\mu_0 H$ is swept down and up, showing the spontaneous circular polarization arises from the ferromagnetism. **e,** Schematic of trion sensing of a spin-valley polarized Fermi liquid.

We can extract a value for the PL DOCP by integrating over the PL peak in each channel, giving us $PL(\sigma^-)$ and $PL(\sigma^+)$, and taking the normalized difference, which we define as $\rho = \frac{PL(\sigma^-) - PL(\sigma^+)}{PL(\sigma^-) + PL(\sigma^+)}$. Measuring ρ as a function of $\mu_0 H$ swept down and up, sharp transitions between $\rho \approx +1$ and $\rho \approx -1$ can be observed, with clear hysteresis (Figure 6.2d). This behavior demonstrates that the trion PL helicity is a result of the ferromagnetic order. A schematic of the process leading to this near unity DOCP is shown in Figure 6.2e. The ferromagnetic order and spin/valley locking result in a spontaneous polarization of the doped carriers into the +K valley, for ferromagnetism pointing up. In the FM metal phase at $\nu = -0.78$, these doped holes form a spin-valley polarized Fermi liquid. As discussed, the favored emission channel is the X^+ trion. However, as the trion must be a singlet, and the only available carriers are in the +K valley, the exciton must sit in the -K valley. Therefore, emission is in the σ^- channel. The time-reversed partner of this - doped carriers in the -K valley and the exciton in the +K valley emitting in the σ^+ channel - occurs when the

magnetization is flipped to point down. Thus, the trion PL emission helicity serves as a probe of the spin-valley polarized Fermi liquid in our moiré Chern band.

6.2 Helicity Suppression in the Chern Insulating States

So far, we have discussed the FM metal region of phase space, establishing that the spin-valley polarized Fermi liquid leads to a spontaneous near-unity polarization in the trion PL emission. However, as has been covered extensively in the last few chapters, additional states arise in other regions of the ferromagnetic phase space - namely, the integer and fractional Chern insulators. We know that the trion PL emission intensity drops as we tune to the insulating states, but have not investigated the polarization dependence of the emission. As the polarization dependence depends on the same spin-valley polarized holes that are involved in the formation of the insulating states, it would be interesting to see how ρ is affected as ν is varied.

In Figures 6.3a&b, we show polarization-resolved PL emission spectra as a function of ν. While the general shape of the PL is consistent with the unpolarized measurement shown in Figure 4.1b - drops in emission and blueshifts are visible for the insulating states - the polarization dependence gives additional information. While the FM metal region around $\nu = -0.8$ shows emission only in the σ^- channel, as we expect from the previous discussion, emission is visible in the σ^+ channel around the insulating states at $\nu = -1$ and $\nu = -2/3$. In addition, we can observe σ^+ emission in a region of filling around $\nu = -1/2$. The extracted ρ as a function of ν, plotted in Figure 6.3c, clarifies these features. We observe that within the FM region of phase space, which is roughly between $\nu = -1.2$ and $\nu = -0.3$, ρ is generically near 1. The exceptions to this are a broad drop around the Chern insulator at $\nu = -1$, a narrower drop around the fractional Chern insulator at $\nu = -2/3$, and a suppression of ρ around $\nu = -1/2$. Polarization-resolved PL spectra at $\nu = -1$ and $\nu = -2/3$ are plotted in Figures 6.3d&e, which show suppressed trion emission and drop in ρ.

The drop in ρ at these insulating states is quite counterintuitive. Not only are these states ferromagnetic, but they actually have more robust ferromagnetism than the surrounding fillings, as can be seen in the measurements of Curie temperature and coercive field vs ν in Figures 3.4 and 4.2. If the PL emission helicity relies on the spin-valley polarization of doped holes in the FM phase, why would we see these drops in ρ where FM is the strongest?

This puzzle can be resolved by considering the gapped nature of the insulating states and the

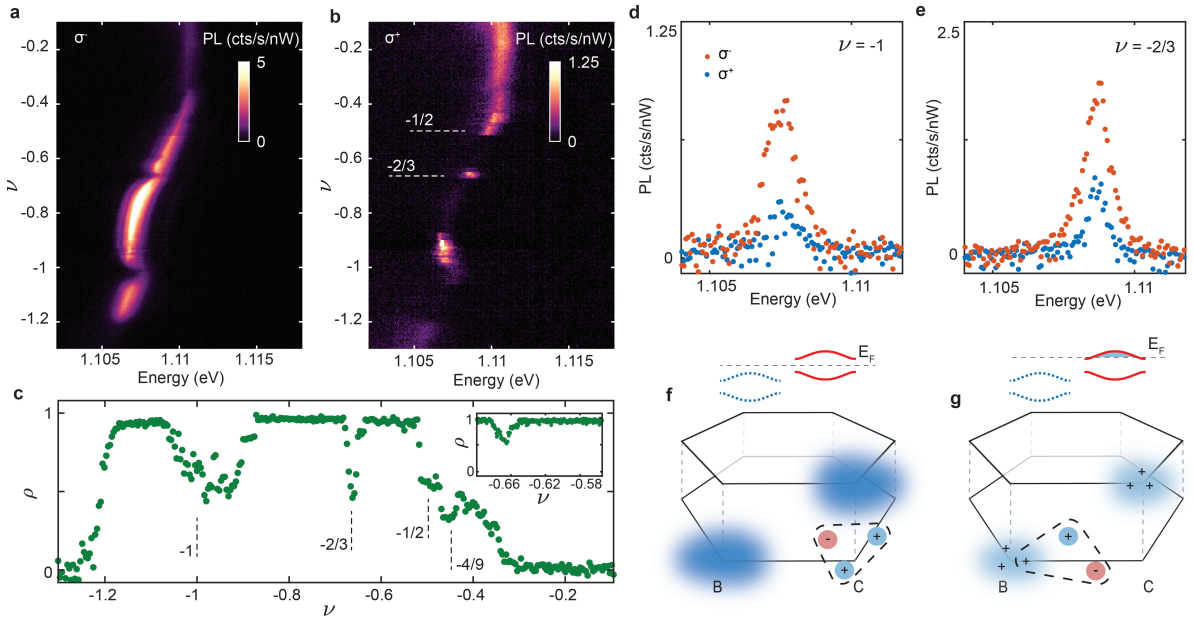

Figure 6.3: Suppression of ρ at Chern insulating states. **a,** Trion PL intensity plot as a function of ν and emission energy, detecting the σ^- channel. **b,** As in (a), but for the σ^+ channel. **c,** ρ, extracted from (a&b), vs ν. Drops are visible in ρ around $\nu = -1$, $-2/3$, and $-1/2$, as well as an additional dip consistent with the $\nu = -4/9$ Jain state. Inset: high resolution ρ sweep near fractional filling. **d&e** Circular polarization resolved PL at integer ($\nu = -1$) and fractional ($\nu = -2/3$) Chern insulator states. **f,** Schematic of hole distribution at $\nu = -1$. Inset denotes the gapped Fermi surface, with the first moiré flat band completely filled, thus consuming the spin-valley polarized Fermi liquid. Due to the large Coulomb repulsion, trions avoid spatial overlap with the spin-valley polarized holes. **g,** Schematic of hole distribution in the underdoped Chern insulator (i.e., the ferromagnetic metal phase). The spin-valley polarized Fermi liquid provides carriers to form valley polarized trions.

effect of strong correlations. If we consider $\nu = -1$, the first moiré band is completely filled, and the Fermi surface is gapped out. As we recall from Chapter 3, the doped holes filling this band are mainly localized to the MX (B) and XM (C) high symmetry sites in the bottom and top layers, shown schematically in Figure 6.3f. Because of the formation of this gapped phase, there are no longer free spin-valley polarized free carriers available to form trions. There is still some trion emission (albeit with decreased intensity) in this gapped phase, which is likely a result of thermally excited holes binding to the photoexcited electron-hole pairs. Because of Coulomb repulsion and Pauli exclusion, these thermally populated holes will avoid spatial overlap with the filled orbitals on the MX and XM sites. Thus, the trion will only weakly interact with the background ferromagnetism

at $\nu = -1$, causing ρ to drop. Similar behavior occurs for the gapped phase at $\nu = -2/3$.

There is a much broader range of suppressed ρ around $\nu = -1$ than there is around $\nu = -2/3$. This is not too surprising, as it is also consistent with the broader plateau around $\nu = -1$ seen in transport measurements (Chapter 5) vs the plateau at $\nu = -2/3$. This plateau in transport is a result of random potential disorder and the percolation transition, as has been widely studied in 2DEGs [92, 134]. This percolation transition can also explain the behavior of ρ, as the $\sim 1\mu m$ scale of the beamspot will also likely contain a randomly varying potential background. In the intermediate regime as the system is doped away from $\nu = -1$, there will be regions of both QAH insulating states and puddles of free carriers. This causes an increase in ρ, but some signal remains in the σ^+ channel. As the we dope far enough away from $\nu = -1$, into the FM metal phase, ρ returns to near unity - the spin-valley polarized carriers are now available to form trions, as discussed previously (Figure 6.3g)

6.3 Ferromagnetism vs Trion Helicity in the TRS Breaking Phase Space

The picture we have discussed so far - near-unity circular polarization in the gapless spin-valley polarized metal, with drops at the gapped insulating states - explains most of the behavior seen in the polarization-resolved PL. However, there is one feature that is not explained - the drop in ρ near $\nu = -1/2$. To understand this, we investigate the full ferromagnetic phase space vs D/ϵ_0 and ν - shown by the finite RMCD region in Figure 6.4a. Clearly, the system remains ferromagnetic at and below $\nu = -1/2$. We can compare the RMCD measurement with a measurement of ρ as a function of D/ϵ_0 and ν (Figure 6.4b). The general boundary of these measurements are the same - both show the "fishtail" like outline of the FM phase space, dropping to zero outside. However, unlike in the RMCD measurement, ρ shows a much more complex structure within the FM region. The "generic" behavior within the FM region appears to be near-unity ρ. This is the case in the FM metal region between $\nu = -1$ and $\nu = -2/3$, discussed previously, as well as in the FM tails above $\nu = -1$ and near the FM boundaries at finite D. This is consistent with our trion recombination picture - in the FM region, generically, there are free spin-valley polarized carriers which form trions emitting in a single channel.

Three regions of phase space diverge from this behavior. Two of these we have already discussed - the integer and fractional Chern insulating states at $\nu = -1$ and $\nu = -2/3$, and the surrounding percolation transition region. We note that as D is increased to near the critical value D_C for $\nu = -1$ and $\nu = -2/3$, there is an increase in ρ, before a subsequent drop as D is increased further and the ferromagnetism is destroyed. Because the decreased ρ at these fillings corresponds to the gapped state and lack of free spin-valley polarized carriers, the reemergence of large ρ at increased D suggests that these topological insulating states are destroyed at large D near D_C, but below the value of D where ferromagnetism disappears.

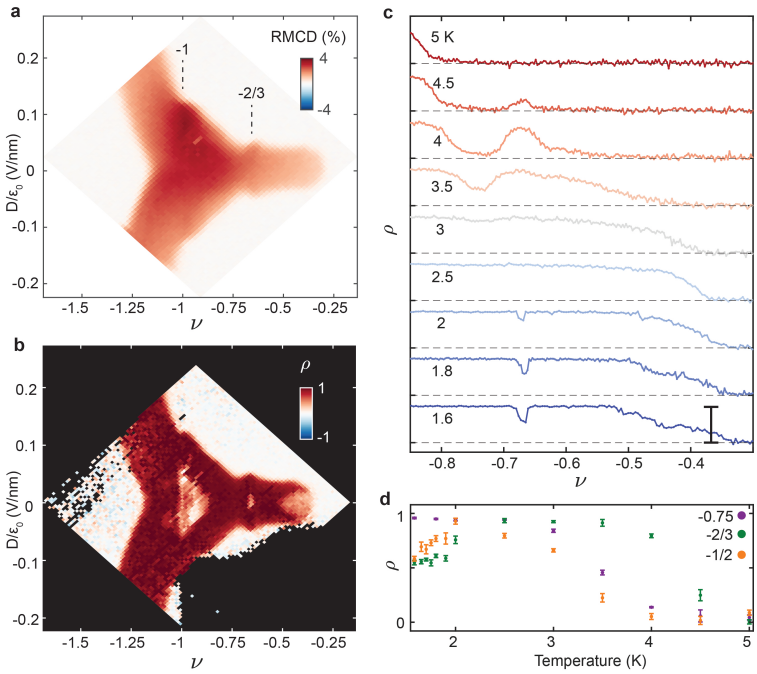

Figure 6.4: Ferromagnetism and ρ phase space comparison and temperature dependence. a, RMCD vs D/ϵ_0 and ν. **b,** ρ vs D/ϵ_0 and ν. Suppression of ρ is visible in the regions of FM phase space around $\nu = -1$, $\nu = -2/3$, and $\nu = -1/2$ for small D. **c,** ρ vs ν as a function of temperature, at 5nW and 0T. At the base temperature of 1.6K, suppression of ρ is visible at $\nu = -2/3$ and $\nu = -1/2$. As temperature increases, this suppression disappears. With increasing temperature, ρ eventually drops to zero, surviving to higher temperature at $\nu = -2/3$ where the Curie temperature is enhanced. Scale bar indicates from $\rho = 0$ to $\rho = 1$, with data offset for clarity. **d,** Extracted ρ for selected fillings as a function of temperature. ρ is suppressed at base temperature for $\nu = -2/3$ and $\nu = -1/2$, and increases as temperature is increased until $\sim 2K$, before dropping as temperature is increased further and ferromagnetism is destroyed. In the FM metal phase at $\nu = -0.75$, however, ρ starts at near unity for base temperature, and decreases monotonically as temperature increases. Error bars are one standard deviation of ρ extracted from multiple polarization resolved PL spectra taken at each temperature.

The third of these regions of phase space - the one around $\nu = -1/2$ - cannot be explained by our picture so far. We know from both transport and optics that there is no gapped state in the vicinity of $\nu = -1/2$. In transport, this is indicated by a lack of a plateau in R_{xy}, and in optics we see no change in the trion PL energy or intensity. From RMCD, we know that the region is ferromagnetic. Nevertheless, we see a drop in ρ similar to the insulating states, and in contrast the

the FM metal regions. An additional puzzling feature is that while ρ is suppressed near $D = 0$ in the region near $\nu = -1/2$, it *increases* at elevated D. If this region were a gapless, spin-valley polarized Fermi liquid, this behavior would make no sense - the valley polarized free carriers in the FM region lead to large ρ, and ferromagnetism is weakened at larger D. Thus, the value of ρ should decrease as D increases for an FM metal. Indeed, this is what we observe in the FM metal region near $\nu = -0.75$. Though the region near $\nu = -1/2$ is gapless, its behavior of ρ vs D is much more similar to the integer and fractional Chern insulating states than it is to the spin-valley polarized Fermi liquid.

Our picture is supported by a measurement of the temperature dependence of ρ vs ν, shown in Figures 6.4c&d. As the reduction of the trion polarization corresponds to the formation of a many-body gap, we expect that for both the Chern insulator and CFL states, ρ should increase as the temperature increases within a certain temperature range (i.e., below the Curie temperature). Indeed, the data show that the circular polarization of the -2/3 FCI and -1/2 state first increase as temperature rises, then peak to near unity, and subsequently drop again as magnetic order starts to vanish. This is in stark contrast to the temperature dependence of the PL polarization in the ferromagnetic metal phase. The polarization remains near unity at low temperature, before dropping at a temperature close to the Curie temperature. It is worth noting that the temperature at which trion PL polarization suppression at -2/3 vanishes is around 2K, which coincides with the temperature at which R_{xy} starts to lose quantization (see Figure 5.6d). This consistency further supports our interpretation of the suppression of trion circular polarization as resulting from the formation of a many-body gap

6.4 Optical Signatures of the Zero Field Composite Fermi Liquid

The optical behavior of the system near $\nu = -1/2$ presents a conundrum. It is ferromagnetic - thus spin/valley polarized - and has no gapped states. However, the decreased value of ρ at this filling implies that near $D = 0$, free spin-valley polarized doped holes are not available to bind to the exciton, and the trions likely form at locations away from the filled moiré orbitals on the MX/XM regions. In addition, as D is increased, the increase in ρ implies more spin-valley polarized carriers become available - even though this finite D weakens the ferromagnetism. This behavior is in stark contrast to the spin-valley polarized Fermi liquid near $\nu = -0.75$.

The formation of the theoretically predicted zero field composite Fermi liquid near $\nu = -1/2$, however, can explain these observations. The zero field CFL has a gapless composite fermion Fermi surface [6], which explains the lack of any observation of a gapped phase in transport or optics. The quasiparticles in this phase, though, are composite fermions, rather than the spin-valley polarized holes of the ferromagnetic metal. Thus, there is a pseudogap suppressing local spin-valley polarized charge excitations when the system is in the zero field CFL phase. This pseudogap property has been observed by tunneling measurements between double layer quantum wells, which show a suppression of electron tunneling at low energies when tuned into the CFL regime in the partially filled LLL [135, 136]. A pseudogap is also expected to occur for the zero field CFL in the partially filled moiré Chern band [96].

The pseudogap can clarify the unusual behavior of ρ near $\nu = -1/2$. In the dipole picture, composite fermion formation can be thought of as an electron binding to a 2-fold vortex to form a dipole [137]. Local charge excitations require a finite energy to break apart this dipole - thus the pseudogap. Because trion formation requires a free charge to bind to the exciton, this pseudogap prevents the type of recombination process we have discussed for the spin-valley polarized Fermi liquid (Figure 6.5a). Rather, the zero field CFL behaves in a similar manner to the Chern insulator phases - consuming the spin-valley polarized Fermi liquid needed for the formation of spin-valley polarized trions.

This picture can also explain the behavior of ρ as D is increased. The zero field CFL - like the integer and fractional Chern insulators - is weakened for increasing D. We show linecuts of ρ vs D in Figures 6.5b,d,f,&h. The Chern insulators in Figures 6.5d&h have a minimum near $D = 0$ where the insulating state is robust, with an increased ρ near boundaries of the FM phase, as discussed. The behavior at $\nu = -1/2$ is extremely similar - consistent with a phase at low D suppressing spin-valley polarized trion formation which is weakened with increasing D in favor of a spin-valley polarized Fermi liquid, before ferromagnetism is destroyed entirely at large D. This behavior contrasts with that of the ferromagnetic metal at $\nu = -0.8$ (Figure 6.5f). Here, there is a near-unity plateau in ρ for small D, with an eventual drop to zero at large D where ferromagnetism disappears.

As a comparison to the behavior of ρ vs D at these fillings, we also measure RMCD at 0T vs D, but with 5nW of 623.8nm laser (as is used to measure ρ) focused on the same spot (Figs. c,e,g,&i).

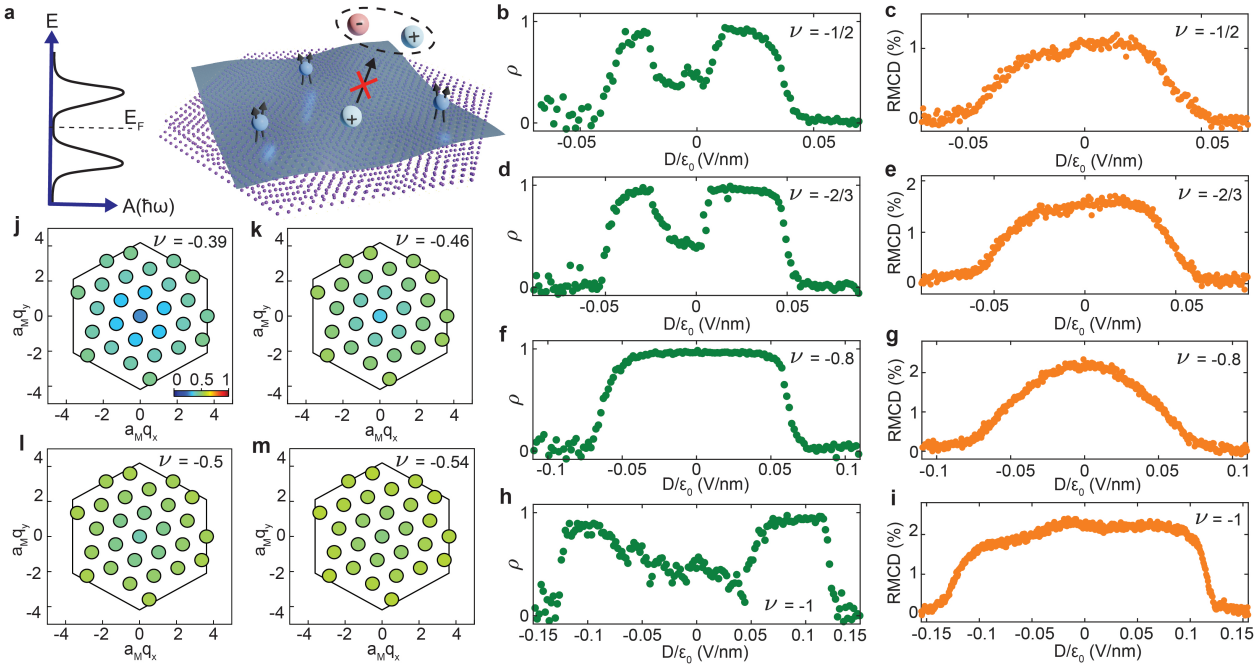

Figure 6.5: Signatures of the zero field CFL. a, Cartoon illustrating the charge pseudogap property of the CFL phase. This pseudogap suppresses local spin-valley polarized charge excitations in the CFL, thus reducing trion valley polarization. **b&c,** PL polarization ρ (b) and RMCD (c) vs displacement field at $\nu = -1/2$. PL is taken with 5nW excitation at 633nm, and RMCD is taken with excitation near the trion resonance, with 5nW at 633nm focused on the same spot as RMCD is measured. While there is a clear drop at small D for ρ, no drop is seen in RMCD. **d&e,** As in (b&c), but at $\nu = -2/3$. **f&g,**, As the previous plots, but in the FM metal region at $\nu = -0.8$. No drop is visible in either ρ or RMCD. **h&i,**, As the previous plots, but at $\nu = -1$. **j-m,** Calculated momentum distribution function n(k) of the electron Bloch states for fillings near v=-1/2, averaged over the ground state manifold. n(k) is determined for selected momenta in the moiré Brillouin zone via exact diagonalization. $a_M q_x$ and $a_M q_y$ are x and y components of momentum spanning the moiré Brillouin zone. The nearly uniform and smoothly varying occupation indicates a robust CFL phase over a wide filling range centered at -1/2 filling of the flat Chern band.

In contrast to ρ, RMCD shows a plateau in the FM region at small D for all values of ν.

Our understanding of the suppression of ρ near $\nu = -1/2$ can help to clarify some features of the transport measurements, as well. Comparing ρ vs ν to the transport measurement of R_{xy} vs ν (Figure 5.7c) we see exactly the opposite behavior as filling is decreased. ρ starts near 1 in the FM metal phase, drops at $\nu = -2/3$, increases again, and then drops in the region surrounding $\nu = -1/2$. R_{xy}, however, starts low in the FM metal, increases at $\nu = -2/3$, drops, and then increases linearly through the region surrounding $\nu = -1/2$. From our discussion of large ρ indicating free spin-valley polarized holes, this behavior suggests that the slightly underdoped -2/3 FCI is a spin-valley polarized Fermi liquid.

The phase space surrounding $\nu = -1/2$ with decreased ρ corresponding to a zero field CFL is also supported by numerical calculations of the electron Bloch state momentum distribution function $n(k)$. Figures 6.5j-m show that $n(k)$ is almost completely uniform for a range of fillings centered around $\nu = -1/2$, demonstrating their non-Fermi liquid character. If the system was a Fermi liquid, a sharp transition in momentum space between $n(k) \approx 0$ and $n(k) \approx 1$ would be expected - i.e., we should see an electron Fermi surface.

Over this chapter, we showed that the unique optical properties of the $MoTe_2$ bilayer provide us with a powerful new probe of the physics occurring in the moiré system - the degree of circular polarization of the trion emission, ρ. In particular, the sensitivity of the trion recombination and emission helicity to the availability of free spin-valley polarized carriers gives information on the behavior of the partially filled moiré Chern band not accessible for previous optical or transport measurements. The unusual behavior of ρ in the region around $\nu = -1/2$ can be explained by the formation of the theoretically predicted zero field composite Fermi liquid, offering additional experimental support for this phase beyond the transport results discussed earlier. Further theoretical work is necessary to determine the microscopic picture of trion formation and recombination in the presence of zero field fractional charge - behavior unique to the zero field FCI found in moiré $MoTe_2$. The strong coupling between circularly polarized light, magnetism, and topology in this system suggests that in addition to its usefulness as a probe, the helicity of light may also provide a new tuning knob for the control of topology in the system. If circularly polarized light could be used to control magnetic domains, and thus the topological index of FCIs, it could be an invaluable tool in designing anyon interferometers - and perhaps, one day, topologically protected qubits.

Chapter 7

OUTLOOK

To conclude this dissertation by saying that the discovery of the fractional quantum anomalous Hall effect has had an impact on the condensed matter physics community would be a fairly egregious understatement. Over the past year, the experimental results discussed in the previous chapters established moiré $MoTe_2$ as the first system to host the FQAHE. In the same year, another moiré system - pentalayer graphene/hBN moiré - also showed FQAH [17]. These results, after over a decade of searching, have generated tremendous excitement. FQAH in both systems is very much an active area of research - new theory work is released weekly (often daily!) on the arXiv, and an increasing number of experimental groups have started studying these systems. Pablo Jarillo-Herrero - in whose lab at MIT superconductivity in moiré graphene was first discovered - said recently, "I don't know anyone who's not excited about this. I think the question is whether you're so excited that you switch all your research and start working on it, or if you're just very excited" [138].

While there could be many reasons for this excitement, there are, I think, two primary ones. The first is that the fundamental physics of these fractional quantum Hall phases is extremely interesting. The theory of the fractional quantum Hall effect incorporates concepts such as topological order, composite fermions, and Abelian and non-Abelian anyons. The stringent temperature and magnetic field requirements to realize these phases in fractionally filled Landau levels has made their experimental study quite difficult. Though the $\nu = 1/3$ fractional quantum Hall state was discovered in the early 1980s, for instance, the fractional statistics of its anyon excitations were only observed directly a few years ago [139, 140]. Having a robust, zero field system in which to investigate these concepts is a huge step forward experimentally.

Beyond the experimental convenience of zero field FCIs, however, is the fact that there is almost certainly new physics to explore in these systems. Zero field fractional Chern insulators are not the same thing as fractional quantum Hall phases in Landau levels. For one, zero field FCIs open

up experiments not possible with Landau level systems. Forming a domain wall between two FCIs with opposite topological indices could be as simple as creating two magnetic domains with opposite polarization. Measuring a 2DEG with one section in a +10T magnetic field and another in a -10T field would not be nearly as easy. More device architectures are also possible with FCIs. For instance, hybridizing a fractional state and a superconductor with the goal of engineering non-Abelian anyons is feasible with zero field FCIs, but not at the high magnetic fields required for FQH, as this would destroy the superconductivity. Zero field FCIs might simply have fundamental differences from the FQH states in Landau levels, as well. Though the fractional fillings seen so far in moiré systems correspond to the Jain sequence fillings in the LLL, there may be other fractional states in partially filled moiré Chern bands on a lattice which are not seen in Landau levels. A theoretical understanding of both the $MoTe_2$ and the pentalayer graphene/hBN moiré systems is still being actively worked out, which would shed more light on the types of fractional states which might be expected to occur.

The second reason for the excitement about the discovery of the FQAHE are the potential applications - particularly for topologically protected quantum computation.[1] The main difficulty with building a large-scale quantum computer is decoherence - random interactions between the qubits and environment which destroy the quantum superposition used for the computation. While there are methods to address these decoherence-induced errors using a range of quantum error correction schemes, achieving a scalable, fault-tolerant quantum computer using current qubit architectures remains a major challenge. One path forward, suggested by Kitaev in 2002, is to use anyons to perform quantum computations [8]. This scheme, which requires non-Abelian anyons, encodes our quantum information in the ground state of the system. The way to perform unitary operations on this information - in fact, the *only* way to perform unitary operations on this information - is to braid the anyons around each other. This scheme is insensitive to local perturbations such as a photon or phonon striking the system, as this doesn't cause braiding of the anyons. Topological quantum computation is inherently fault-tolerant.

The challenge with this approach, of course, is realizing and manipulating non-Abelian anyons. Most FQH states in Landau levels host Abelian anyons, but some, such as those at 5/2 or 12/5,

[1] Discussed in more detail in Appendix E

are expected to host non-Abelian ones [141, 142]. Actually detecting and manipulating these non-Abelian anyons is extremely difficult, though, considering the delicate nature of the states and their stringent requirements on sample quality, temperature, and magnetic field. The hope is that these new zero field FCI systems will prove more tractable. Their robust nature and lack of magnetic field requirement is certainly helpful in lightening the experimental requirements, but also in allowing for more flexibility in device design. While these moiré systems are very promising, the zero field FCIs so far observed are all expected to host Abelian anyons. However, hybridizing these FCIs with other materials as discussed above, or building more complex moiré vdW heterostructures, could stabilize new phases not possible in Landau level systems - with the target being those hosting non-Abelian anyons.

I will end by indulging in some speculation. The amount of progress made on our understanding of the moiré $MoTe_2$ system over the past year or so - its phase space, optoelectronic properties, and topological states - is immense. There is, however, much that remains to be explored. Of the dozen optical and transport cryostats in our lab, almost all of them are currently dedicated to measuring moiré $MoTe_2$. But research is not only ongoing in our lab - many groups are now measuring transport and optics on the system, as well as employing specialized techniques such as scanning SQUID magnetometry, MIM, scanning SET, STM, THz optics, ARPES, millikelvin optics, and more. I may be a bit biased, since I have spent much of the past year measuring moiré $MoTe_2$ optics, but the optical properties of the system - in particular, the helicity dependence - seems to me a particularly promising direction. If it were possible to use circularly polarized light to flip magnetic domains - and thereby write patterns of FCIs in-situ onto a device - it would be a huge help in designing studies of zero field anyons. If we add to this our recent results showing that electrical current can control magnetic domains, and thereby the emission helicity, it suggests that combining magneto-optics and transport in a single measurement would be extremely fruitful. But the beauty of the community's excitement about these systems is that there is now a wide range of different techniques and perspectives being applied to their investigation. If there is something even more exciting in moiré $MoTe_2$, it will certainly be found - and, most likely, very soon.

BIBLIOGRAPHY

1. Klitzing, K. v., Dorda, G. & Pepper, M. New Method for High-Accuracy Determination of the Fine-Structure Constant Based on Quantized Hall Resistance. *Physical Review Letters* **45,** 494–497 (1980).

2. Tsui, D. C., Stormer, H. L. & Gossard, A. C. Two-Dimensional Magnetotransport in the Extreme Quantum Limit. *Physical Review Letters* **48,** 1559–1562 (1982).

3. Thouless, D. J., Kohmoto, M., Nightingale, M. P. & den Nijs, M. Quantized Hall Conductance in a Two-Dimensional Periodic Potential. *Physical Review Letters* **49,** 405–408 (1982).

4. Laughlin, R. B. Anomalous Quantum Hall Effect: An Incompressible Quantum Fluid with Fractionally Charged Excitations. *Physical Review Letters* **50,** 1395–1398 (1983).

5. Jain, J. K. Composite-fermion approach for the fractional quantum Hall effect. *Physical Review Letters* **63,** 199–202 (1989).

6. Halperin, B. I., Lee, P. A. & Read, N. Theory of the half-filled Landau level. *Physical Review B* **47,** 7312–7343 (1993).

7. Wen, X.-G. Colloquium: Zoo of quantum-topological phases of matter. *Reviews of Modern Physics* **89,** 041004 (2017).

8. Kitaev, A. Y. Fault-tolerant quantum computation by anyons. *Annals of Physics* **303,** 2–30 (2003).

9. Haldane, F. D. M. Model for a Quantum Hall Effect without Landau Levels: Condensed-Matter Realization of the "Parity Anomaly". *Physical Review Letters* **61,** 2015–2018 (1988).

10. Tang, E., Mei, J.-W. & Wen, X.-G. High-Temperature Fractional Quantum Hall States. *Physical Review Letters* **106,** 236802 (2011).

11. Sun, K., Gu, Z., Katsura, H. & Das Sarma, S. Nearly Flatbands with Nontrivial Topology. *Physical Review Letters* **106,** 236803 (2011).

12. Neupert, T., Santos, L., Chamon, C. & Mudry, C. Fractional Quantum Hall States at Zero Magnetic Field. *Physical Review Letters* **106,** 236804 (2011).

13. Sheng, D. N., Gu, Z.-C., Sun, K. & Sheng, L. Fractional quantum Hall effect in the absence of Landau levels. *Nature Communications* **2,** 389 (2011).

14. Regnault, N. & Bernevig, B. A. Fractional Chern Insulator. *Physical Review X* **1,** 021014 (2011).

15. Xiao, D., Zhu, W., Ran, Y., Nagaosa, N. & Okamoto, S. Interface engineering of quantum Hall effects in digital transition metal oxide heterostructures. *Nature Communications* **2,** 596 (2011).

16. Chang, C.-Z. *et al.* Experimental Observation of the Quantum Anomalous Hall Effect in a Magnetic Topological Insulator. *Science* **340,** 167–170 (2013).

17. Lu, Z. *et al.* Fractional quantum anomalous Hall effect in multilayer graphene. *Nature* **626,** 759–764 (2024).

18. Novoselov, K. S. *et al.* Two-dimensional gas of massless Dirac fermions in graphene. *Nature* **438,** 197–200 (2005).

19. Katsnelson, M. I., Novoselov, K. S. & Geim, A. K. Chiral tunnelling and the Klein paradox in graphene. *Nature Physics* **2,** 620–625 (2006).

20. Andrei, E. Y. & MacDonald, A. H. Graphene bilayers with a twist. *Nature Materials* **19,** 1265–1275 (2020).

21. Bistritzer, R. & MacDonald, A. H. Moiré bands in twisted double-layer graphene. *Proceedings of the National Academy of Sciences* **108,** 12233–12237 (2011).

22. Cao, Y. *et al.* Correlated insulator behaviour at half-filling in magic-angle graphene superlattices. *Nature* **556,** 80–84 (2018).

23. Cao, Y. *et al.* Unconventional superconductivity in magic-angle graphene superlattices. *Nature* **556,** 43–50 (2018).

24. Song, J. C. W., Samutpraphoot, P. & Levitov, L. S. Topological Bloch bands in graphene superlattices. *Proceedings of the National Academy of Sciences* **112,** 10879–10883 (2015).

25. Bultinck, N., Chatterjee, S. & Zaletel, M. P. Mechanism for Anomalous Hall Ferromagnetism in Twisted Bilayer Graphene. *Physical Review Letters* **124,** 166601 (2020).

26. Zhang, Y.-H., Mao, D. & Senthil, T. Twisted bilayer graphene aligned with hexagonal boron nitride: Anomalous Hall effect and a lattice model. *Physical Review Research* **1,** 033126 (2019).

27. Xie, M. & MacDonald, A. H. Nature of the Correlated Insulator States in Twisted Bilayer Graphene. *Physical Review Letters* **124,** 097601 (2020).

28. Zhang, Y.-H., Mao, D., Cao, Y., Jarillo-Herrero, P. & Senthil, T. Nearly flat Chern bands in moiré superlattices. *Physical Review B* **99,** 075127 (2019).

29. Sharpe, A. L. *et al.* Emergent ferromagnetism near three-quarters filling in twisted bilayer graphene. *Science* **365,** 605–608 (2019).

30. Serlin, M. *et al.* Intrinsic quantized anomalous Hall effect in a moiré heterostructure. *Science* **367,** 900–903 (2020).

31. Xu, Y. *et al.* Correlated insulating states at fractional fillings of moiré superlattices. *Nature* **587,** 214–218 (2020).

32. Li, T. *et al.* Quantum anomalous Hall effect from intertwined moiré bands. *Nature* **600,** 641–646 (2021).

33. Regan, E. C. *et al.* Mott and generalized Wigner crystal states in WSe2/WS2 moiré superlattices. *Nature* **579,** 359–363 (2020).

34. Liu, E. *et al.* Excitonic and Valley-Polarization Signatures of Fractional Correlated Electronic Phases in a WSe2\WS2 Moiré Superlattice. *Physical Review Letters* **127,** 037402 (2021).

35. Wang, X. *et al.* Moiré trions in MoSe2/WSe2 heterobilayers. *Nature Nanotechnology* **16,** 1208–1213 (2021).

36. Wang, X. *et al.* Light-induced ferromagnetism in moiré superlattices. *Nature* **604,** 468–473 (2022).

37. Park, H. *et al.* Dipole ladders with large Hubbard interaction in a moiré exciton lattice. *Nature Physics* **19,** 1286–1292 (2023).

38. Wang, X. *et al.* Intercell moiré exciton complexes in electron lattices. *Nature Materials* **22,** 599–604 (2023).

39. Huang, X. *et al.* Correlated insulating states at fractional fillings of the WS2/WSe2 moiré lattice. *Nature Physics* **17,** 715–719 (2021).

40. Li, H. *et al.* Imaging two-dimensional generalized Wigner crystals. *Nature* **597,** 650–654 (2021).

41. Li, T. *et al.* Charge-order-enhanced capacitance in semiconductor moiré superlattices. *Nature Nanotechnology* **16,** 1068–1072 (2021).

42. Wang, L. *et al.* Correlated electronic phases in twisted bilayer transition metal dichalcogenides. *Nature Materials* **19,** 861–866 (2020).

43. Ghiotto, A. *et al.* Quantum criticality in twisted transition metal dichalcogenides. *Nature* **597,** 345–349 (2021).

44. Wu, F., Lovorn, T., Tutuc, E., Martin, I. & MacDonald, A. H. Topological Insulators in Twisted Transition Metal Dichalcogenide Homobilayers. *Physical Review Letters* **122,** 086402 (2019).

45. Yu, H., Chen, M. & Yao, W. Giant magnetic field from moiré induced Berry phase in homobilayer semiconductors. *National Science Review* **7,** 12–20 (2020).

46. Kane, C. L. & Mele, E. J. Z2 Topological Order and the Quantum Spin Hall Effect. *Physical Review Letters* **95,** 146802 (2005).

47. Kane, C. L. & Mele, E. J. Quantum Spin Hall Effect in Graphene. *Physical Review Letters* **95,** 226801 (2005).

48. Deng, Y. *et al.* Quantum anomalous Hall effect in intrinsic magnetic topological insulator MnBi2Te4. *Science* **367,** 895–900 (2020).

49. Wu, F., Lovorn, T., Tutuc, E. & MacDonald, A. H. Hubbard Model Physics in Transition Metal Dichalcogenide Moiré Bands. *Physical Review Letters* **121,** 026402 (2018).

50. Tang, Y. *et al.* Simulation of Hubbard model physics in WSe2/WS2 moiré superlattices. *Nature* **579,** 353–358 (2020).

51. Anderson, E. *et al.* Programming correlated magnetic states with gate-controlled moiré geometry. *Science* **381,** 325–330 (2023).

52. Magorrian, S. J. *et al.* Multifaceted moiré superlattice physics in twisted WSe2 bilayers. *Physical Review B* **104,** 125440 (2021).

53. Liang, J. *et al.* Optically Probing the Asymmetric Interlayer Coupling in Rhombohedral-Stacked MoS2 Bilayer. *Physical Review X* **12,** 041005 (2022).

54. Zhang, Z. *et al.* Flat bands in twisted bilayer transition metal dichalcogenides. *Nature Physics* **16,** 1093–1096 (2020).

55. Naik, M. H. & Jain, M. Ultraflatbands and Shear Solitons in Moiré Patterns of Twisted Bilayer Transition Metal Dichalcogenides. *Physical Review Letters* **121,** 266401 (2018).

56. Devakul, T., Crépel, V., Zhang, Y. & Fu, L. Magic in twisted transition metal dichalcogenide bilayers. *Nature Communications* **12,** 6730 (2021).

57. Zhang, Y., Liu, T. & Fu, L. Electronic structures, charge transfer, and charge order in twisted transition metal dichalcogenide bilayers. *Physical Review B* **103,** 155142 (2021).

58. Crépel, V. & Fu, L. Anomalous Hall metal and fractional Chern insulator in twisted transition metal dichalcogenides. *Physical Review B* **107,** L201109 (2023).

59. Li, H., Kumar, U., Sun, K. & Lin, S.-Z. Spontaneous fractional Chern insulators in transition metal dichalcogenide moiré superlattices. *Physical Review Research* **3,** L032070 (2021).

60. Zang, J., Wang, J., Cano, J. & Millis, A. J. Hartree-Fock study of the moiré Hubbard model for twisted bilayer transition metal dichalcogenides. *Physical Review B* **104,** 075150 (2021).

61. Pan, H., Wu, F. & Das Sarma, S. Quantum phase diagram of a Moiré-Hubbard model. *Physical Review B* **102,** 201104 (2020).

62. Pan, H., Wu, F. & Das Sarma, S. Band topology, Hubbard model, Heisenberg model, and Dzyaloshinskii-Moriya interaction in twisted bilayer WSe2. *Physical Review Research* **2,** 033087 (2020).

63. Xian, L. *et al.* Realization of nearly dispersionless bands with strong orbital anisotropy from destructive interference in twisted bilayer MoS2. *Nature Communications* **12,** 5644 (2021).

64. Wang, X. *et al.* Interfacial ferroelectricity in rhombohedral-stacked bilayer transition metal dichalcogenides. *Nature Nanotechnology* **17,** 367–371 (2022).

65. Sung, J. *et al.* Broken mirror symmetry in excitonic response of reconstructed domains in twisted MoSe2/MoSe2 bilayers. *Nature Nanotechnology* **15,** 750–754 (2020).

66. Shimazaki, Y. *et al.* Strongly correlated electrons and hybrid excitons in a moiré heterostructure. *Nature* **580,** 472–477 (2020).

67. Yang, J. *et al.* Robust Excitons and Trions in Monolayer MoTe2. *ACS Nano* **9,** 6603–6609 (2015).

68. Lezama, I. G. *et al.* Indirect-to-Direct Band Gap Crossover in Few-Layer MoTe2. *Nano Letters* **15,** 2336–2342 (2015).

69. Robert, C. *et al.* Excitonic properties of semiconducting monolayer and bilayer MoTe2. *Physical Review B* **94,** 155425 (2016).

70. Miao, S. *et al.* Strong interaction between interlayer excitons and correlated electrons in WSe2/WS2 moiré superlattice. *Nature Communications* **12,** 3608 (2021).

71. Jin, C. *et al.* Stripe phases in WSe2/WS2 moiré superlattices. *Nature Materials* **20,** 940–944 (2021).

72. Li, T. Spontaneous quantum Hall effect in quarter-doped Hubbard model on honeycomb lattice and its possible realization in doped graphene system. *Europhysics Letters* **97,** 37001 (2012).

73. Wang, C. *et al.* Fractional Chern Insulator in Twisted Bilayer MoTe. *Physical Review Letters* **132,** 036501 (2024).

74. Qiu, W.-X., Li, B., Luo, X.-J. & Wu, F. Interaction-Driven Topological Phase Diagram of Twisted Bilayer MoTe2. *Physical Review X* **13,** 041026 (2023).

75. Xu, Y. *et al.* A tunable bilayer Hubbard model in twisted WSe2. *Nature Nanotechnology* **17,** 934–939 (2022).

76. Kumar, A., Hu, N. C., MacDonald, A. H. & Potter, A. C. Gate-tunable heavy fermion quantum criticality in a moiré Kondo lattice. *Physical Review B* **106,** L041116 (2022).

77. Zhao, W. *et al.* Gate-tunable heavy fermions in a moiré Kondo lattice. *Nature* **616,** 61–65 (2023).

78. Seifert, U. F. P. & Balents, L. Spin Polarons and Ferromagnetism in Doped Dilute Moiré-Mott Insulators. *Physical Review Letters* **132,** 046501 (2024).

79. Chang, C.-Z., Liu, C.-X. & MacDonald, A. H. Colloquium: Quantum anomalous Hall effect. *Reviews of Modern Physics* **95,** 011002 (2023).

80. Chen, G. *et al.* Tunable correlated Chern insulator and ferromagnetism in a moiré superlattice. *Nature* **579,** 56–61 (2020).

81. Nayak, C., Simon, S. H., Stern, A., Freedman, M. & Sarma, S. D. Non-Abelian Anyons and Topological Quantum Computation. *Reviews of Modern Physics* **80,** 1083–1159 (2008).

82. Hasan, M. Z. & Kane, C. L. Colloquium: Topological insulators. *Reviews of Modern Physics* **82,** 3045–3067 (2010).

83. Spanton, E. M. *et al.* Observation of fractional Chern insulators in a van der Waals heterostructure. *Science* **360,** 62–66 (2018).

84. Xie, Y. *et al.* Fractional Chern insulators in magic-angle twisted bilayer graphene. *Nature* **600,** 439–443 (2021).

85. Mai, P., Feldman, B. E. & Phillips, P. W. Topological Mott insulator at quarter filling in the interacting Haldane model. *Physical Review Research* **5,** 013162 (2023).

86. Cai, J. *et al.* Signatures of fractional quantum anomalous Hall states in twisted MoTe2. *Nature* **622,** 63–68 (2023).

87. Streda, P. Theory of quantised Hall conductivity in two dimensions. *Journal of Physics C: Solid State Physics* **15,** L717 (1982).

88. Bernevig, B. A. & Hughes, T. L. *Topological Insulators and Topological Superconductors* (Princeton University Press, 2013).

89. Nuckolls, K. P. *et al.* Strongly correlated Chern insulators in magic-angle twisted bilayer graphene. *Nature* **588,** 610–615 (2020).

90. Chernikov, A. *et al.* Exciton Binding Energy and Nonhydrogenic Rydberg Series in Monolayer WS2. *Physical Review Letters* **113,** 076802 (2014).

91. Popert, A. *et al.* Optical Sensing of Fractional Quantum Hall Effect in Graphene. *Nano Letters* **22,** 7363–7369 (2022).

92. Hayakawa, J., Muraki, K. & Yusa, G. Real-space imaging of fractional quantum Hall liquids. *Nature Nanotechnology* **8,** 31–35 (2013).

93. Vanhala, T. I. *et al.* Topological Phase Transitions in the Repulsively Interacting Haldane-Hubbard Model. *Physical Review Letters* **116,** 225305 (2016).

94. Reddy, A. P., Alsallom, F., Zhang, Y., Devakul, T. & Fu, L. Fractional quantum anomalous Hall states in twisted bilayer MoTe2 and WSe2. *Physical Review B* **108,** 085117 (2023).

95. Goldman, H., Reddy, A. P., Paul, N. & Fu, L. Zero-Field Composite Fermi Liquid in Twisted Semiconductor Bilayers. *Physical Review Letters* **131,** 136501 (2023).

96. Dong, J., Wang, J., Ledwith, P. J., Vishwanath, A. & Parker, D. E. Composite Fermi Liquid at Zero Magnetic Field in Twisted MoTe2. *Physical Review Letters* **131,** 136502 (2023).

97. Li, B., Qiu, W.-X. & Wu, F. *Electrically tuned topology and magnetism in twisted bilayer MoTe2 at vh=1* 2023. arXiv: 2310.02217[cond-mat].

98. Liu, X., Wang, C., Zhang, X.-W., Cao, T. & Xiao, D. *Gate-tunable antiferromagnetic Chern insulator in twisted bilayer transition metal dichalcogenides* 2023. arXiv: 2308.07488[cond-mat].

99. Song, X.-Y., Zhang, Y.-H. & Senthil, T. *Phase transitions out of quantum Hall states in moiré TMD bilayers* 2023. arXiv: 2308.10903[cond-mat].

100. Yu, J. *et al. Fractional Chern Insulators vs. Non-Magnetic States in Twisted Bilayer MoTe2* 2023. arXiv: 2309.14429[cond-mat].

101. Jia, Y. *et al. Moiré Fractional Chern Insulators I: First-principles calculations and Continuum Models of Twisted Bilayer MoTe2* 2023. arXiv: 2311.04958[cond-mat].

102. Luo, X.-J., Qiu, W.-X. & Wu, F. *Majorana zero modes in twisted transition metal dichalcogenides homobilayers* 2023. arXiv: 2308.09707[cond-mat].

103. Song, X.-Y., Jian, C.-M., Fu, L. & Xu, C. *Intertwined fractional quantum anomalous Hall states and charge density waves* 2023. arXiv: 2310.11632[cond-mat].

104. Morales-Durán, N., Wei, N., Shi, J. & MacDonald, A. H. Magic Angles and Fractional Chern Insulators in Twisted Homobilayer Transition Metal Dichalcogenides. *Physical Review Letters* **132,** 096602 (2024).

105. Reddy, A. P. & Fu, L. Toward a global phase diagram of the fractional quantum anomalous Hall effect. *Physical Review B* **108,** 245159 (2023).

106. Zhang, X.-W. *et al. Polarization-driven band topology evolution in twisted MoTe2 and WSe2* 2024. arXiv: 2311.12776[cond-mat].

107. Wang, T. *et al. Topology, magnetism and charge order in twisted MoTe2 at higher integer hole fillings* 2023. arXiv: 2312.12531[cond-mat].

108. Xu, C., Li, J., Xu, Y., Bi, Z. & Zhang, Y. Maximally localized Wannier functions, interaction models, and fractional quantum anomalous Hall effect in twisted bilayer MoTe2. *Proceedings of the National Academy of Sciences* **121,** e2316749121 (2024).

109. Fan, F.-R., Xiao, C. & Yao, W. Orbital Chern insulator at v=-2 in twisted MoTe2. *Physical Review B* **109,** L041403 (2024).

110. Sheng, D. N., Reddy, A. P., Abouelkomsan, A., Bergholtz, E. J. & Fu, L. *Quantum anomalous Hall crystal at fractional filling of moiré superlattices* 2024. arXiv: 2402.17832[cond-mat].

111. Fujimoto, M. *et al. Higher vortexability: zero field realization of higher Landau levels* 2024. arXiv: 2403.00856[cond-mat].

112. May-Mann, J., Stern, A. & Devakul, T. *Theory of Half-Integer Fractional Quantum Spin Hall Insulator Edges* 2024. arXiv: 2403.03964[cond-mat].

113. Crépel, V. & Regnault, N. *Attractive Haldane bilayers for trapping non-Abelian anyons* 2024. arXiv: 2403.05622[cond-mat].

114. Jian, C.-M., Cheng, M. & Xu, C. *Minimal Fractional Topological Insulator in half-filled conjugate moiré Chern bands* 2024. arXiv: 2403.07054[cond-mat].

115. Zhang, Y.-H. *Non-Abelian and Abelian descendants of vortex spin liquid: fractional quantum spin Hall effect in twisted MoTe2* 2024. arXiv: 2403.12126[cond-mat].

116. Zhang, L. & Song, X.-Y. *Moore-Read state in Half-filled Moiré Chern band from three-body Pseudo-potential* 2024. arXiv: 2403.11478[cond-mat].

117. Fan, F.-R., Xiao, C. & Yao, W. *Intrinsic Dipole Hall effect in tMoTe2 moiré: magnetoelectricity and contact-free signature of topological transitions* 2024. arXiv: 2403.16586[cond-mat].

118. Crépel, V., Ding, P., Verma, N., Regnault, N. & Queiroz, R. *Topologically protected flatness in chiral moiré heterostructures* 2024. arXiv: 2403.19656[cond-mat].

119. Ahn, C.-E., Lee, W., Yananose, K., Kim, Y. & Cho, G. Y. *First Landau Level Physics in Second Moiré Band of 2.1º Twisted Bilayer MoTe2* 2024. arXiv: 2403.19155[cond-mat].

120. Zeng, Y. *et al.* Thermodynamic evidence of fractional Chern insulator in moiré MoTe2. *Nature* **622,** 69–73 (2023).

121. He, H. *et al.* Accurate graphene quantum Hall arrays for the new International System of Units. *Nature Communications* **13,** 6933 (2022).

122. Willett, R. *et al.* Observation of an even-denominator quantum number in the fractional quantum Hall effect. *Physical Review Letters* **59,** 1776–1779 (1987).

123. Willett, R. L., Ruel, R. R., West, K. W. & Pfeiffer, L. N. Experimental demonstration of a Fermi surface at one-half filling of the lowest Landau level. *Physical Review Letters* **71,** 3846–3849 (1993).

124. Kang, W., Stormer, H. L., Pfeiffer, L. N., Baldwin, K. W. & West, K. W. How real are composite fermions? *Physical Review Letters* **71,** 3850–3853 (1993).

125. Goldman, V. J., Su, B. & Jain, J. K. Detection of composite fermions by magnetic focusing. *Physical Review Letters* **72,** 2065–2068 (1994).

126. Halperin, B. I. & Jain, J. K. *Fractional Quantum Hall Effects: New Developments* 551 pp. (World Scientific, 2020).

127. Park, H. *et al.* Observation of fractionally quantized anomalous Hall effect. *Nature* **622,** 74–79 (2023).

128. Wei, H. P., Chang, A. M., Tsui, D. C. & Razeghi, M. Temperature dependence of the quantized Hall effect. *Physical Review B* **32,** 7016–7019 (1985).

129. Shahar, D., Tsui, D. C., Shayegan, M., Bhatt, R. N. & Cunningham, J. E. Universal Conductivity at the Quantum Hall Liquid to Insulator Transition. *Physical Review Letters* **74,** 4511–4514 (1995).

130. Chang, C.-Z. *et al.* Observation of the Quantum Anomalous Hall Insulator to Anderson Insulator Quantum Phase Transition and its Scaling Behavior. *Physical Review Letters* **117,** 126802 (2016).

131. Xu, F. *et al.* Observation of Integer and Fractional Quantum Anomalous Hall Effects in Twisted Bilayer MoTe2. *Physical Review X* **13,** 031037 (2023).

132. Winkler, R. W., Kotthaus, J. P. & Ploog, K. Landau band conductivity in a two-dimensional electron system modulated by an artificial one-dimensional superlattice potential. *Physical Review Letters* **62,** 1177–1180 (1989).

133. Smet, J. H. *et al.* Magnetic Focusing of Composite Fermions through Arrays of Cavities. *Physical Review Letters* **77,** 2272–2275 (1996).

134. Hashimoto, K. *et al.* Quantum Hall Transition in Real Space: From Localized to Extended States. *Physical Review Letters* **101,** 256802 (2008).

135. Eisenstein, J. P., Pfeiffer, L. N. & West, K. W. Coulomb barrier to tunneling between parallel two-dimensional electron systems. *Physical Review Letters* **69,** 3804–3807 (1992).

136. He, S., Platzman, P. M. & Halperin, B. I. Tunneling into a two-dimensional electron system in a strong magnetic field. *Physical Review Letters* **71,** 777–780 (1993).

137. Read, N. Theory of the half-filled Landau level. *Semiconductor Science and Technology* **9,** 1859 (1994).

138. Garisto, D. Weird new electron behaviour in stacked graphene thrills physicists. *Nature* **628,** 16–17 (2024).

139. Nakamura, J., Liang, S., Gardner, G. C. & Manfra, M. J. Direct observation of anyonic braiding statistics. *Nature Physics* **16,** 931–936 (2020).

140. Bartolomei, H. *et al.* Fractional statistics in anyon collisions. *Science* **368,** 173–177 (2020).

141. Moore, G. & Read, N. Nonabelions in the fractional quantum hall effect. *Nuclear Physics B* **360,** 362–396 (1991).

142. Read, N. & Rezayi, E. Beyond paired quantum Hall states: Parafermions and incompressible states in the first excited Landau level. *Physical Review B* **59,** 8084–8092 (1999).

143. Geim, A. K. & Novoselov, K. S. The rise of graphene. *Nature Materials* **6,** 183–191 (2007).

144. Novoselov, K. S., Mishchenko, A., Carvalho, A. & Castro Neto, A. H. 2D materials and van der Waals heterostructures. *Science* **353,** aac9439 (2016).

145. Mak, K. F. & Shan, J. Photonics and optoelectronics of 2D semiconductor transition metal dichalcogenides. *Nature Photonics* **10,** 216–226 (2016).

146. Schaibley, J. R. *et al.* Valleytronics in 2D materials. *Nature Reviews Materials* **1,** 1–15 (2016).

147. Wang, G. *et al. Colloquium* : Excitons in atomically thin transition metal dichalcogenides. *Reviews of Modern Physics* **90,** 021001 (2018).

148. Huang, B. *et al.* Emergent phenomena and proximity effects in two-dimensional magnets and heterostructures. *Nature Materials* **19,** 1276–1289 (2020).

149. Carr, S., Fang, S. & Kaxiras, E. Electronic-structure methods for twisted moiré layers. *Nature Reviews Materials* **5,** 748–763 (2020).

150. Balents, L., Dean, C. R., Efetov, D. K. & Young, A. F. Superconductivity and strong correlations in moiré flat bands. *Nature Physics* **16,** 725–733 (2020).

151. Mak, K. F. & Shan, J. Semiconductor moiré materials. *Nature Nanotechnology* **17,** 686–695 (2022).

152. Törmä, P., Peotta, S. & Bernevig, B. A. Superconductivity, superfluidity and quantum geometry in twisted multilayer systems. *Nature Reviews Physics* **4,** 528–542 (2022).

153. Girvin, S. M. *The Quantum Hall Effect: Novel Excitations and Broken Symmetries* 1999. arXiv: `cond-mat/9907002`.

154. Shankar, R. *Theories of the Fractional Quantum Hall Effect* 2001. arXiv: `cond-mat/0108271`.

155. Jain, J. K. *Composite Fermions* 561 pp. (Cambridge University Press, 2007).

156. Stern, A. Anyons and the quantum Hall effect—A pedagogical review. *Annals of Physics. January Special Issue 2008* **323,** 204–249 (2008).

157. Goerbig, M. O. *Quantum Hall Effects* 2009. arXiv: `0909.1998[cond-mat]`.

158. Tong, D. *The Quantum Hall Effect* `https://www.damtp.cam.ac.uk/user/tong/qhe.html` (2024).

159. Xiao, D., Chang, M.-C. & Niu, Q. Berry phase effects on electronic properties. *Reviews of Modern Physics* **82,** 1959–2007 (2010).

160. Liu, C.-X., Zhang, S.-C. & Qi, X.-L. The Quantum Anomalous Hall Effect: Theory and Experiment. *Annual Review of Condensed Matter Physics* **7,** 301–321 (2016).

161. *Topology in Condensed Matter* TU Delft OCW. `https://ocw.tudelft.nl/courses/topology-condensed-matter-concept/` (2024).

162. Von Klitzing, K. in *The Quantum Hall Effect: Poincaré Seminar 2004* (eds Douçot, B., Pasquier, V., Duplantier, B. & Rivasseau, V.) 1–21 (Birkhäuser, Basel, 2005).

163. Englert, T. & Von Klitzing, K. Analysis of xx minima in surface quantum oscillations on (100) n-type silicon inversion layers. *Surface Science* **73,** 70–80 (1978).

164. Laughlin, R. B. Quantized Hall conductivity in two dimensions. *Physical Review B* **23,** 5632–5633 (1981).

165. Prange, R. E. & Girvin, S. M. *The Quantum Hall Effect* 487 pp. (Springer Science & Business Media, 2012).

166. Willett, R. L. Experimental evidence for composite fermions. *Semiconductor Science and Technology* **12,** 495 (1997).

167. Wu, Y.-L., Bernevig, B. A. & Regnault, N. Zoology of fractional Chern insulators. *Physical Review B* **85,** 075116 (2012).

168. Bernevig, B. A. & Regnault, N. Emergent many-body translational symmetries of Abelian and non-Abelian fractionally filled topological insulators. *Physical Review B* **85,** 075128 (2012).

169. Leinaas, J. M. & Myrheim, J. On the theory of identical particles. *Il Nuovo Cimento B* **37,** 1–23 (1977).

170. Wilczek, F. Quantum Mechanics of Fractional-Spin Particles. *Physical Review Letters* **49,** 957–959 (1982).

171. Arovas, D., Schrieffer, J. R. & Wilczek, F. Fractional Statistics and the Quantum Hall Effect. *Physical Review Letters* **53,** 722–723 (1984).

172. de-Picciotto, R. *et al.* Direct observation of a fractional charge. *Nature* **389,** 162–164 (1997).

173. Saminadayar, L., Glattli, D. C., Jin, Y. & Etienne, B. Observation of the e/3 Fractionally Charged Laughlin Quasiparticle. *Physical Review Letters* **79,** 2526–2529 (1997).

174. Samuelson, N. L. *et al. Anyonic statistics and slow quasiparticle dynamics in a graphene fractional quantum Hall interferometer* 2024. arXiv: `2403.19628[cond-mat]`.

175. Fowler, A. G., Mariantoni, M., Martinis, J. M. & Cleland, A. N. Surface codes: Towards practical large-scale quantum computation. *Physical Review A* **86,** 032324 (2012).

Appendix A

EXPERIMENTAL METHODS

A.1 Device Fabrication

Devices were fabricated using the tear-and-stack method. First, hBN, used as the gate dielectric, and graphite, used for the metallic gates, were mechanically exfoliated onto silicon (Si)/silicon dioxide (SiO_2) substrates. Homogeneous flakes were identified using an optical microscope. The hBN thickness was confirmed by atomic force microscope measurements. In an argon-filled glovebox with water and oxygen concentrations below 0.1 ppm, 2H $MoTe_2$ was mechanically exfoliated onto Si/SiO_2 substrates with a 285-nm oxide layer precleaned by oxygen plasma. Monolayer flakes were identified via optical microscope.

Standard polymer-based dry transfer techniques were used to fabricate the heterostructure. First, the topmost hBN protection layer, top graphite electrode, hBN top dielectric layer and half of the $MoTe_2$ monolayer were picked up. Then, the entire stage was rotated by the desired twist angle. After rotation, the second half of the $MoTe_2$ monolayer was picked up, forming the twisted $MoTe_2$ interface. The heterostructure was completed by picking up a long strip of graphite to serve as a grounding pin, a bottom hBN dielectric and the graphite bottom gate. The transfer process was performed at about 100 °C. The entire heterostructure was then put down and picked up repeatedly at about 140 °C to mechanically squeeze out trapped gas bubbles between layers, before being melted down onto the substrate at about 170 °C. The polymer was dissolved in anhydrous chloroform for 5 min in an inert glovebox environment. Standard electron beam lithography was used to electrically connect gold wire bonding pads to the gates and grounding pin of the fully encapsulated device. Lift off was performed in an inert glovebox environment with anhydrous dichloromethane.

A.2 Optical Measurements

All measurements were performed in a closed-loop magneto-optical exchange gas cryostat (attoDRY 2100) with an attocube xyz piezo stage, a 9T out-of-plane superconducting magnet and a base temperature of 1.6K. For PL measurements, a 632.8nm helium–neon laser was focused on the sample by a high-numerical-aperture non-magnetic objective to minimize the magnetic-field-induced drift. Differential reflectance measurements were performed under the same conditions using a tungsten–halogen lamp. The reflected signal was dispersed with a diffraction grating (Princeton Instruments, 600 grooves per mm at 1-µm blaze) and detected by an liquid nitrogen-cooled infrared charge-coupled device (Princeton Instruments PyLoN-IR 1.7). For PL measurements, a long-pass filter was inserted before the entrance to the spectrometer to remove reflected laser excitation. Excitation was linearly polarized. For polarization resolved measurements, a quarter wave plate and linear polarizer were used in the signal path to select out σ^+ and σ^- polarizations.

RMCD was performed by filtering a broadband supercontinuum source (NKT SuperK EXTREME EXW-12) by dual-passing through a monochromator, achieving a narrow excitation bandwidth in resonance with the trion feature. The out-of-plane magnetization of the sample induces an MCD signal ΔR, the difference between the reflected right- and left-circularly polarized light. To obtain the normalized RMCD $\Delta R/R$, the laser intensity was modulated by a chopping frequency p=850Hz and the phase was modulated by $\lambda/4$ via a photoelastic modulator at a frequency f=50kHz. The output signal of an indium-gallium-arsenide avalanche photodiode detector was read by two lock-in amplifiers (SR830). The ratio between the p-component signal I_p and the f-component signal I_f gives the RMCD signal: $\Delta R/R = I_f/(J_1(\pi/2) \times I_p)$ where J_1 is the first-order Bessel function. All zero-field RMCD plots are taken after the device was trained by application of a positive magnetic field, unless otherwise specified.

A.3 Transport Measurements

Transport measurements were conducted in a Bluefors dilution refrigerator with a 9T magnet and a base phonon temperature of about 20mK and electron temperature of about 80mK, as estimated from measurements of graphene devices with similar geometry. All AC signals were generated and detected by SR830 lock-in amplifiers. We found that a constant current measurement scheme

substantially improves the stability of the magnetic state compared with a constant voltage scheme. An AC current bias of about 0.2–0.5 nA was generated using a 100-MΩ resistor in series with an AC voltage source, and the actual current was monitored using a DL1211 current preamplifier. Four-terminal R_{xx} and R_{xy} signals were amplified using the differential mode of an SR560 voltage preamplifier with an input resistance (about 100 MΩ) much larger than the contact resistance of the device. Two-terminal conductance was measured by applying a 200–500-μV AC voltage bias to the source and by monitoring the drain current. For temperature dependence above 4K, the current on a resistive heater mounted near the sample was gradually ramped up, with the temperature read out using a Cernox sensor close to the sample. A test with a carbon film sensor mounted on the chip carrier showed that the temperature difference between the sensor and the sample stage temperature does not exceed 50mK.

A.4 Determination of Doping Density and Electric Field

The carrier density n and electric field D on the sample are converted from top (bottom) gate voltage V_{tg} (V_{bg}) using a parallel plate capacitor model: $n = (V_{tg}C_{tg} + V_{bg}C_{bg})/e - n_{offset}$ and $D/\epsilon_0 = (V_{tg}C_{tg} - V_{bg}C_{bg})/2\epsilon_0 - D_{offset}$, where C_{tg} and C_{bg} are the top and bottom gate capacitance obtained from the device geometry, e is the electron charge and ϵ_0 is the vacuum permittivity. The offset carrier density is derived from fitting to the integer and fractional states in PL spectra. The offset electric field is determined from the symmetric axis of the dual-gate RMCD map. The obtained doping density from the capacitor model can then be used to calculate twist angle from the assigned filling factors in the optical measurements, which is comparable to the targeted twist angle.

A.5 Determination of the Chern Number

The optical Landau fan diagram was obtained by integrating PL spectra over a 1-meV spectral range around the peak. Limiting the integration range to 1meV around the PL peak reduces background noise and increases contrast relative to simply integrating the entire spectral range, and thus improves the visibility of the correlated states. However, the main features of the fan diagram are independent of the choice of integration window. To determine the Chern number, first, using the doping density given by hBN capacitance ($C_g = \epsilon_{hBN}/d$, $\epsilon_{hBN} = 3.0$) and assuming the filling

to be linear in carrier density, the Landau fan diagram from the PL measurement can be reproduced. The hBN thickness is measured using an atomic force microscope with an uncertainty of about 200pm, which is negligible compared with the 20–40nm hBN. The most significant uncertainty comes from the dielectric constant of hBN (widely accepted as 3–3.3). Second, single-gated reflectance measurements are performed to obtain the capacitance ratio of the top and bottom gates, which matches the thickness ratio obtained by atomic force microscopy measurements. To quantitatively compare the optical fan diagram with the Streda formula dispersion, we extract the centroid of the integrated PL minimum as a function of carrier density for each value of the applied magnetic field. The centroid is obtained by calculating the geometric centre for the local minimum of the PL intensity. The error bar indicates a 5% deviation of the centroid PL intensity. Using the slope extracted from the Landau fan diagram, the capacitance of the gates can be obtained and compared with the hBN capacitance. This method cross-checks the validity of the hBN capacitance value.

Appendix B

FURTHER READING

B.1 2D Materials

- Geim, A. K. & Novoselov, K. S. The rise of graphene. *Nature Materials* **6,** 183–191 (2007)
- Novoselov, K. S. *et al.* 2D materials and van der Waals heterostructures. *Science* **353,** aac9439 (2016)
- Mak, K. F. & Shan, J. Photonics and optoelectronics of 2D semiconductor transition metal dichalcogenides. *Nature Photonics* **10,** 216–226 (2016)
- Schaibley, J. R. *et al.* Valleytronics in 2D materials. *Nature Reviews Materials* **1,** 1–15 (2016)
- Wang, G. *et al. Colloquium* : Excitons in atomically thin transition metal dichalcogenides. *Reviews of Modern Physics* **90,** 021001 (2018)
- Huang, B. *et al.* Emergent phenomena and proximity effects in two-dimensional magnets and heterostructures. *Nature Materials* **19,** 1276–1289 (2020)

B.2 Moiré Heterostructures

- Carr, S. *et al.* Electronic-structure methods for twisted moiré layers. *Nature Reviews Materials* **5,** 748–763 (2020)
- Andrei, E. Y. & MacDonald, A. H. Graphene bilayers with a twist. *Nature Materials* **19,** 1265–1275 (2020)
- Balents, L. *et al.* Superconductivity and strong correlations in moiré flat bands. *Nature Physics* **16,** 725–733 (2020)

- Mak, K. F. & Shan, J. Semiconductor moiré materials. *Nature Nanotechnology* **17,** 686–695 (2022)

- Törmä, P. *et al.* Superconductivity, superfluidity and quantum geometry in twisted multilayer systems. *Nature Reviews Physics* **4,** 528–542 (2022)

B.3 Quantum Hall Systems

- Girvin, S. M. *The Quantum Hall Effect: Novel Excitations and Broken Symmetries* 1999. arXiv: `cond-mat/9907002`

- Shankar, R. *Theories of the Fractional Quantum Hall Effect* 2001. arXiv: `cond-mat/0108271`

- Jain, J. K. *Composite Fermions* 561 pp. (Cambridge University Press, 2007)

- Stern, A. Anyons and the quantum Hall effect—A pedagogical review. *Annals of Physics. January Special Issue 2008* **323,** 204–249 (2008)

- Goerbig, M. O. *Quantum Hall Effects* 2009. arXiv: `0909.1998[cond-mat]`

- Tong, D. *The Quantum Hall Effect* `https://www.damtp.cam.ac.uk/user/tong/qhe.html` (2024)

B.4 Topology

- Nayak, C. *et al.* Non-Abelian Anyons and Topological Quantum Computation. *Reviews of Modern Physics* **80,** 1083–1159 (2008)

- Xiao, D. *et al.* Berry phase effects on electronic properties. *Reviews of Modern Physics* **82,** 1959–2007 (2010)

- Hasan, M. Z. & Kane, C. L. Colloquium: Topological insulators. *Reviews of Modern Physics* **82,** 3045–3067 (2010)

- Bernevig, B. A. & Hughes, T. L. *Topological Insulators and Topological Superconductors* (Princeton University Press, 2013)

- Liu, C.-X. *et al.* The Quantum Anomalous Hall Effect: Theory and Experiment. *Annual Review of Condensed Matter Physics* **7,** 301–321 (2016)

- *Topology in Condensed Matter* TU Delft OCW. `https://ocw.tudelft.nl/courses/topology-condensed-matter-concept/` (2024)

Appendix C

INTEGER AND FRACTIONAL QUANTUM HALL EFFECTS IN 2D ELECTRON GASSES

In this appendix, we will discuss the integer and fractional quantum Hall effects. These appear in two dimensional electron gasses under large applied magnetic fields, where the Fermi sea of electrons becomes discretized into Landau levels. These flat, topological bands contribute to a quantized Hall conductance σ_{xy} when fully filled. Even more surprising are the quantized values of Hall conductance which can appear at *fractional* fillings of these Landau levels. The theory which has been worked out in the course of understanding these fractional states has contributed greatly to our understanding of topological order.

Studies of the integer and fractional quantum Hall effects are generally conducted using ultraclean GaAs quantum wells, though 2D materials such as graphene have also been used. Our interest in these systems and their physics is twofold. First, the theory work explaining the IQHE and FQHE can serve as a baseline for understanding the FQAHE in our system. These are not exactly the same, of course - partially filled Landau levels are not the same as partially filled flat Chern bands, and the extent to which the two systems can be mapped onto each other is still an open question. However, FQH can serve as a starting point for us to build our understanding of moiré $MoTe_2$, and give us some intuition for where to look next.

The second major influence is on the experimental side. Decades of work and experimental optimization took place between the first discoveries of IQH and FQH in the 1980s and the current state of the art, where dozens of delicate fractional states can be seen in GaAs/AlGaAs MBE samples with mobilites exceeding 10 million $cm^2/V \cdot s$. A major lesson we can learn from these experiments is that the cleaner your sample is, the more physics you can observe. On the one hand, this could be seen to be somewhat discouraging - our moiré systems have twist angle disorder, bubbles, strain, carbon residue, impurities, relatively high contact resistances, and the mobility is nowhere near that of GaAs systems. But on the other hand, this means that the path forward is

clear - we know what we need to improve, and if we can take the trajectory of experimental work on the FQHE as any indication, the rewards will be great.

C.1 The Integer Quantum Hall Effect

The quantum Hall effect was discovered in the High Magnetic Field Laboratory in Grenoble on February 5th, 1980, at roughly 2 in the morning (Figure C.1a) [1]. A silicon MOSFET, equipped with a gate to control the carrier density, allowed for the measurement of the longitudinal (R_{xx}) and Hall (R_{xy}) resistances of a 2D electron gas (2DEG) under a large magnetic field as a function of gate voltage (Figure C.1b). For particular ranges of gate voltage, R_{xx} drops to nearly zero, and R_{xy} shows a finite plateau. Interestingly, Klaus von Klitzing, the discoverer of the QHE, had actually published a paper three years previously which showed these plateaus in R_{xy} [163]. The breakthrough here, however, was the realization that this plateau corresponds to a Hall conductivity quantized to an integer multiple of e^2/h. That is, a measurement of a real, imperfect device - at finite temperature, with impurities, disorder, surface roughness, etc. - somehow gives a value which depends on a set of fundamental, universal constants. As it turns out, explaining this depends on Landau levels, (a little bit of) disorder, and topology.

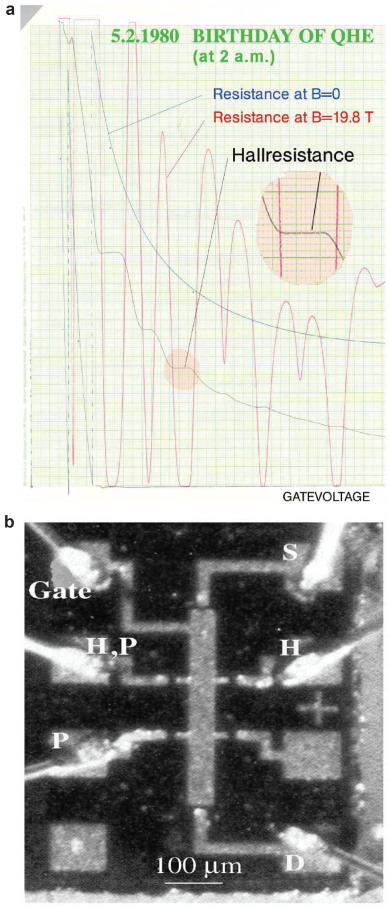

Figure C.1: Discovery of the integer quantum Hall effect. a, Original experimental tracing showing quantized plateaus in the Hall resistance. **b,** Silicon MOSFET of the type used in the first observation of the QHE. Figure adapted from Ref. [162]. Copyright 2005 Birkhauser Basel.

C.2 Landau Levels

Our goal in this section will be to get more familiar with the concepts underlying the integer quantum Hall effect, of which Landau levels play a central role. We will avoid going into too much detail here (some useful pedagogical texts can be found in Appendix B). It is, however, worth working through a derivation of the highly degenerate Landau levels. We will consider free electrons confined

to a plane (a 2DEG) with a magnetic field applied perpendicular to the plane. This magnetic field adds a vector potential term to the canonical momentum $\boldsymbol{p}$ in our free electron Hamiltonian:

$$H = \frac{\boldsymbol{p}^2}{2m} \rightarrow \frac{1}{2m}(\boldsymbol{p} + e\boldsymbol{A})^2\,, \qquad \boldsymbol{p} = m\dot{\boldsymbol{x}} - e\boldsymbol{A} \tag{C.1}$$

If we define the gauge-invariant mechanical momentum as

$$\boldsymbol{\pi} = \boldsymbol{p} + e\boldsymbol{A}$$

then our Hamiltonian becomes

$$H = \frac{\boldsymbol{\pi}^2}{2m} = \frac{1}{2m}(\pi_x^2 + \pi_y^2) \tag{C.2}$$

Importantly, the x and y components of our gauge-invariant momentum fail to commute, with their commutator determined by the magnetic length $l_B = \sqrt{\frac{\hbar}{eB}}$

$$[\pi_x, \pi_y] = -i\frac{\hbar^2}{l_B^2} \tag{C.3}$$

This looks exactly like a simple harmonic oscillator with the variables relabelled, and can be solved the same way. We create raising and lowering operators

$$a = \frac{l_B}{\sqrt{2}\hbar}(\pi_x - i\pi_y) \quad \text{and} \quad a^\dagger = \frac{l_B}{\sqrt{2}\hbar}(\pi_x + i\pi_y)$$

which results in a Hamiltonian

$$H = \hbar\omega_B\left(a^\dagger a + \frac{1}{2}\right) \tag{C.4}$$

where

$$\omega_B = \frac{\hbar}{ml_B^2} = \frac{eB}{m}$$

is the cyclotron frequency. The spectrum of this "simple harmonic oscillator" is

$$E = \hbar\omega_B\left(n + \frac{1}{2}\right) \qquad n \in \boldsymbol{N} \tag{C.5}$$

Note that the spacing between these energy levels is proportional to the magnetic field B - these are our Landau levels.

We can figure out the degeneracy of our Landau levels by creating another "momentum" which is not gauge invariant

$$\tilde{\boldsymbol{\pi}} = \boldsymbol{p} - e\boldsymbol{A}$$

However, the commutator of the components of $\tilde{\boldsymbol{\pi}}$

$$[\tilde{\pi}_x, \tilde{\pi}_y] = i\frac{\hbar^2}{l_B^2} \tag{C.6}$$

is gauge invariant. If we choose the symmetric gauge

$$\boldsymbol{A} = -\frac{yB}{2}\hat{\boldsymbol{x}} + \frac{xB}{2}\hat{\boldsymbol{y}} \tag{C.7}$$

the components of $\boldsymbol{\pi}$ and $\tilde{\boldsymbol{\pi}}$ commute, and we can define another pair of raising and lowering operators using the components of $\tilde{\boldsymbol{\pi}}$

$$b = \frac{l_B}{\sqrt{2}\hbar}(\tilde{\pi}_x + i\tilde{\pi}_y) \quad \text{and} \quad b^\dagger = \frac{l_B}{\sqrt{2}\hbar}(\tilde{\pi}_x - i\tilde{\pi}_y)$$

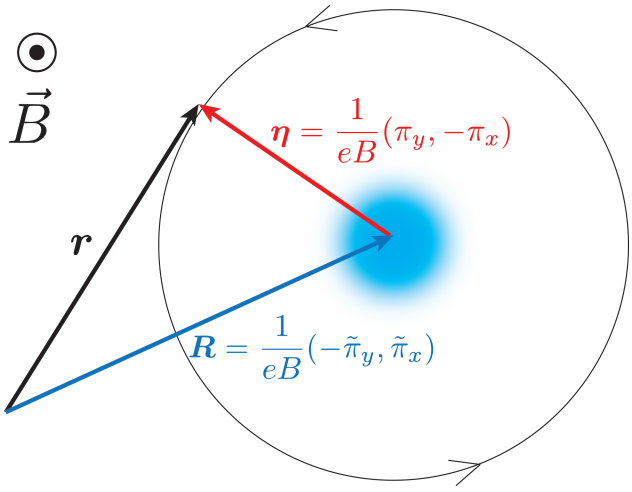

Figure C.2: Semiclassical picture of the LL degeneracy. Cyclotron motion in a magnetic field B. In the symmetric gauge, electron position $\boldsymbol{r}$ can be thought of as being a combination of the guiding center position $\boldsymbol{R}$, depending on the components of the gauge-dependent momentum $\tilde{\boldsymbol{\pi}}$ (blue), and the cyclotron variable $\boldsymbol{\eta}$, depending on the gauge-invariant momentum $\boldsymbol{\pi}$ (red). The failure of $\tilde{\pi}_x$ and $\tilde{\pi}_y$ to commute produces an uncertainty in the guiding center position on the order of l_B^2 (light blue).

This second set of operators allows us to determine the degeneracy of our Landau levels. Only the a and $a^\dagger$ operators show up in our Hamiltonian (Equation C.4), and the different sets of a and b operators commute. So while acting on our state with b and $b^\dagger$ can bring us to a different state, the energies will be equal - the Landau levels have degeneracy. There is a nice semiclassical picture of this degeneracy, if we make the right gauge choice. Electrons in a magnetic field undergo cyclotron motion. The position $\boldsymbol{r}$ of the electron in the cyclotron orbit can be broken up into a guiding center position $\boldsymbol{R}$ and a cyclotron coordinate $\boldsymbol{\eta}$ (Figure C.2). The energy of the electron is independent of $\boldsymbol{R}$ - that is, the center of the orbit can be translated around freely. In the symmetric gauge, $\boldsymbol{R}$ and $\boldsymbol{\eta}$ can be identified with the components of the gauge-dependent momentum $\tilde{\boldsymbol{\pi}}$ and gauge-invariant momentum $\boldsymbol{\pi}$, respectively. This makes some intuitive sense - our Hamiltonian, and the energy of our state, only cares about $\boldsymbol{\pi}$ and not

$\tilde{\boldsymbol{\pi}}$. Shifting around our guiding center - changing $\tilde{\boldsymbol{\pi}}$ - doesn't change the energy. However, the components of $\tilde{\boldsymbol{\pi}}$ fail to commute (Equation C.6). This leads to an uncertainty of the position of the guiding center - it is distributed over an area of $2\pi l_B^2$. For a sample with area A, the total number of states we can fit in the Landau level is then

$$N = \frac{A}{2\pi l_B^2} = \frac{eBA}{2\pi\hbar}$$

This gives us our Landau level degeneracy.

The raising and lowering operators we have worked out gives us a way to determine the wavefunctions of the Landau level states. Similarly to the simple harmonic oscillator, we can find the state $|n = 0, m = 0\rangle$ which is destroyed by both a and b, and then apply a series of raising operators $(a^\dagger)^n$ and $(b^\dagger)^m$ to find the rest of the states $|n, m\rangle$. If we consider only the lowest Landau level ($n = 0$) and work in complex coordinates, the wavefunction for the symmetric gauge is

$$\Psi_{LLL,m} \sim \left(\frac{z}{l_B}\right)^m e^{-|z|^2/4l_B^2} \qquad \text{(C.8)}$$

There are few things to note about this wavefunction. The first piece of $\Psi_{LLL,m}$ is a polynomial of z with degree m, and is analytic - that is, it depends only on z and not $\bar{z}$. Also, $\Psi_{LLL,m}$ is an eigenstate of the angular momentum operator

$$J = i\hbar\left(x\frac{\partial}{\partial y} - y\frac{\partial}{\partial x}\right) = \hbar(z\partial - \bar{z}\bar{\partial}) \qquad \text{(C.9)}$$

with eigenvalue $\hbar m$. Lastly, the wavefunction with degree m is radially symmetric and peaked at $r \approx \sqrt{2ml_B^2}$.

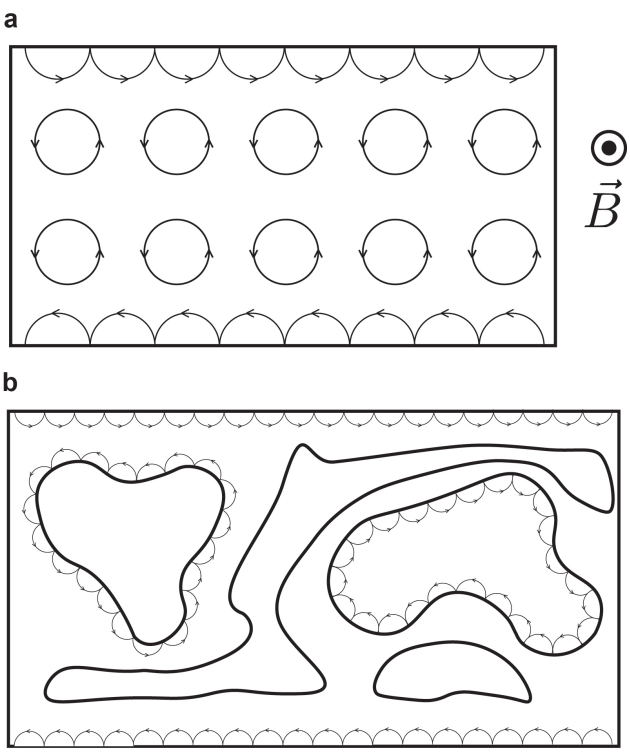

Figure C.3: Skipping orbits and disorder. **a,** Cyclotron motion and skipping orbits on sample edges. Skipping orbits move along equipotentials. **b,** Disorder-induced random background potential. Skipping orbits can form closed loops around local potential minima or maxima, producing localized states which don't contribute to the measured Hall conductivity.

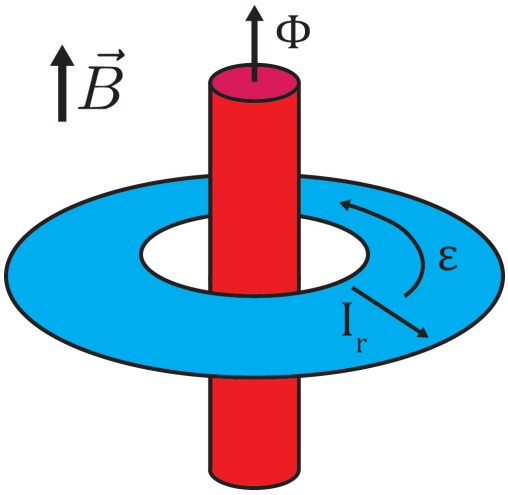

Figure C.4: Laughlin charge pumping. System is in the quantum Hall regime on a disc (blue). Adiabadically threading a flux Φ (red) induces an emf ε around the ring. As Φ is increased from 0 to $\Phi_0 = h/e$, the spectrum of the Hamiltonian returns to itself, and any localized states are unaffected. However, extended state wavefunctions undergo spectral flow, shifting from Ψ_m to Ψ_{m+1}, and one net charge is pumped radially from the inner to outer edge (I_r). The ratio of ε and I_r gives the quantized Hall resistance.

Now that we understand how Landau levels come about, and what the wavefunctions look like (if we have chosen the symmetric gauge) we can start to grasp why the quantized plateaus are seen in quantum Hall effect measurements. We can turn back to our semiclassical picture, and consider cyclotron motion. In the center of our sample, electrons will just complete cyclotron orbits. However, near the edges, the electrons hit the boundary and bounce back. However, the electrons can only orbit one way - they make chiral skipping orbits along the edge of the sample, in only one direction (Figure C.3a). Real samples, of course, aren't perfect - they have random disorder, background potential, etc. It is this characteristic that explains the plateaus. As the magnetic field is changed (and thus the filling, for a fixed electron density), we fill or empty available states. However, when there is disorder in the sample, many of these states are localized states - ie, skipping orbits around a local minimum or maximum within the bulk of the sample (Figure C.3b). Because we can only measure the channels which connect the electrical contacts at different spots on our sample, these local states won't change our measured conductivity. The observed plateaus in R_{xy} vs B are when these localized states are being filled or emptied.

Explaining the quantization of the plateaus is where topology comes in. Intuitively, one would expect that as some of the Landau level states are localized by disorder, the Hall conductivity would drop. This is not the case, however - the value of the Hall conductivity is a topological invariant of the Landau level. To get a flavor of how this works, we can follow Laughlin's argument for a 2DEG in the quantum Hall regime on a Corbino disc (Figure C.4) [164]. We will take our system to be gapped - ie, $\sigma_{xx} = 0$. We can induce an emf ε in the azimuthal direction by threading an additional flux Φ through the center of the disc. If we ramp Φ adiabatically from 0 to one flux quantum $\Phi_0 = h/e$, the induced emf will be $\varepsilon = -\partial\Phi/\partial t = -\Phi_0/T$ where T is the total time.

When we thread this flux quantum, any localized states will not be affected - the flux threading just applies a gauge transformation. In addition, the spectrum of our Hamiltonian will be the same for $\Phi = 0$ and for $\Phi = \Phi_0$.

However, the extended states will undergo *spectral flow*. That is, each eigenstate will shift to the next eigenstate, $\Psi_m \rightarrow \Psi_{m+1}$. As we can see from our symmetric gauge wavefunction C.8, increasing m corresponds to a radial shift outwards. Each extended state wrapping around the ring will be shifted outward to the next extended state; this "bucket brigade" results in a net pumping of one charge from the inner to outer edge. Importantly, this process is independent of the number of extended states. There are always two extended states (ie, one on the inner and one on the outer edge) from the geometry of the disc. Even if all the other states are localized, the spectral flow will adiabatically transform the inner extended state to the outer extended state, resulting in a pumping of one charge as one flux quantum is threaded through the disc.

If we have a single filled Landau level, we pump a single charge as the flux quantum is threaded in time T, giving us a radial current $I_r = -e/T$. If we combine this with our induced emf, we can get the Hall conductivity

$$\sigma_{xy} = \frac{I_r}{\varepsilon} = \frac{-e/T}{-\Phi_0/T} = \frac{e^2}{h} \tag{C.10}$$

This is exactly our quantized Hall conductivity for the lowest Landau level. As additional Landau levels are filled, we just multiply this e^2/h value by an integer. Thus, we can now explain the integer quantized plateaus seen in the Hall conductivity.

C.3 The Fractional Quantum Hall Effect

Two years after the quantum Hall effect was discovered, another observation was made which was even more bizarre. A cleaner GaAs/AlGaAs 2DEG was measured, and showed a quantized plateau corresponding to $\sigma_{xy} = 1/3 * (e^2/h)$ at 1/3 filling of the lowest Landau level (Figure C.5a). This is very strange - according to our discussion in the previous section, a Hall conductivity $\sigma_{xy} = (e^2/h)$ corresponds to a single electron being pumped across the disc as we thread one flux quantum. Having a *higher* quantized Hall conductivity - say $\sigma_{xy} = 3 * (e^2/h)$ - is normal. This corresponds to three electrons being pumped per flux quantum, which is the situation we have when there are three filled Landau levels. Quantization of σ_{xy} to a *fraction* of (e^2/h), however, would correspond

to a fraction of an electron charge being pumped per flux quantum. Electrons, of course, are fundamental particles - how is it possible to have a fraction of an electron?

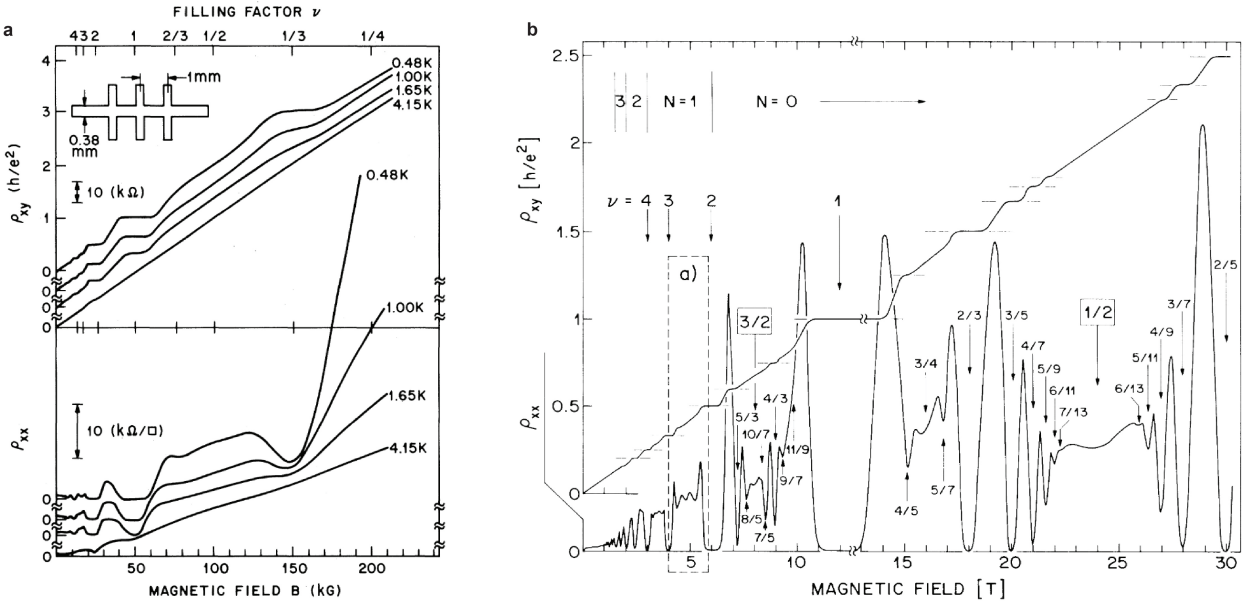

Figure C.5: The fractional quantum Hall effect. a, The first observation of the fractional quantum Hall effect, with Hall resistance quantized to $3h/e^2$. By the argument of the previous section, this corresponds to 'pumping' 1/3 of an electron charge. **b,** With cleaner samples, many more fractional states are observed, including even denominator states such as $\nu = 5/2$ Figures adapted from Refs. [2, 122]. (a) Copyright 1982 by the American Physical Society. (b) Copyright 1987 by the American Physical Society.

As sample quality improved further, many other fractional states were observed (Figure C.5b). Most of these are odd-denominator states, though there are also even-denominator ones such as $\nu = 5/2$. As it turns out, these fractional quantum Hall states are very exotic, strongly correlated phases of matter. As we discussed in the previous section, states within Landau levels are degenerate. Thus, the only relevant energy in a fractionally filled Landau level is the Coulomb repulsion of the electrons. It is this strongly correlated many-body system that allows for the emergence of an incompressible liquid with topological order. The quasiparticle excitations of FQH states are anyons, with fractional charge and fractional statistics (see Appendix E). Certain FQH states are expected to host non-Abelian anyons, which could be used for topologically protected quantum computation.

C.4 The Laughlin Picture

The Laughlin wavefunction describing the lowest Landau level at a fractional filling of $\nu = 1/m$, with $m = 3, 5, 7...$, is an extremely useful tool for understanding the properties of the FQH states. The wavefunction can be written as

$$\psi(z_i) = \prod_{i<j}(z_i - z_j)^m e^{-\sum_{i=1}^{n}|z_i|^2/4l_B^2} \tag{C.11}$$

Note that this looks somewhat similar to the lowest Landau level wavefunction in Equation C.8. In particular, the first term is analytic, as we would expect for a state within the lowest LL. There are, however, some other properties that make it effective in describing the $\nu = 1/m$ states.

One indication that this ansatz for the wavefunction of the FQH state is a good one is that it does a great job minimizing the Coulomb energy of the system. As we have discussed, the Coulomb energy is the only relevant energy scale in the partially filled Landau level problem - the kinetic energy is quenched. One way to see how the Coulomb energy is minimized is by looking at the effect of the $(z_i - z_j)^m$ term. For two particles at z_i and z_j, this term causes the wavefunction to become zero if $z_i = z_j$ - i.e., if the particles are in the same place. This is, of course, necessary for electrons, as they are fermions obeying Pauli exclusion. However, the 'zero' is not simply $(z_i - z_j)$, as is required by Pauli exclusion, but is actually of order m. That is, this wavefunction does a much better job keeping charges separated than is necessary for fermion statistics, and thus can keep the Coulomb energy low. This can be seen in the Monte Carlo simulation in Figure C.6a, particularly when compared to a Poisson distribution in Figure C.6b.

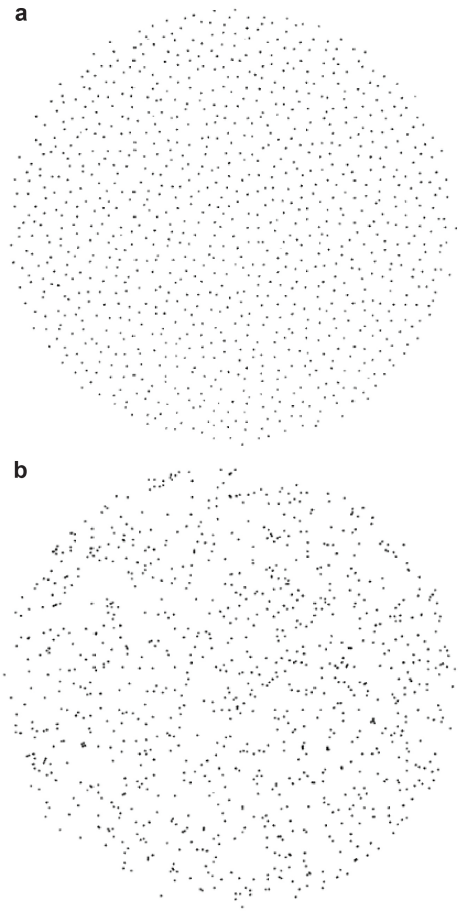

Figure C.6: Laughlin wavefunction distribution. a, Monte Carlo simulation of Laughlin wavefunction distribution of particles for $m = 3$. **b,** Poisson distribution of particles. Comparing the two figures, the Laughlin wavefunction is more effective for keeping particles separated. Figure adapted from Ref. [165]. Copyright 1990 Springer New York.

As we discuss in more depth in Appendix E, the quasiparticle and quasihole excitations of the Laughlin wavefunction are anyons. That is, they have a fractional charge, and fractional exchange statistics. While there are other approaches for understanding FQH states - as we discuss in the next section - seeing how these anyon excitations arise from the Laughlin wavefunction for the partially filled Landau level can be quite instructive.

C.5 Composite Fermions

We briefly discussed the idea of composite fermions in Chapter 6, with a particular focus on the composite Fermi liquid at $\nu = 1/2$. In this section, we will go in to a bit more detail on composite fermions, how they form, why they are such a nice description of FQH states, and experimental evidence for the CFL. The idea of the composite fermion picture, as illustrated in Figure C.7a, is that a 2D gas of electrons in a magnetic field will form bound states with two flux quanta, resulting in new fermionic particles - the composite fermions. Because the magnetic flux piercing the sheet is "consumed" to create the composite fermions, these particles will only feel a weak residual effective magnetic field, B_{eff}. At exactly half filling of the lowest Landau level, there are exactly two flux quanta per electron. Thus, at $\nu = 1/2$, $B_{eff} = 0$. As we know, fermions in zero magnetic field will form a Fermi liquid. In this case, the Fermi liquid is made of composite fermions - thus the composite Fermi liquid.

This result is actually quite surprising - $\nu = 1/2$ occurs at huge magnetic fields, on the order of 10T. The formation of a Fermi sea here is counterintuitive. As we will see, though, this composite Fermi liquid is quite real - experimentally, all of the expected signatures of a Fermi liquid (cyclotron orbits, geometric resonances, magnetic focusing, etc.) occur near $\nu = 1/2$. This composite fermion picture elegantly explains the FQH plateaus that we observe. These states can be though of as the *integer* quantum Hall states of the composite fermions in the *effective* magnetic field that arises as the filling moves away from $\nu = 1/2$ (or other even denominator fillings like $\nu = 1/4$). These composite fermion Landau levels are also commonly referred to as *Lambda levels*. Thinking in the composite fermion picture can also clarify some other puzzles, such as the gapped state at $\nu = 5/2$. This state can be viewed as, essentially, a BCS-like state of paired composite fermions [141]. Thus, the CFL picture is useful not only to describe Abelian states, but those predicted to be non-Abelian as well.

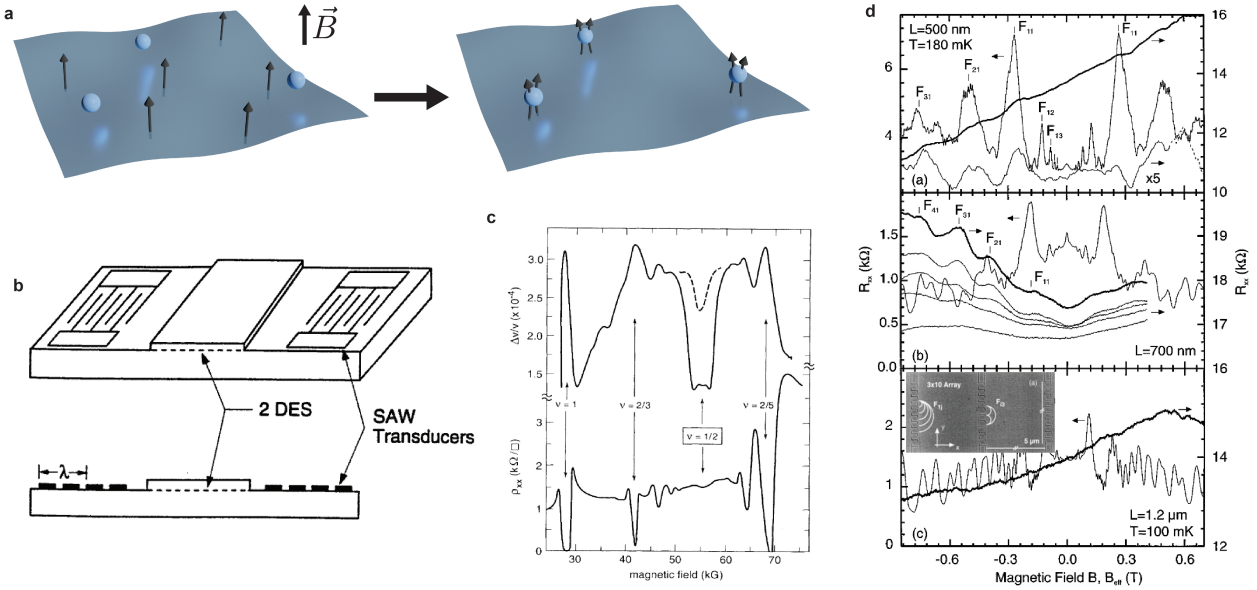

Figure C.7: The composite fermion picture. a, Schematic of composite fermion formation. Electrons bind with two flux quanta, resulting in composite fermions which feel a reduced effective magnetic field. A Fermi liquid of these composite fermions forms at $\nu = 1/2$. **b,** Schematic of sample for surface acoustic wave measurements, which probe finite wavevector conductivity. **c,** Comparison of velocity shift of SAW measurement, proportional to finite wavevector conductivity (top) and longitudinal resistance ρ_{xx} (bottom). A clear drop is seen in the SAW measurement at $\nu = 1/2$, indicating the formation of a CFL. **d,** Magnetic focusing spectra for electrons (left axis) and composite fermions (right axis) for various cavity array lengths vs B (B_{eff}). Peaks occur when cyclotron radius of the CF in the effective magnetic field (or electron in the magnetic field) is commensurate with the array spacing. Inset: SEM image of the cavity array. Figures adapted from Refs. [123, 133, 166]. (b) Copyright IOP Publishing. Reproduced with permission. All rights reserved. (c) Copyright 1993 by the American Physical Society. (d) Copyright 1996 by the American Physical Society.

There have been a few different experimental methods used to confirm the existence of a Fermi liquid near $\nu = 1/2$. The first were surface acoustic wave (SAW) measurements, which used SAW transducers to send an acoustic wave at finite wavevector q through a GaAs 2DEG (Figure C.7b). The measured velocity shift of the wave, $\Delta v/v$, can be related to the finite wavevector conductivity $\sigma_{xx}(\omega, q)$ of the 2DEG tuned to the partially filled LLL regime. The result of this measurement (Figure C.7c) is a dramatic drop in $\Delta v/v$ around $\nu = 1/2$ - a signature of the CFL. This drop is dependent on the SAW wavelength λ, which must be on the order of the composite fermion mean free path.

An additional probe of the CFL comes in the form of geometric resonances. That is, when the

cyclotron orbits of the composite fermions in B_{eff} are commensurate with a patterned potential grid, the measured resistance will change - just like electrons undergoing cyclotron orbits in B. This measurement is shown in Figure C.7d. Peaks in R_{xx} are observed in a sample equipped with a periodic cavity array both for electrons in B and CF in B_{eff}.

A commonality between these different measurement techniques for the CFL is that they require something beyond conventional transport techniques. While measurement of R_{xx} and R_{xy} can rule out a gapped state at $\nu = 1/2$, more involved measurements were required to directly investigate the CFL. As we discuss in Chapter 6, the unique optical properties of the moiré $MoTe_2$ system can serve as a powerful new probe of the *anomalous* composite Fermi liquid in the half filled flat moiré Chern band.

Appendix D

FRACTIONAL CHERN INSULATORS

As the focus of this dissertation is on the discovery of the fractional quantum anomalous Hall effect - a phenomenon arising in zero-field fractional Chern insulators - it bears going into a bit more detail on the theoretical and experimental background of FCIs. But before starting, it's worth thinking about why there has been so much interest in Chern insulators and fractional Chern insulators, as well as topology beyond Landau levels more generally. One reason is that, while fractional phases in Landau levels are extremely interesting, there are serious constraints when it comes to studying them experimentally, and especially to using them for practical applications. As we have discussed, these phases can only occur at very low temperature and high magnetic field in extremely clean samples. The most interesting phases - those predicted to host non-Abelian anyon excitations - are some of the most delicate. This is to be expected, of course - we are considering exotic quantum states of matter, and it's not too surprising that they will only emerge in fairly specific circumstances. However, there are unique properties of these phases which we would like to exploit to achieve, for example, topologically protected quantum computation (see Appendix E). Restricting ourselves to Landau levels makes this extremely difficult. Might there be a way to realized these phases *without* Landau levels?

A second reason for this interest is the possibility for more and different physics than can be realized in Landau level systems. To some extent, this has to do with the flexibility of, for example, systems hosting FCIs in flat Chern bands over a 2DEG in the Landau level regime. Hybridizing other phases, such as superconductors, with zero-field FCIs is feasible, whereas the large magnetic field required for FQH destroys superconductivity. But beyond this, flat Chern bands are not the same thing as Landau levels - the states which arise in them may be even richer and more interesting than those that have been seen so far in Landau level systems.

D.1 Chern Bands

The first model for a quantized Hall effect without net magnetic field or the formation of Landau levels was the celebrated Haldane model [9]. This model is built on a hexagonal lattice, with both nearest-neighbor (NN) and next-nearest-neighbor (NNN) hopping (Figure D.1a). Crucially, the NNN hopping can pick up a complex phase. In the original model, this was accomplished by threading fluxes through different regions within the unit cell, with a net flux through the entire unit cell being zero. As we discussed in Chapter 2, however, there are other ways to get this complex hopping. In the case of moiré $MoTe_2$, this is accomplished with the effective real space magnetic field which varies over the moiré unit cell generated by the layer pseudospin skyrmion texture [44, 45]. Also included in the model is a sublattice-dependent energy M, which acts with $+M$ on A sites (white dots) and $-M$ on B sites (black dots).

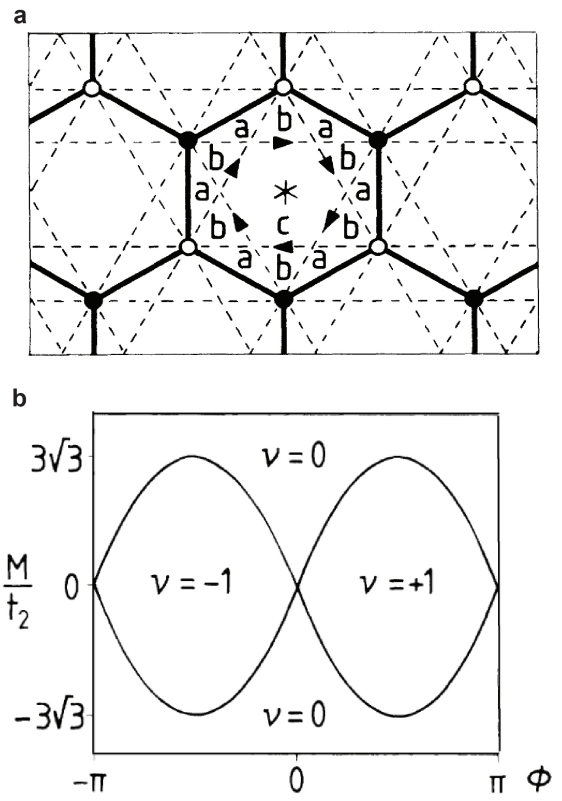

Figure D.1: The Haldane model. a, Schematic of the Haldane model. Nearest neighbor (solid) and next-nearest neighbor (dotted) hopping between sites is included in the model. Next nearest neighbor hopping is complex, with direction of increasing phase shown by arrows. **b,** Phase space of the quantum anomalous Hall effect. For finite NNN phase and sufficiently small sublattice energy offset M, $\sigma_{xy} = \nu e^2/h$, with $\nu = \pm 1$ Figure adapted from [9]. Copyright 1988 by the American Physical Society.

For a particular range of parameters - namely, finite NNN hopping phase Φ and sufficiently small M, the Hall conductivity will take a finite, quantized value of $\sigma_{xy} = \pm e^2/h$ (Figure D.1b). This was the first example of what are now called *Chern insulators* - that is, systems which host topologically nontrivial Bloch bands (Chern bands) and which can show a quantized Hall effect at zero magnetic field (the quantum anomalous Hall effect). Since, a wide variety of toy models have also been shown to have this property. In addition, the quantum anomalous Hall effect has been observed in multiple systems - magnetically doped topological

insulators [16], intrinsic magnetic TIs [48], and both graphene and TMD moiré systems [30, 32]. The commonality between all of these is the coexistence of topological bands and spontaneous time reversal symmetry breaking (i.e., ferromagnetism).

D.2 Fractional Chern Insulators: Theory

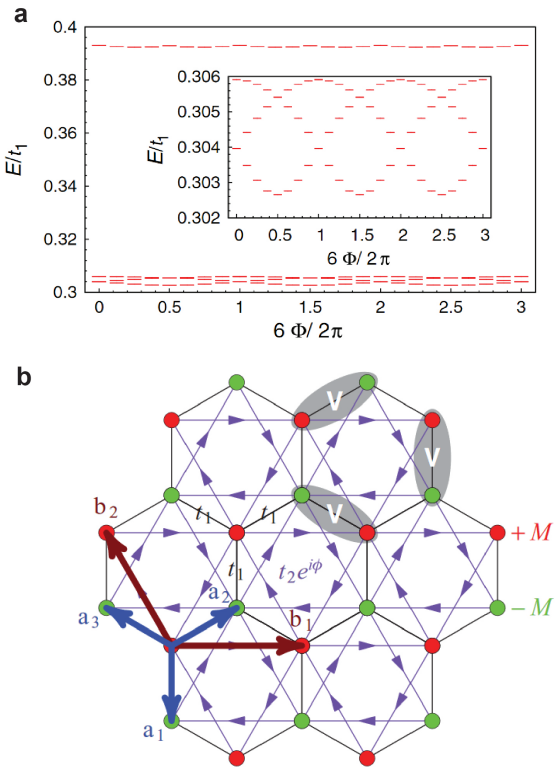

Figure D.2: Fractional Chern Insulators: Theory. a, Exact diagonalization of a 1/3 filled flat Chern band. 3-fold degenerate ground state spectrum undergoes spectral flow upon flux insertion. **b,** The Haldane model with density-density interaction V. Exact diagonalization calculations at 1/3 filling indicates that the system hosts and FCI. Figures adapted from [14, 167]. (a) Reproduced with permission under CC BY 3.0. (b) Copyright 2012 by the American Physical Society.

As we have discussed in the previous chapter, the physics arising in the fractional quantum Hall states in the partially filled Landau levels is much more exotic than that of the integer quantum Hall states. These physics, which arise from strong correlations between the electrons, include electron fractionalization and anyonic quasiparticle excitations. Non-Abelian anyons, in particular, are highly sought after. It is no surprise, then, that significant theory work has been done to explore the possibility of a zero-field fractional quantum Hall effect. In a flurry of activity in 2011 and 2012, it was established that zero field fractional Chern insulators - phases showing the fractional quantum anomalous Hall effect - were possible [10–15, 168].

A range of theoretical techniques have been used to study FCIs, but one of the more common is exact diagonalization of the Hamiltonian and investigation of the low energy spectrum. Taking this approach for a checkerboard lattice model in the flat band limit at 1/3 filling, it was shown that there is a 3-fold degenerate ground state. Upon flux insertion, these ground states undergo spectral flow into each other, indicating an FCI (Figure D.2a). However, FCIs can occur in a variety of different lattice models, including the Haldane model with the addition of

density-density interactions (Figure D.2b). The general requirements for FCIs are the same as for Chern insulators - topological Bloch bands and spontaneous TRS breaking - but with the additional requirement of strong interactions. This makes sense - the FQH states in Landau levels arise from strong Coulomb interactions between electrons, so it is not a surprise that flat bands and strong interactions are necessary for zero field FCIs.

D.3 FCIs at Finite Field

We now turn to the experimental side, and discuss experimental progress in the search for fractional Chern insulators. Moiré engineering of graphene heterostructures has played a key role here. Determining the topological properties of the states in these moiré graphene systems has relied on measurements of compressibility - which shows insulating states - vs magnetic field. As we discuss in Chapter 4, the slope of filling vs applied magnetic field, when compared to the predictions of the Streda formula, can give information on the topological properties of the state.

Two different moiré systems were observed to host FCIs - that is, a non-FQH topologically ordered state in a fractionally filled Chern band - at finite magnetic field. The first of these measured penetration capacitance (C_P) of a graphene bilayer aligned to hBN on one side, forming a moiré superlattice. C_P changes when an insulating state is formed, allowing a Landau fan diagram to be obtained by measuring C_P vs filling and magnetic field (Figures D.3a,c). A range of different topological states are observed, which can be identified based on their slopes and intercepts and are labelled in the Wannier diagrams (Figures D.3b,d). A key observation was that there were states with fractional slopes at fractional fillings of Harper-Hofstadter bands. The formation of these bands relies on both the magnetic field and the superlattice potential. Thus, this measurement reveals fractional states that exist in topological bands which are not Landau levels. However, the FCIs only emerge at high magnetic fields, as they require the formation of these Harper-Hofstadter bands.

Another capacitance measurement using a single-electron transistor (SET) was performed on magic angle twisted bilayer graphene (MATBG). As discussed above, and in Chapter 2, MATBG exhibits the quantum anomalous Hall effect, which shows that it hosts Chern bands and spontaneous time reversal symmetry breaking. Thus, two of the three criteria for zero-field FCIs are met, and it is natural to look for them in this system. The measurement showed fractional Chern insulators

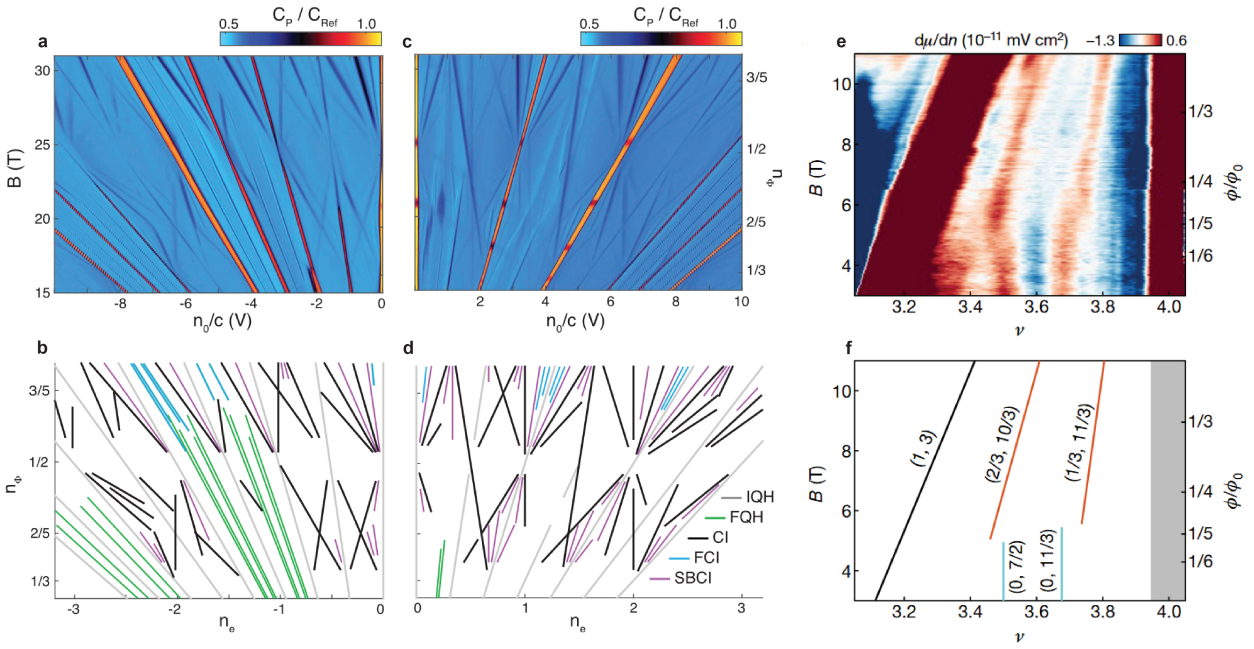

Figure D.3: FCIs at finite magnetic field. a&b, Penetration capacitance measurement of bilayer graphene-hBN moiré vs filling and magnetic field, compared to a Wannier diagram with various classes of topological states labelled. Large positive out-of-plane electric field is applied to force electrons close to the aligned hBN layer where the moiré resides. **c&d,** as in (a&b), but with negative electric field forcing electrons away from the moiré. Fractional Chern insulators are observed at high field at fractional fillings of Harper-Hofstadter bands. **f&g,** Compressibility measurements of magic-angle twisted bilayer graphene vs filling and magnetic field, and corresponding Wannier diagram. FCIs survive to a low magnetic field of ∼5T Figures adapted from Refs. [83, 84]. (a) Reprinted with permission from AAAS. (b) Reproduced with permission from Springer Nature.

which emerge at at much lower magnetic fields than the bilayer graphene-hBN moiré system, at ∼5T (Figures D.3e,f). The small magnetic field onset of these FCIs indicates that the primary role of the magnetic field here is to redistribute the Berry curvature of the moiré Brillouin zone to make the bands more conducive for hosting FCIs.

The next part of the story, of course, is the search for FCIs which exist at zero field. As we have discussed at length in the above chapters, the first system shown to host zero-field FCIs was moiré $MoTe_2$, followed shortly thereafter by the pentalayer graphene/hBN moiré. Though there is still much work to be done to understand these theoretically, the general intuition in the search for the fractional quantum anomalous Hall effect was quite accurate - look for flat Chern bands and strong electron-electron interactions. As we can see from these two systems, moiré engineering turns out

to be a very effective way to do this.

Appendix E

ANYONS

Particle exchange statistics is one of those topics that seems to get more complicated the more you learn about it. In three spatial dimensions, the spin-statistics theorem proves that particles with integer spin are bosons following Bose-Einstein statistics, and half-integer spin particles are fermions following Fermi-Dirac statistics. Though the relationship is easy to state, there aren't - as far as I'm aware - any derivations of this that are simultaneously simple, intuitive, and rigorous.

The purpose of this appendix is to serve as an introduction to particle exchange statistics in 2+1 dimensions and how it differs from the more familiar 3+1 dimensions, so we will avoid any rigorous proofs. Our goal, rather, is to explore what kinds of particles can live in the 2D plane. It turns out that confining ourselves to 2 dimensions gives us a much richer array of possible particle types, beyond just bosons and fermions. These new types of particles are anyons. As we will see, these particles can have both Abelian and non-Abelian exchange statistics, and particular types of non-Abelian anyons can be used to perform quantum computation.

E.1 Fermions, Bosons, and Beyond

As mentioned above, the two kinds of particles that exist in our 3+1 dimensional spacetime are bosons and fermions, with integer and half-integer spins, respectively. The key difference between the two is how a many-particle wavefunction evolves upon particle exchange. Let's consider two identical bosons. If we exchange the particles, the two-particle wavefunction, ψ, will remain the same. However, for two identical fermions, the wavefunction will pick up a negative sign upon exchange: $\psi \to -\psi$. Note that in both of these cases, exchanging the particles twice (or, equivalently, taking one particle in a loop around the other) gives back the same wavefunction. This is necessary in 3 spatial dimensions: we can always "take the loop out of the plane", so to speak, so that looping one particle around the other is topologically equivalent to doing nothing (see Figure E.1).

This sort of movement provides an intuitive picture of why the wavefunction either staying the

same or picking up a minus sign are the only options in 3+1D - these are the only possibilities if we want two particle exchanges to give back the same wavefunction. This logic generalizes to any number of particles - permuting particle positions in a many-boson wavefunction gives back the same wavefunction, and doing the same with a many-fermion wavefunction will give a plus or minus sign, depending on the parity of the permutation. While these rules may seem simple, their consequences are profound. The Pauli exclusion principle, for instance, is a direct result of the exchange statistics for fermions, and leads, among many other things, to the stability of matter.

As we might imagine from this looping argument, confining our particles to 2+1 dimensional spacetime could remove this constraint to only fermions and bosons. In this case, it would seem that the wavefunction does not necessarily need to remain unchanged after performing two particle exchanges. It turns out that this is correct, and was worked out by Leinaas and Myrheim [169] and Frank Wilczek [170]. Exchanging two particles can lead to the wavefunction picking up a phase:

$$\psi \to e^{i\theta}\psi \tag{E.1}$$

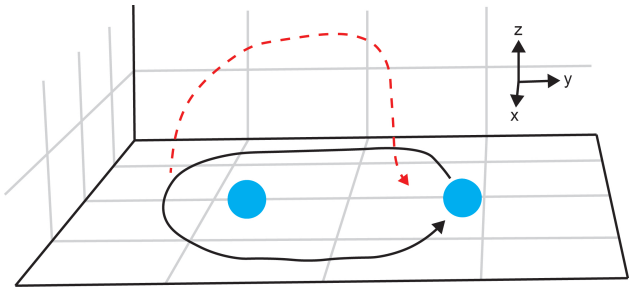

Figure E.1: Particle loop in three dimensions. We take one particle all the way around the other (black line). Because of the dimensionality of the space, we can "move the loop out of the plane" (red dotted line), making this looping topologically equivalent to doing nothing. This type of movement is not possible when confined to two dimensions.

In the cases of $\theta = 0$ or $\theta = \pi$, we would simply have bosons or fermions (which, of course, still exist in 2D). Because of the dimensionality of the space, however, we have other options - there can be particles with other "statistical angles" θ, dubbed "anyons" by Wilczek.

E.2 The Braid Group

The key to understanding this 2+1 dimensional particle exchange behavior is that rather than particle exchanges corresponding to elements of the permutation group, as in 3+1D, they instead correspond to elements of the braid group (Figure E.2). Unlike in more conventional 3+1 spacetime, the worldlines of 2+1 particle exchanges cannot be 'unwound' without intersecting each other. Consider, for example, performing two interchanges of particles 1 and 2 - in the figure, applying σ_1

twice. Because we can't "untangle the worldlines", the end state of our system does not necessarily need to correspond to our initial state - $\sigma_1^2 \neq 1$. In addition, switching the order of exchange operations does not necessarily lead to the same result. See, for example, the failure of σ_1 and σ_2 to commute in Figure E.2b. These properties mean that the braid group is non-Abelian.

Because particles in 2+1D transform under representations of the braid group, exchange statistics are not limited to the ± 1 of bosons and fermions, but can lead to an arbitrary phase, in the case of Abelian anyons. In Figure E.2c, we see that the braid group has the relation $\sigma_1\sigma_2\sigma_1 = \sigma_2\sigma_1\sigma_2$, which means that, for identical Abelian anyons, all of the exchanges pick up the same phase. In the case of non-Abelian anyons - which we will discuss in section E.5 - particle exchange can lead not just to a phase, but to a unitary operation being performed on the ground state subspace. As it turns out, this property makes it possible to use non-Abelian anyons to perform quantum computation.

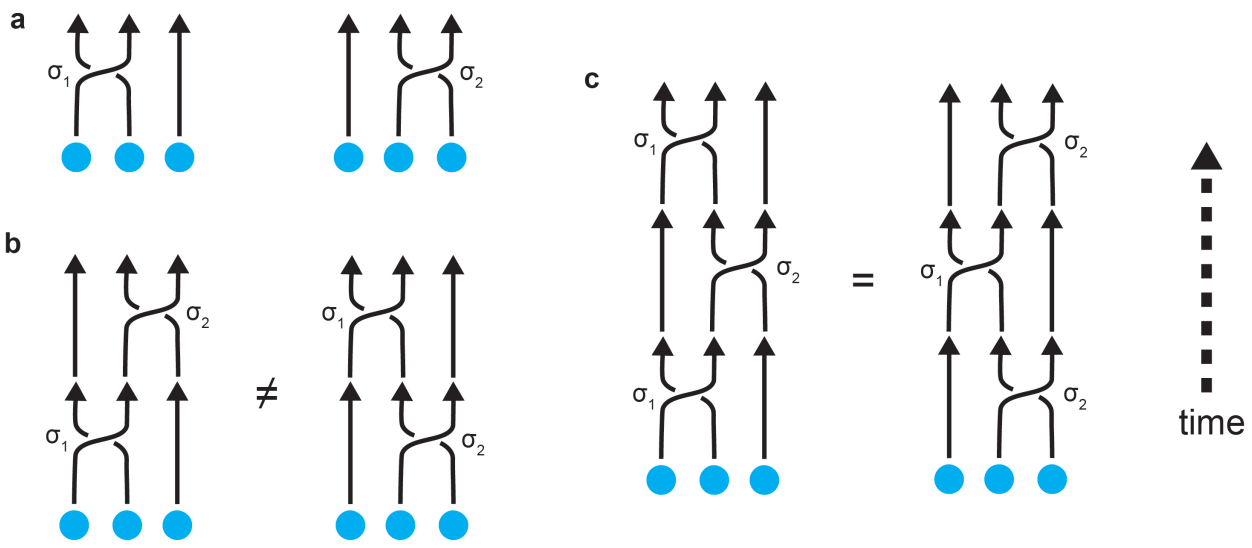

Figure E.2: The braid group. a, Two elementary braid operations, σ_1 and σ_2, which exchange particles 1, 2 and 2, 3, respectively. **b,** The operation $\sigma_1\sigma_2$ is not equivalent to $\sigma_2\sigma_1$ - the braid group is non-Abelian. **c,** "Shifting around the exchanges" gives the braid relation $\sigma_1\sigma_2\sigma_1 = \sigma_2\sigma_1\sigma_2$.

E.3 Anyons in the Fractional Quantum Hall States

This is all, of course, pretty abstract. After all, we live in 3+1 spacetime dimensions, and are familiar with the behavior of fermions and bosons, but what would having these exotic exchange statistics even entail? And just because it is theoretically possible for anyons to exist in 2D doesn't imply that they can be realized experimentally. Luckily, though confining electrons to a 2D plane doesn't change their fermionic statistics, the quasiparticle excitations of fractional quantum Hall states (which we discussed in Appendix C) are anyons. The Laughlin state at filling $\nu = 1/m$, for example, will have quasiparticle excitations with a statistical angle $\theta = \pi/m$ and charge e/m.[1]

We can get some understanding of why the quasiparticle excitations have these fractional statistics by looking at the Laughlin wavefunction:

$$\psi(z_i) = \prod_{i<j}(z_i - z_j)^m e^{-\sum_{i=1}^{n}|z_i|^2/4l_B^2} \tag{E.2}$$

where we use complex variables, and l_B is the magnetic length. As mentioned in Appendix C, this wavefunction does a great job at lowering the Coulomb energy for a Landau level at filling $\nu = 1/m$, and serves as an extremely useful tool for understanding the physics of the fractional quantum Hall effect. We want to add quasiparticles - in this case quasi-holes - to the Laughlin state. we can do this by "adding zeros" to the wavefunction at different positions η_j, giving a total of M quasi-holes:

$$\psi_{quasi-holes}(z_i;\eta) = \langle z, \overline{z}|\eta_i, ..., \eta_M\rangle = \prod_{j=1}^{M}\prod_{i=1}^{N}(z_i - \eta_j)\prod_{k<l}(z_k - z_l)^m e^{-\sum_{i=1}^{n}|z_i|^2/4l_B^2} \tag{E.3}$$

Essentially, we have tacked on some terms to the front of $\psi(z_i)$ which make the electron density go to zero at η_j - thus "quasi-hole".

To work out the statistics of the quasi-holes, we need to find the Berry phase that is picked up when taking one of them in a loop around the other. We need the normalized wavefunction, which we get by determining the normalization factor Z:

$$|\psi\rangle = \frac{1}{\sqrt{Z}}|\eta_i, ..., \eta_M\rangle = \frac{1}{\sqrt{Z}}|\eta\rangle \tag{E.4}$$

[1]The discussion over the next few pages will really only scratch the surface of the physics of the Laughlin states and their excitations. The goal is to give a flavor of how anyons can naturally come about from the Laughlin wavefunction, but we will not go into quasiparticle excitations (which are more complicated than quasi-holes), neutral excitations, Wigner crystals at low filling, etc. Some nice sets of lecture notes which dive deeper into these topics are Refs. [153, 156–158].

$$Z = \langle \eta_i, ..., \eta_M | \eta_i, ..., \eta_M \rangle = \int \prod d^2 z_i \exp(\sum_{i,j} \log |z_i - \eta_j|^2 + m \sum_{k,l} \log |z_k - z_l|^2 - \frac{1}{2l_B^2} \sum_i |z_i|^2) \tag{E.5}$$

We are in the lowest Landau level, and our wavefunction $|\eta\rangle$ is holomorphic, so the Berry connection for the quasi-holes is:

$$\mathbf{A}_\eta(\eta, \overline{\eta}) = -i \langle \psi | \frac{\partial}{\partial \eta} | \psi \rangle = \frac{i}{2Z} \frac{\partial Z}{\partial \eta} - \frac{i}{Z} \langle \eta | \frac{\partial}{\partial \eta} | \eta \rangle = -\frac{i}{2} \frac{\partial \log Z}{\partial \eta} \tag{E.6}$$

The anti-holomorphic Berry connection $\mathbf{A}_{\overline{\eta}}$ is the same, but with the opposite sign and with η replaced by $\overline{\eta}$.

To actually make progress evaluating the Berry connection - which we need to know to work out the quasi-hole statistics - we will have to take derivatives of Z in equation E.5. This is not a trivial task. However, we an take advantage of the famous *plasma analogy* [4, 171] - mapping the quasi-hole wavefunction onto a partition function for a 2D plasma of charged particles. Then, using our intuition for the behavior of the fake plasma, it's possible to make some progress on figuring out how our actual wavefunction, $\psi_{quasi-holes}$, will behave. We can write down Z in the form of a partition function:

$$Z = \int \prod d^2 z_i e^{-\beta U(z_i)} \tag{E.7}$$

In doing this, we can see that the term in the exponent in equation E.5 maps nicely to $-\beta U(z_i)$. In particular, if we take the inverse temperature $\beta = 2/m$, we can get a potential energy which looks like

$$U(z_i) = -m^2 \sum_{i<j} \log \left(\frac{|z_i - z_j|}{l_B} \right) + m \sum_i \log \left(\frac{|z_i - \eta|}{l_B} \right) + \frac{m}{4l_B^2} \sum_{i=1}^{N} |z_i|^2 \tag{E.8}$$

This gives us our "plasma". The first term looks like the Coulomb potential in 2D between two particles of charge $-m$ at locations z_i and z_j - recall that the Coulomb potential in 2D goes as $\log(r)$. The last term looks like a constant background charge density of $\rho_0 = -1/2\pi l_B^2$. Without any added quasi-holes, we would expect the "charges" in the first term to want to spread out and neutralize the background charge density. Since each particle has charge $-m$, the needed density n to compensate the background charge is $nm = \rho_0$, giving $n = 1/2\pi l_B^2 m$, or a filling fraction of $\nu = 1/m$, as we expect.

Now, considering the second term in equation E.8, we can see that this looks like adding a charged impurity to our plasma at position η. However, in this case, the impurity has a charge of 1, rather than $-m$. This gives us our fractional charge - the "charged particles" in the plasma, corresponding to electrons, have a "charge" of $-m$, so this impurity - or quasi-hole - has a fraction $-1/m$ of the electron charge.

Our (fake) "plasma with impurities" potential in equation E.8 is missing a few terms though. In an actual plasma, we would need to consider the Coulomb interaction between the (M) charged impurities, as well as the interaction between the impurities and the background charge. So, if we add these in, the "correct" plasma potential would be given by:

$$U(z_i;\eta_k) = U(z_i) - \sum_{k<l} \log\left(\frac{|\eta_k - \eta_l|}{l_B}\right) + \frac{1}{4l_B^2}\sum_{i=k}^{M} |\eta_k|^2 \tag{E.9}$$

Now we make some qualitative arguments about a plasma with impurities. We would expect, as long as the plasma is in the fluid phase, that if we add in charged impurities, the charged particles making up the plasma would move around to screen them. Therefore, as long as the impurities aren't too close together (ie, the separation is large compared to some screening length λ), the free energy should be essentially independent of impurity position. This means (assuming all of our assumptions above hold) that if we make a partition function Z' out of the "correct" plasma potential in equation E.9, $U(z_i;\eta_k)$, it should just be some constant, independent of η_k - let's call it I. But this partition function Z' can be written as our original partition function Z multiplied by an exponential containing the "missing" additional terms we added in:

$$Z' = \int \prod d^2 z_i e^{-\beta U(z_i;\eta_k)} = \exp\left(-\frac{1}{m}\sum_{k<l}\log|\eta_k - \eta_l|^2 + \frac{1}{2ml_B^2}\sum_k |\eta_k|^2\right) Z = I \tag{E.10}$$

With this sneaky trick, we now have our expression for Z, which is dependent on η only in the first terms:

$$Z = \exp\left(\frac{1}{m}\sum_{k<l}\log|\eta_k - \eta_l|^2 - \frac{1}{2ml_B^2}\sum_k |\eta_k|^2\right) I \tag{E.11}$$

Taking the necessary derivatives, we can now get our Berry connection, using the expression in equation E.6. The holomorphic and anti-holomorphic Berry connections are:

$$\mathbf{A}_{\eta_k} = -\frac{i}{2m}\sum_{l\neq k}\frac{1}{\eta_k - \eta_l} + \frac{i\overline{\eta}_k}{4ml_B^2} \tag{E.12}$$

and

$$\mathbf{A}_{\overline{\eta}_k} = +\frac{i}{2m}\sum_{l\neq k}\frac{1}{\overline{\eta}_k - \overline{\eta}_l} - \frac{i\eta_k}{4ml_B^2} \tag{E.13}$$

respectively.

To get our Berry phase, we will take a contour integral, moving our quasi-hole $\eta_k \equiv \eta$ around some closed path C. If the path doesn't enclose any other quasi-holes, only the second term will contribute to the contour integral and result in a phase shift γ, given by:

$$e^{i\gamma} = \exp\left(-i\oint_C \mathbf{A}_\eta d\eta + \mathbf{A}_{\overline{\eta}} d\overline{\eta}\right) \tag{E.14}$$

The resulting phase is

$$\gamma = \frac{e\Phi}{m\hbar} \tag{E.15}$$

with Φ the enclosed magnetic flux. This is just the Aharonov-Bohm phase for a particle with charge $e^* = e/m$ - exactly what we expect for a fractionally charged quasi-hole.

If the path C encloses another quasi-hole, we will also get a contribution from the first terms in equations E.12 and E.13. Using the Cauchy integral theorem, we pick up an additional phase

$$\gamma = \frac{2\pi}{m} \tag{E.16}$$

in addition to the Aharonov-Bohm phase. Comparing this to equation E.1, and realizing that one loop is equivalent to two interchanges, we see that the statistical angle of our quasi-hole is $\theta = \pi/m$. This gives us our fractional statistics. For example, quasi-hole excitations of the Laughlin state at filling $\nu = 1/m$ with $m = 3$ have a statistical angle of $\theta = \pi/3$. This is different from either fermions or bosons - the quasi-holes are anyons!

E.4 Anyons: Experiment

Starting from the Laughlin wavefunction, we found that the quasi-hole excitations have fractional charge and fractional statistics. The question then arises of how to measure these anyons experimentally - what signatures should we search for? In some sense, the fact that the Hall conductivity of FQH states quantizes to $\sigma_{xy} = e^2/mh$ for $\nu = 1/m$ is all we need. Based on the Laughlin charge pumping argument mentioned in section C.1, σ_{xy} should always quantize to an integer multiple of e^2/h, assuming the ground state on a torus is not degenerate. So the fact that we see FQH plateaus

in transport implies topological order, anyonic excitations, and their fractional charge and statistics. However, it would be nice to have a more direct method to probe anyons and their braiding statistics experimentally. Not only would this confirm our theoretical picture of the FQH states, but being able to braid and manipulate anyons is a crucial step towards using them for quantum computation (see section E.5).

One method to measure the fractional charge of the quasiparticles directly is quantum shot noise [172, 173]. The idea is that sending a current through a quantum point contact on a 2DEG in the FQH regime can generate an edge current made up of anyonic quasiparticles, if the QPC is in the weak backscattering regime. Making a very sensitive measurement of the magnitude of noise fluctuations as a function of the current can be used to measure the charge of the individual particles. In short, the shot noise amplitude for a particle with charge $e/3$, as is expected for quasiparticles at $\nu = 1/3$, will be significantly lower than if the particles had charge e. The measurement was carried out in a 2DEG sample with a tunable QPC in the late 1990s, and showed just this behavior (Figure E.3). An analytical model for the current noise expected for a given current, temperature, transmission, and particle charge was worked out theoretically, and was found to fit quite nicely to the experimental results. While this result was able to show the fractional charge of the anyonic quasiparticles of the FQH states, it doesn't say anything about their statistics. These types of measurements proved to be more difficult, and were only accomplished quite recently.

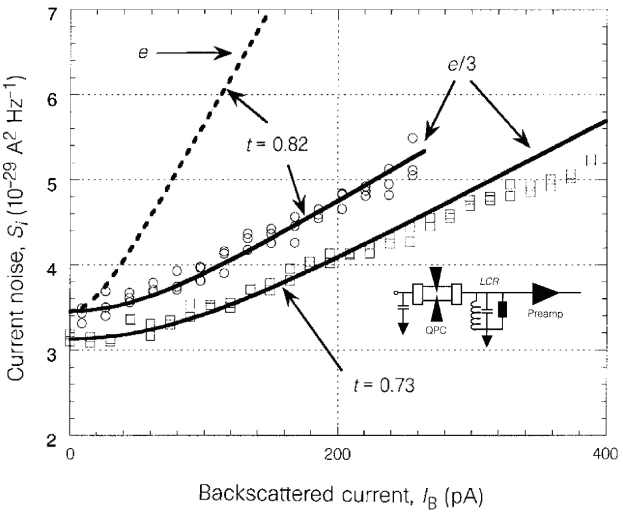

Figure E.3: Shot noise measurement of quasiparticle charge. Measured current noise S_i vs backscattered current, controlled by the applied voltage. Data are taken in the $\nu = 1/3$ regime. Transmission, t, is controlled by the QPC. Solid and dashed lines are theoretical model estimations for the shot noise for particles with charges e and $e/3$, respectively. Inset: Schematic of measurement circuit. Figure adapted from Ref. [172]. Reproduced with permission from Springer Nature.

Two experimental works measuring fractional statistics using different approaches came out in 2020. One of these [140] built on the idea of using noise measurements as a probe of anyons in a

2DEG in the FQH regime, but in this case, with three sets of gate-defined quantum point contacts (Figure E.4a). Two of these QPCs were used to generate anyons, and the third served as a collider for the two incoming anyon currents. To get an idea of why this might tell us something about the fractional statistics, it's useful to think about the limiting cases of fermions and bosons. For fermions, Pauli exclusion forbids both particles from coming out of the same channel. If we define the output cross-correlation between I_3 and I_4 as $S_{I_3I_4}$, this restriction suppresses any correlation, so $S_{I_3I_4} = 0$. Bosons, in contrast, will want to bunch together and leave through the same channel, so $S_{I_3I_4} \neq 0$. Anyons will be somewhere in the middle. The expected relationship between $S_{I_3I_4}$ and the total input current $I_+ = I_1 + I_2$, which also depends on the transmission of the collider QPC, T, can be worked out for anyons. Because this relationship depends on the statistical angle, measuring $S_{I_3I_4}$ vs I_+ gives an experimental approach for observing fractional statistics.

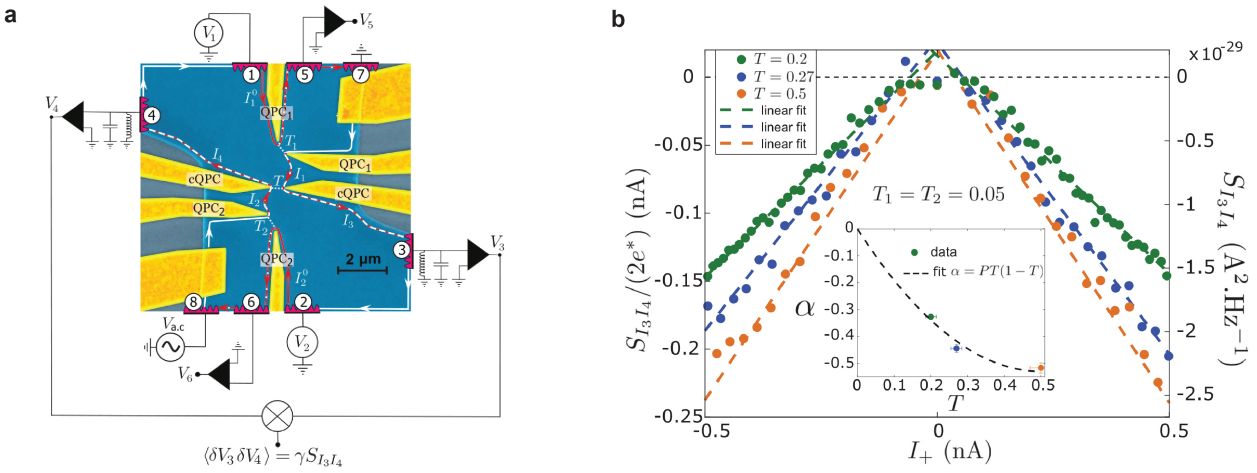

Figure E.4: Anyon collider. a, Anyon collider device image. 2DEG is blue, gates are gold, and edge currents are red. QPC1 and QPC2 create anyon currents I_1 and I_2, which collide at cQPC with transmission T. Correlations between the output currents from cQPC, I_3 and I_4, can be measured as $S_{I_3I_4}$. **b,** $S_{I_3I_4}$ vs total input current $I_+ = I_1 + I_2$ for various T. Slope of the linear fits varies with T. Inset is a fit to the slope variation vs T, with the resulting value of $P = -2.1 \pm 0.1$. The value of P expected for anyons with $\theta = \pi/3$ is -2. Figure adapted from Ref. [140]. Reprinted with permission from AAAS.

In Figure E.4b, we see the results of this measurement. The 2DEG is tuned into the $\nu = 1/3$ FQH state, and QPC1 and QPC2 are tuned to the weak backscattering regime to produce anyon currents I_1 and I_2. Cross correlation $S_{I_3I_4}$ is then determined by measurement of the voltage fluctuations V_3 and V_4. $S_{I_3I_4}$ vs I_+ has a linear dependence, as expected, and is clearly not zero,

as would be expected for fermions. The change of the slope value as T is varied lines up with what would be expected theoretically for particles with a statistical angle $\theta = \pi/3$, as expected.

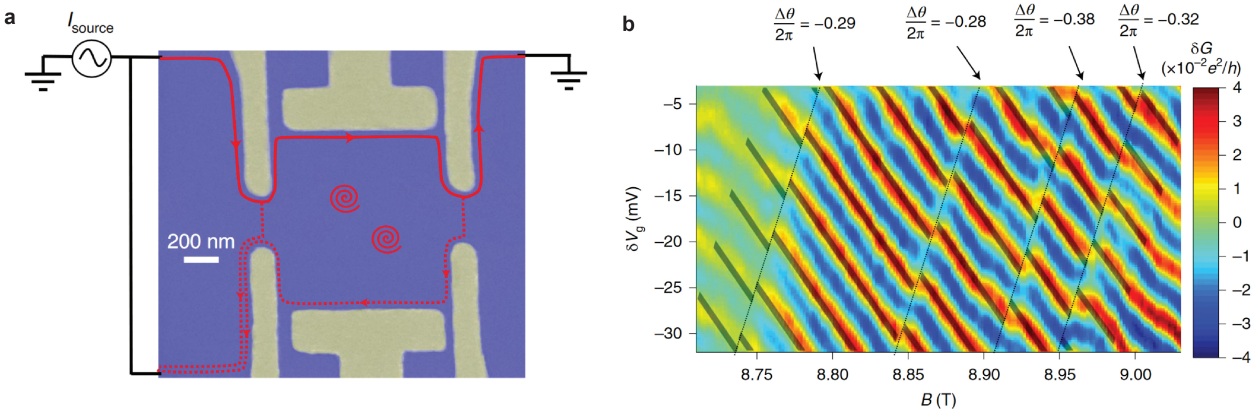

Figure E.5: Anyon interferometer. a, Anyon interferometer device image. 2DEG is blue, gates are gold, and edge currents are red. Spirals signify localized quasiparticles within the interferometer **b,** Conductance oscillations in the $\nu = 1/3$ regime. Interferometer area is tuned by plunger gate voltage δV_g and total flux through the interferometer area is tuned by magnetic field B. Discrete phase jumps, corresponding to a change in the number of quasiparticles in the interferometer region, show values consistgent with a statistical angle of $\theta = \pi/3$. Figure adapted from Ref. [139]. Reproduced with permission from Springer Nature.

The other work [139] relied on quasiparticle braiding, and the link to our discussion of anyon statistics in section E.3 is a bit more straightforward. The idea of this measurement was to build an interferometer on a 2DEG, where the interferometer area is defined by metal gates (Figure E.5a). The device was designed with additional metallic layers to screen the bulk from the edges, allowing for an independent tuning of the interferometer area by the plunger gates and number of localized quasiparticles inside the interferometer by magnetic field. The conductance variation across the interferometer, δG, is shown in Figure E.5b. The oscillations are due to Aharonov-Bohm interference, but there are also multiple "phase slips" in the pattern. These can be attributed to a change in quasiparticle number within the interferometer, which changes the interferometric phase. The behavior of the phase, including the contributions from both the Aharonov-Bohm phase and from anyonic quasiparticles, should go as:

$$\theta = 2\pi \frac{e^*}{e} \frac{A_I B}{\Phi_0} + N_{qp}\theta_{anyon} \tag{E.17}$$

Here, e^* is the quasiparticle charge, A_I is the interferometer area, Φ_0 is the flux quantum, N_{qp}

is the quasiparticle number in the interferometer, and θ_{anyon} is twice the anyon statistical angle. Extracting the phase slip values gives shifts quite close to $2\pi/3$ - just what would be expected for a complete loop around an anyon with statistical angle $\theta = \pi/3$.

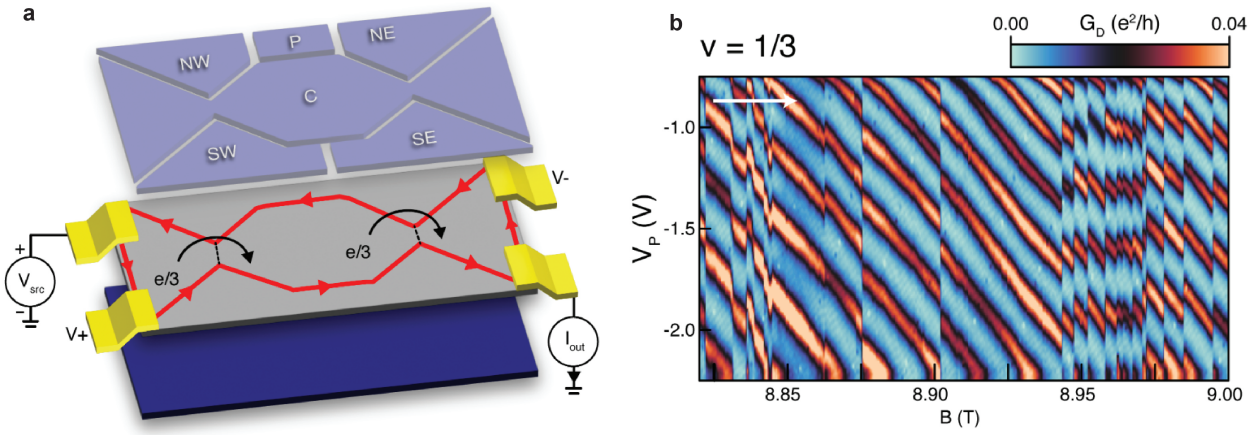

Figure E.6: FQH interferometry in monolayer graphene. a, Fabry-Pérot interferometer constructed from monolayer graphene. **b,** Diagonal conductance G_D vs plunger gate voltage V_P and magnetic field. Values of the sharp phase jumps correspond to those expected for anyons with a statistical angle of $\pi/3$. Figure adapted from Ref. [174]. Reproduced with permission under CC BY 4.0. (a) unchanged, x-axis units added to (b).

A very recent work implemented this type of interferometry measurement in monolayer graphene [174]. AFM cutting allows for a set of gates which electrostatically define the interferometer area and two quantum point contacts in a graphene layer (Figure E.6a). This design enabled measurement of the diagonal conductance $G_D = I_{out}/(V_+ - V_-)$ as a function of the plunger gate voltage, which controls the sample area A_I, and magnetic field, which controls the flux through the sample. When the graphene monolayer is tuned to the $\nu = 1/3$ FQH regime, sharp jumps in phase are observed, with values of shifts corresponding to the anyon statistical angle (Figure E.6b). These results demonstrate the possibility of very high quality interferometry measurements of FQH physics using 2D materials. In addition, this architecture is extremely promising for the study of anyonic statistics in zero-field FCIs.

E.5 Non-Abelian Anyons and Topologically-Protected Quantum Computation

Most of the fractional quantum Hall states, and all of the zero-field FCI states, which have been observed so far are expected to host Abelian anyon quasiparticle excitations. As discussed in the last section, interferometry and noise measurements have directly observed the fractional statistical phase and charge of Abelian anyons in the FQH regime. Performing these types of measurements at zero field on the recently discovered FCIs would certainly be an interesting and ambitious goal. However, the real dream would be to investigate and manipulate non-Abelian anyons - predicted to exist in FQH states at fillings such as $\nu = 5/2$ and $\nu = 12/5$ [141, 142]. No non-Abelian FCI states have yet been observed - this is a very active area of ongoing research, both theoretically and experimentally.

The reason for this interest in non-Abelian anyons is their potential for topologically protected quantum computation. As we discussed in section E.2, particles confined to two dimensions transform under representations of the braid group. This allows, in addition to the $\theta = 0$ and $\theta = \pi$ statistical angle of bosons and fermions, the fractional exchange statistics of the Abelian anyons. However, there are also higher dimensional representations of the braid group. These are associated with non-Abelian anyons. Here, there is a degenerate set of ground states, and braiding non-Abelian anyons applies a unitary operation to this ground state subspace. To perform quantum computations with this system, the quantum information would be encoded in this degenerate ground state subspace, with the unitary operations necessary for performing the computation performed by braiding the non-Abelian anyons. Though this is not the case for all non-Abelian anyons, the unitary operations which can be formed by braiding specific types - such as the Fibonacci anyons - are sufficient for universal quantum computation.

Crucially, essentially the *only* way to perform unitary operations on the encoded quantum information is by braiding the non-Abelian anyons. This is an inherently non-local process - two spatially separated anyons are moved around each other. This is what makes topological quantum computation such a promising method. Local perturbations cannot affect the quantum information and cause errors, and essentially all of the processes by which qubits can decohere are local processes. There are other ways around the issue of qubit decoherence in more conventional architectures, using quantum error correction. However, the error threshold physical qubits must reach before fault

tolerant quantum computation can be achieved is still a ways off.[2] The advantage of topological quantum computation is that the fault tolerance is on the "hardware level". That is, because the quantum information is stored and operated upon non-locally, typical sources of error from interaction with the environment which cause decoherence in normal qubits will not affect the computation.

The price we pay for this inherent fault tolerance, of course, is that we need to find and manipulate non-Abelian anyons in the first place. This is not an easy task. The fact that they can occur at all, however, is quite astonishing. So, despite all the difficulties, the search is on for their signatures in fractionally filled Landau levels. Now, though, with the discovery of zero field FCIs, and the huge degree of flexibility and adaptability of moiré heterostructures, it would not surprise me if the first practical architecture for topologically protected quantum computation turned out to be based on moiré $MoTe_2$.

[2]Interestingly, one of the best algorithms for quantum error correction currently in use - the surface code [175] - evolved out of Kitaev's toric code, created to study topological order. Its performance relies essentially on these same ideas of topological protection.

VITA

Eric Anderson grew up in Washington, D.C. and attended Sidwell Friends School. After living in Beijing for a year following high school, he began his undergraduate at Northwestern University. Over the course of obtaining his Bachelor of Science degree, double majoring in Physics and Materials Science and Engineering, he found himself increasingly gravitating towards condensed matter physics and quantum materials. Following a brief summer at NIST, he started research in the Xu group at the University of Washington. He received a Doctor of Philosophy in Physics following his work on 2D materials and topological phases of matter.